PERFORMANCE EVALUATION OF HIGH-STRENGTH CONCRETE CIRCULAR COLUMNS REINFORCED WITH GFRP BARS AND SPIRALS

By

Mu'taz Muwafaq Mohammad Almomani

A Thesis Submitted to the Faculty of Graduate Studies of
The University of Manitoba

In partial fulfilment of the requirements of the degree of

MASTER OF SCIENCE

Department of Civil Engineering
University of Manitoba
Winnipeg, MB, Canada

May 2021

ABSTRACT

The results of fifteen large-scale high-strength concrete (HSC) columns internally reinforced with GFRP bars and spirals are presented in this thesis. The concrete dimensions and reinforcement of the columns satisfied all the minimum requirements of the relevant Canadian standards. The test parameters in this study include reinforcement type (steel or GFRP), spiral pitch (50 or 85 mm), slenderness ratio (14, 20 or 28), the level of axial load eccentricity (60, 90, 120 or 150 mm) and the loading type (axial or flexural loading). The experimental results were then compared to the predictions of the Canadian and American FRP design codes and guidelines. Compared to the GFRP-reinforced concrete (RC) counterpart, the steel-RC specimen achieved a higher axial capacity (7.8%) with very similar behaviour up to the peak load but a more ductile post-peak behaviour. Both spiral pitches were able to provide adequate confinement up to the peak load, however, the smaller pitch was able to provide a more deformable post-peak behaviour. As the slenderness ratio increased, the lateral displacement increased and the lateral and axial stiffness decreased. The effect of increasing axial load eccentricity was more pronounced than the increase in slenderness ratio and resulted in reduced axial and lateral stiffness. The GFRP reinforcement was able to contribute to the carrying load capacity of both the axially-loaded columns and those under flexure. No failure of any bars or spirals was observed with the exception of the shortest column under the least eccentricity. Under flexural loading, the spirals were able to provide adequate confinement at different loading stages until failure. When compared with the experimental results, the examined codes and guidelines were found to be conservative in predicting the capacities of the columns for all loading conditions and slenderness ratios.

AKNOWLEDGEMENTS

First and foremost, I thank Almighty God (Allah) for providing me with the strength and the will that allowed me to complete my degree. Secondly, I would like to thank my supervisor, Dr. Ehab El-Salakawy, PEng, FCSCE, Professor of Structural Engineering and former Canada Research Chair in Durability and Modernization of Civil Infrastructures (2006-2016) in the Department of Civil Engineering at the University of Manitoba, whose support and guidance has allowed me to achieve the goals I had set early on in my degree and providing me the opportunity to meet and work with an amazing research team.

I would also like to thank all my friends and colleagues for their assistance and support during my studies. I would also like to show my appreciation to the technical staff of the McQuade Heavy Structures Laboratory for their assistance throughout my lab work.

Last but not least, I owe many thanks and a great deal of gratitude to my entire family for their love and encouragement. I would like to personally thank my father, Dr. Muwafaq Almomani, my mother, Wijdan Alhourani, my brother, Mo'ath Almomani and my uncles Ibrahim and Dr. Zeid Alhourani. Without you, none of this would have been possible.

To my beloved mother,

father and brother.

TABLE OF CONTENTS

LIST OF FIGURES

LIST OF TABLES

LIST OF NOTATIONS

The following symbols are used in this study:

A_g = gross area of the column cross-section

D = diameter of the column cross-section

$d_{N.A}$ = depth of neutral axis

d_{s_n} = depth of centroid of concrete strip "*n*"

e = load eccentricity

f_c = stress in the concrete

f'_c = maximum concrete stress obtained from testing standard concrete cylinders

f_{s_n} = stress in concrete strip "*n*"

F_{s_n} = force in concrete strip "*n*"

F_{frp_n} = force in FRP layer "*n*"

k = effective length factor (controlled by column boundary conditions)

K_n = normalised axial load

ℓ = unbraced length of the column

M_n = nominal moment

M_u = experimental ultimate moment

P_n = nominal axial load

P_u = experimental ultimate axial load

$r =$ radius of gyration

$R_n =$ normalised bending moment

$\lambda =$ slenderness ratio, defined as $\frac{k\ell}{r}$

$\varepsilon_c =$ strain in concrete

$\varepsilon_0 =$ strain in concrete corresponding to f'_c

$\delta =$ lateral deflection of the column

ρ_f = GFRP longitudinal reinforcement ratio

ρ_{fs} = GFRP transverse reinforcement ratio

LIST OF ABBREVIATIONS

General Abbreviations

ACI	American Concrete Institute
CSA	Canadian Standards Association
GFRP	Glass Fibre Reinforced Polymers
HSC	High-Strength Concrete
ISIS	Intelligent Sensing for Innovative Structures
NSC	Normal-Strength Concrete
RC	Reinforced Concrete

Specimen Names

G50-20-E60	GFRP reinforced specimen with a spiral pitch of 50 mm and a slenderness ratio of 20 tested under an eccentricity of 60 mm
G85-14-E60	GFRP reinforced specimen with a spiral pitch of 85 mm and a slenderness ratio of 14 tested under an eccentricity of 60 mm (named S14-60 in chapter 4)
G85-14-E90	GFRP reinforced specimen with a spiral pitch of 85 mm and a slenderness ratio of 14 tested under an eccentricity of 90 mm (named S14-90 in chapter 4)
G85-14-E120	GFRP reinforced specimen with a spiral pitch of 85 mm and a slenderness ratio of 14 tested under an eccentricity of 120 mm (named S14-120 in chapter 4)
G85-20-E60	GFRP reinforced specimen with a spiral pitch of 85 mm and a slenderness ratio of 20 tested under an eccentricity of 60 mm
G85-20-E90	GFRP reinforced specimen with a spiral pitch of 85 mm and a slenderness ratio of 20 tested under an eccentricity of 90 mm

G85-20-E120	GFRP reinforced specimen with a spiral pitch of 85 mm and a slenderness ratio of 20 tested under an eccentricity of 120 mm
G85-20-E150	GFRP reinforced specimen with a spiral pitch of 85 mm and a slenderness ratio of 20 tested under an eccentricity of 150 mm
G85-20-FL	GFRP reinforced specimen with a spiral pitch of 85 mm and a slenderness ratio of 20 tested under pure flexure
G85-28-E60	GFRP reinforced specimen with a spiral pitch of 85 mm and a slenderness ratio of 28 tested under an eccentricity of 60 mm (named S28-60 in chapter 4)
G85-28-E90	GFRP reinforced specimen with a spiral pitch of 85 mm and a slenderness ratio of 28 tested under an eccentricity of 90 mm (named S28-90 in chapter 4)
G85-28-E120	GFRP reinforced specimen with a spiral pitch of 85 mm and a slenderness ratio of 28 tested under an eccentricity of 120 mm (named S28-120 in chapter 4)
G85-28-E150	GFRP reinforced specimen with a spiral pitch of 85 mm and a slenderness ratio of 28 tested under an eccentricity of 150 mm (named S28-150 in chapter 4)
G85-28-FL	GFRP reinforced specimen with a spiral pitch of 85 mm and a slenderness ratio of 28 tested under pure flexure (named S28-FL in chapter 4)
S85-20-E60	Steel reinforced specimen with a spiral pitch of 85 mm and a slenderness ratio of 20 tested under an eccentricity of 60 mm

1. INTRODUCTION

1.1 General

Reinforced concrete (RC) has been a major component of the accelerated development of our modern world. Commonly, steel is the main reinforcement used with concrete due to the excellent combination of the tensile strength of steel and the compressive strength of concrete. The greatest drawback of using steel is its susceptibility to corrosion. Concrete is alkaline by nature and the embedded reinforcement becomes enclosed in a passive alkaline film that protects it from corrosion. Designers, adhering to code provisions, also provide an appropriate concrete cover to keep the steel away from the external, more acidic environment to prevent corrosion, however with many factors at play; corrosion is inevitable and can only be delayed (ACI Committee 222 2019).

Some structures are vulnerable to harsher environments than others are. Bridges, for example, are constantly subject to the use of de-icing salts during winter. In addition, many structures built over waterways are subject to high humidity and salt exposure due to the nature of the marine environment. Since corrosion is a key issue affecting the durability of RC structures, leading to the need of costly repairs, many researchers have proposed remedies for this situation. Increasing concrete cover, using additives to make the concrete less permeable, coating of steel with epoxy, using galvanized or stainless steel are all methods to mitigate corrosion. Although these methods have been successful in prolonging the time the structure can stand without the need of repairs, they have not been able to eradicate the problem since it stems from the nature of the steel itself (ACI Committee 222 2019).

The only way to remove corrosion from the equation was to look for alternatives to steel reinforcement. Over many years, Fibre Reinforced Polymer (FRP) reinforcement has become the

predominant solution to that problem. Unlike steel, FRP is a non-corrosive material by virtue of its non-reactive constituents (ACI Committee 440 2015). It is also more advantageous than steel on more fronts, such as its high tensile strength in comparison to the conventional reinforcing steel as well as being much lighter, giving it a very high strength to weight ratio. In addition to those mechanical properties, FRP is also electromagnetically transparent and has very low conductivity of heat and electricity making especially useful for applications where that transparency is a major consideration for design (ISIS Canada 2007).

Design equations and code provisions for steel-RC structures have been constructed based on the properties and behaviour of steel. Thus, when making a radical change such as replacing steel, we must consider the fact that existing equations cannot be directly transferred to FRP-RC design. The main difference between steel and FRP is that the latter does not yield. The FRP material experiences elastic deformation up to failure and shows no signs of a stress-strain plateau like that of steel. Few types of fibres such as carbon, aramid, glass and recently, basalt have been used to produce FRP reinforcement. However, glass FRP (GFRP) is the most desirable due to its great strain capacity and its relatively cheaper cost. As shown in Figure 1.1, GFRPs generally have a much higher tensile capacity and lower modulus of elasticity than steel.

Understanding the properties of FRP through previous research has led to the development of design provisions such as the Canadian standard CSA/S806 (CSA 2002, 2012 & 2017) and the American guidelines ACI 440.1R (ACI 440 Committee 2001, 2003, 2006 & 2015) and the integration of FRP-RC design in the Canadian Highway Bridge Design code, CHBDC, CSA/S6 (CSA 2000, 2006, 2014 & 2019). Moreover, most of these design provisions, namely the CSA/S806-12 (2017) and ACI 440.1R-15 (2015) do not allow for or recommend the consideration of the compressive contribution of FRPs in design. However, very recently, the CSA/ S6-19 (2019)

has permitted the use of FRP materials in compression zones and have allowed for their compressive contribution to be used in design up to a strain of 0.002.

Reinforcement of some structural elements are more susceptible to corrosion due to their greater proximity to corrosive environments. Columns used in aggressive climate, such as bridges and structures in marine environments, are more prone to having increased susceptibility (ISIS Canada 2007; ACI Committee 222 2019). Exposed compressive elements are often designed with a circular cross-section due to their aesthetic appearance (Hadhood 2017). In addition to aesthetics, circular columns have a larger inertia making them less likely to buckle under load and have more uniform confinement stresses when compared to their rectangular counterparts. Therefore, circular columns are more preferable in external applications and so are more likely to be exposed to harsh conditions.

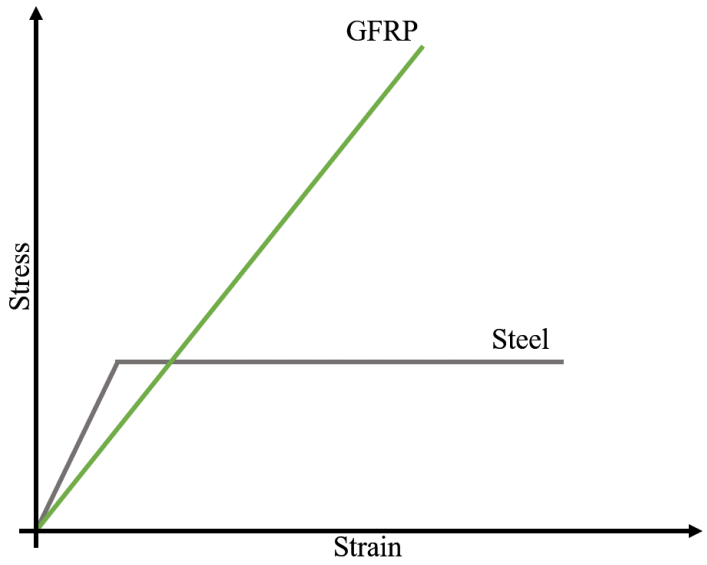

Figure 1.1 - Typical stress-strain relationship for steel vs GFRP reinforcement

The continuous development of concrete from the early 1900s and onwards meant that existing definitions had to be updated. Concretes with compressive strengths of 34 MPa were considered high-strength concrete (HSC) in the 1950s, but by recent standards, are normal strength concrete (NSC). This shows the advancements of current research and technology and the need for the redefinition of terms such as HSC. Current standards classify compressive strengths of 55 MPa or greater to be HSC. Such materials behave in a more brittle manner and special considerations must be taken in their design (ACI Committee 363 2010). Moreover, while HSC is widely used, its behaviour is still not as well defined as NSC, and even less with FRP reinforcement.

In column design, the amount of confinement reinforcement is equally important as the aforementioned material properties. Current design provisions dictate a maximum spiral reinforcement pitch, to ensure adequate confinement of the concrete core of the columns. There are two provisions in the Canadian standards CSA/S806-12 (CSA 2017) on spiral pitch; one for columns predominantly under axial load and another to ensure adequacy under seismic loading. While the provisions ensure the effectiveness of the column confinement (Ali 2015), their adequacy for HSC is yet to be determined.

For columns to be designed in accordance with these provisions, it becomes essential to consider the predominant external loading conditions. Eccentric loading is present in structures due design requirements or imperfections in executions. Nevertheless, the high probability of their occurrence increases the need for their consideration in design. The behaviour of eccentric loading in columns is characterised by an axial load-bending moment interaction diagram, which has been known and extensively covered by research on steel-RC columns. The standard shape of the interaction diagram is dependent on the yielding behaviour of steel reinforcement. However, since FRP does not experience yielding in comparison with steel, the interaction diagram may consequently be

different. The interaction diagram is composed of multiple points, each representing the column under a different combination of axial load and bending moment. To characterise the behaviour of FRP-RC columns, they must be studied under varying loads and moments. These can be controlled by varying the eccentricity of which a load (P) is applied and hence creating a moment ($M = P.e$).

In addition to the moment caused by eccentric loading, buckling of the column can produce secondary moment. The effect of buckling is directly proportional to the column's slenderness ratio $\lambda = k\ell/r$, where k is the effective length coefficient, ℓ is the unbraced length of the column, and r is the radius of gyration. As a result, slender columns are more prone to buckling and secondary moments than short columns. Furthermore, the Canadian standard CSA/S806-12 (CSA 2017) does not permit the use of FRP reinforcement in slender columns. This emphasises the effect of buckling on the capacity of the columns as well as the importance of studying the slenderness ratio on the behaviour columns. Additionally, columns reinforced with the minimum reinforcement ratio set by the codes are very common in structures. Such reinforcement ratio further increases the risk of instability in columns (Broms and Viest 1961). Therefore, large-scale slender and short columns that satisfy the minimum reinforcement provisions of design codes were investigated in this study.

1.2 Problem Definition

For many years, steel reinforcement has been used in concrete structural members to provide additional strength to the concrete, especially in tension. During the lifetime of the structure, it can endure harsh and corrosive environmental conditions that can cause substantial damage to these structures. This occurs because steel is highly susceptible to corrosion. Even though different methods have been used to stop the corrosion, it only seems to delay the need for inevitable and

expensive repair and maintenance measures; in some cases, the need to replace entire structural elements in the structures such as bridge decks. This replacement and repair can be very costly and extremely difficult in elements such as columns. The use of FRP in structural elements has been recognised as an effective alternative, which eliminates some of the problems that exist in steel-RC elements (El-Salakawy et al. 2003; ACI Committee 222 2019). The decreased need for regular repair and replacement of GFRP-RC elements, in comparison to steel-RC, making it a more economical option.

When designing compressive members, load eccentricity can greatly reduce the axial capacity of the member; therefore, it must be considered and incorporated into their design. When the column is loaded eccentrically, compressive and tensile stresses begin to form. To simplify the design process, equivalent models to the actual compression distribution in concrete were introduced. A non-uniform compression stress is converted into a uniform stress block. This stress block has a width of $\alpha_1 f'_c$ and length of $\beta_1 c$; where c is the depth of the neutral axis. The values of α_1 and β_1 where developed considering steel-RC members, cast with normal strength concrete. However, by assessment of 184 columns from literature, Hadhood (2017) found that the ACI equivalent rectangular stress block (ERSB) is un-conservative for HSC circular columns. Moreover, recent guidelines remain less conservative than critical limits.

In addition to eccentricity, the slenderness effect can also cause instability in the column and have an effect on the capacity of the column. Consequently, codes are reluctant to allow the use of FRPs in such members. However, slender columns are common in buildings, which makes the study of such GFRP-RC members and assessing their safety of importance. Recent studies have also recommended the reduction of the slenderness ratio limit for FRPs due to different properties,

including their low modulus of elasticity. Therefore, it becomes necessary to study such recommended limits as this may lead to columns having lower capacities than designed.

As structures become larger, higher performance materials, such as HSC, are sought to fulfil the demand. However, when higher strength concrete is used, the concrete becomes less deformable. Consequently, this change causes the models used previously in design to become un-conservative. In addition to the different concrete properties, the change of reinforcement from steel to GFRP makes the study of such elements more critical.

1.3 Scope of Work

The use of GFRP reinforcement has increased in recent years and research is required to ensure the safety of critical infrastructure utilizing such reinforcement. The aim of this study was to investigate the behaviour of HSC columns due to the common use of such material and the brittle nature of the material compared to NSC, since HSC may interact differently with GFRP reinforcement and compromise the conservativeness of design codes. Additionally, the slenderness ratio limit and slenderness effect were examined to verify the validity of the current design code provisions in this regard. Furthermore, the tested columns were reinforced with the minimum reinforcement allowed by the relevant design codes as this introduces risk of instability in the structural elements. The studied parameters included slenderness ratio, reinforcement type, transverse reinforcement ratio, eccentricity level and loading type.

1.4 Objectives

The objectives of this study were to:

- Compare GFRP-reinforced HSC columns to their steel-reinforced counterparts and identify any behavioural differences.

- Investigate the effect of spiral pitch on the behaviour and capacity of HSC columns reinforced with GFRP.
- Investigate the axial-flexural capacity and failure mechanism under the effect of different eccentricity-to-diameter ratio.
- Investigate the effect of the slenderness ratio on GFRP-reinforced HSC columns by testing short and slender columns of slenderness ratios of 14 and 28.
- Investigate the slenderness ratio limit of current design provisions and whether it is necessary to reduce it from the current value of 22 as per the CSA A23.3-19 (CSA 2019) and the ACI 318-19 (ACI 2019).

1.5 Work Methodology

Fourteen large-scale GFRP-reinforced HSC circular columns were constructed and tested in this study in addition to a control steel-RC specimen. The specimens had a diameter of 350 mm and lengths of 1,250 mm (λ = 14) 1,750 mm (λ = 20) and 2,450 mm (λ = 28) and were constructed with a target compressive strength of 60 MPa. The ends of the columns were encased with specially fabricated steel collars to prevent premature failure and to facilitate pin-pin boundary conditions. The columns were tested under varying eccentricities of 60, 90, 120, 150 mm, corresponding to *e/D* ratios of 0.17, 0.26, 0.34 and 0.43, respectively. Additionally, a specimen was tested under pure flexural loading. Moreover, the spiral pitch was varied to test its effect on the confinement of the column; pitches of 50 and 85 mm were used.

1.6 Thesis Layout

This thesis consists of six chapters as follows:

Chapter 1 defines the problem and provides a brief introduction to the topic and presents the scope, objectives and the work methodology of the work.

Chapter 2 presents the most recent findings and the state-of-the-art research into GFRP-RC columns. The chapter identifies various parameters and discusses previous findings and knowledge gaps related to the behaviour of columns. Furthermore, the chapter provides summary of relevant design codes and guidelines with regards to the use of GFRP materials in compression members.

Chapter 3 presents the experimental method used to construct and test the GFRP-RC specimens. The chapter highlights the material properties, the test matrix and the variables addressed by each specimen series.

The following chapters (4 and 5) are presented in journal article format. The articles have been submitted to the respective journals and are currently under review.

Chapter 4 (Article 1) presents the experimental method used and the results of eight of the fifteen large-scale HSC specimens consisting of three short and five slender columns. The article studies the differences that characterize slender behaviour by testing slenderness ratios that satisfy both code definitions and literature recommendations of the slenderness limit. The response of the columns is tested under different loading conditions including varying eccentricities and a flexural test. The results are compared against code predictions to identify whether the codes are conservative.

Almomani, M., Mahmoud, K., and El-Salakawy, E. “Effect of Slenderness Ratio on GFRP-Reinforced High Strength Concrete Columns." ACI Structural Journal, Submitted in April 2021.

Chapter 5 (Article 2) presents the experimental results of ten specimens. The article studies variables such as reinforcement type, transverse reinforcement pitch, slenderness ratio, level of eccentricity and loading type. The study identifies the difference in behaviour between the two

slenderness ratios and whether the code definitions need to be modified to account for material differences between steel and GFRP reinforcement.

Almomani, M., Mahmoud, K., and El-Salakawy, E. “Effect of Slenderness Ratio on Large –Scale Eccentrically-Loaded GFRP-Reinforced HSC Columns." ASCE, Journal of Composites for Construction, Submitted in May 2021.

2. LITERATURE REVIEW

2.1 General

Steel has many advantages, like its strength and ductility, but due to its reactivity, steel corrosion has been a very costly issue. This has led researchers to investigate alternatives such as FRP material in order to solve this problem.

The post-World War II era saw a great advancement in the area of composite materials. Polymers were already recognized for their strength and versatility by industries such as aerospace in which they have been widely used. The ease at which such materials could be made and shaped increased its utilization by manufacturers of sports and fishing equipment. It was only in the 1960s that FRP was introduced to the construction industry. Its potential as a replacement to steel reinforcement was recognised. Currently, many structures in Canada are reinforced with FRP, especially following the development of provisions for design with FRP materials. Many bridges were constructed such as the Headingly Bridge and the Floodway Bridge over the Red River in Manitoba, with latter becoming the largest bridge to be constructed using non-metallic reinforcement in the world, consuming over 140,000 kg of GFRP in its construction. GFRP reinforcement was used in many bridges in other parts of Canada, no reports of deterioration even after 20 years in service. In Quebec, stands the Wotton Bridge, the Magog Bridge, Cookshire-Eaton Bridge and the Val-Alain Bridge and they remain structurally intact until this day (ACI Committee 440 2015; El-Salakawy et al. 2003).

2.2 Fibre-Reinforced Polymers

In the search of a solution to the corrodibility of steel, FRPs have been shown to be superior alternatives as internal reinforcement to epoxy coated steel in concrete structures. The use of FRPs has become widely accepted since the recognition of its highly advantageous properties in the 1970s such as its high strength to weight ratio and very low susceptibility to corrosion. FRP is a composite material consisting mainly of fibres and resins which give it its aforementioned qualities.

Many factors can affect the mechanical properties of FRP but are mainly controlled by the manufacturing process. Quality control measures by the ISIS Product certification allow no less than 55% fibre content in FRP bars or rods. Many other limitations have been imposed on the manufacturing of these products, such as the percentage of certain diluents within the base resin and other agents such as coupling, hardener and UV agents with many more, to ensure higher consistency in the production and ensure greater reliability of FRP bars (ISIS Canada 2007).

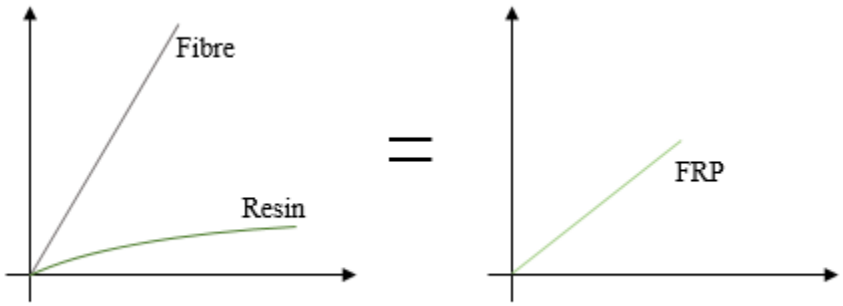

Figure 2.1: Relative comparison between the stress-strain relationship of fibres, resins and FRP

The strength and stiffness of the FRP bars are derived from the fibres whereas the resins provide a bond that laterally supports the bars against buckling and serves as a transfer medium of inter-laminar and in-plane shear.

2.3 Steel-RC Columns

Research on steel reinforced concrete began in the early 1900s. Since then, extensive research has been carried out to test the behaviour of concrete elements under different types of loading. This helped construct the understanding we have today of reinforced concrete, and consequently the provisions that govern the design of such elements.

The behaviour of columns under axial loading is characterised into two stages, one being from 0 load to peak capacity and a post-peak stage. During the initial stage the capacity of the column is dependent only on the material properties; namely, the compressive strength of the concrete and steel used in the column. The relationship up to peak is an increasing relationship until the peak load that according to the (ACI Committee 318 2019) is defined as:

$$P_o = 0.85 f_c' \left(A_g - A_{st}\right) + f_y A_{st} \qquad \text{Equation 2.1}$$

where f_c' is the compressive strength of the concrete cylinder test. A_g and A_{st} are the gross areas of the concrete and steel in the column cross-section respectively. f_y is the yield strength of the reinforcing steel. A factor of 0.85 is used to translate the strength of the cylinder from the test to the actual strength of the concrete within the column, it accounts for differences such as size and shape (Park and Paulay 1975).

The second stage begins when the column reaches the peak capacity. As the concrete cover begins to spall, the transverse reinforcement is activated, and the column starts to carry additional load.

The most common column loading is a combination of axial load and moment. Within a structure, the presence of a small deviation in the alignment of structural elements will cause moment to be generated on those elements. In other cases, eccentricity could be due to an imbalance in loading because of the design. The presence of those moments creates an eccentricity equal to the moment applied divided by the axial load, $e = M_u/P_u$. Regardless of cause of the eccentric loading, the behaviour of columns with moment is very different from that of a purely axially loaded one. Over time, generated data on eccentrically-loaded steel-RC columns helped develop diagrams to help predict capacity of eccentrically loaded columns. The combination of axial load and bending moment capacity can be plotted in an Axial Load-Bending Moment Interaction diagrams. As per the ACI-318-19 (ACI Committee 318 2019) and CSA A23.3-19 (CSA 2019d), basic assumptions must be made when developing an interaction diagram: (1) A perfect bond exists between the concrete and the steel, (2) the strength of concrete is only considered in compression, (3) A plane-section remains plain and so when bending is applied the strains within the section are proportional to their distance from the neutral axis of the section, (4) concrete is considered to be failed when its strain has reached 0.0035 or 0.003 according to CSA A23.3-19 and ACI 318-19, respectively. The stress-strain behaviour is idealised, where the strain keeps increasing after yield without gain in strength or what is known as strain hardening (Fig. 2.2).

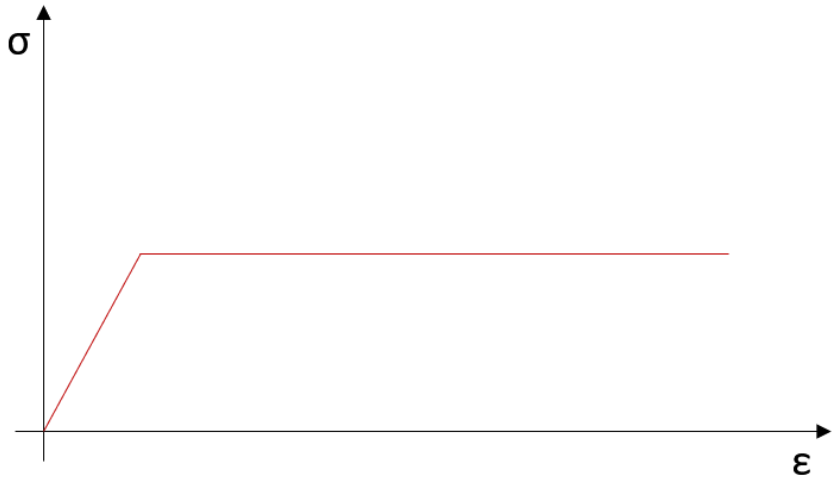

Figure 2.2: Idealised stress-strain relationship of steel reinforcement

Taking into account the material properties and the aforementioned assumptions, an interaction diagram can be developed. There are three main points that shape the interaction diagram; a point representing pure axial loading, pure bending point and a balance point (Fig. 2.3)

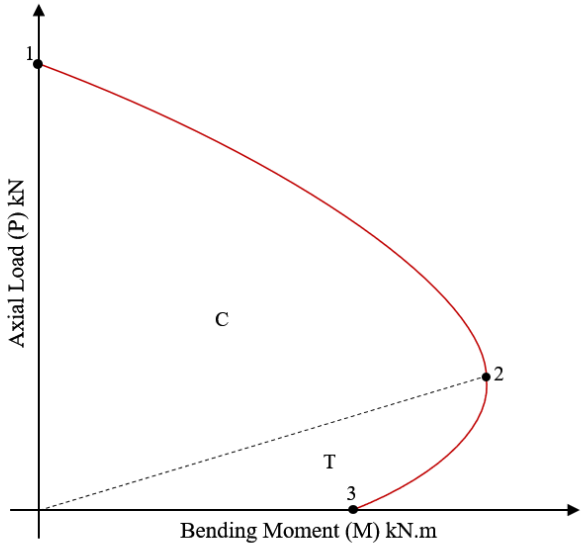

Figure 2.3: Typical axial load-bending moment interaction diagram

Point 1 on the diagram represents the load that the column can theoretically carry with no moment acting on it. Point 3 represents pure bending, where the column should be able to carry that moment with no applied axial loads. The diagram is divided into two parts, before point 2; which represents failure that is compression controlled, and after point 2; which represents failure of the column that is tension-controlled. Point 2, which is the balance point, is a theoretical phenomenon in which the steel yields at the same time the concrete crushes and it helps identify, to a certain degree of accuracy, the type of failure of a designed column. If the failure is tension controlled the steel will yield before the concrete crushes, whereas in the compression-controlled case the concrete crushes before the tension steel yields; the reinforcement in the compression may also buckle.

When a column fails, ductility helps provide early warning for the occupants of the building to evacuate; this favoured ductile behaviour is obtained through tension-controlled design. If a column is compression controlled, the failure will be brittle and sudden. (Park and Paulay 1975).

2.4 GFRP-RC Columns

The pressing need for a solution to corrosion has progressively led to research and wide acceptance of GFRP as concrete reinforcement (Ali and El-Salakawy 2016; Mahmoud et al. 2016; El-Gendy et al. 2016; Barua and El-Salakawy 2020; Barua et al. 2021; Abdallah and El-Salakawy 2021). The main behavioural differences between GFRP and steel reinforcement arise from the core properties of the materials. The main difference being that FRP reinforcement lacks the yielding phenomenon that steel exhibits. This requires design codes to provide new considerations for the design of elements reinforced with GFRP. However, due to the well-established provisions for steel, many of the current provisions of FRP are modelled from those of steel taking into account the FRP properties.

The axial capacity of a column comprises of the compressive capacity of the concrete and the reinforcement, as shown in Equation 2.1. However, for FRP-RC columns, the capacity of the reinforcement is neglected by omitting the corresponding term. Both the CSA/S806-12 (2017) and the ACI 440.1R-15 (2015) neglect or do not recommend the consideration of the compressive capacity of FRP bars. However, the CSA/ S9-19 (2019) has allowed for FRP use in compression up to a strain of 0.002.

Moreover, when subject to lateral loading, the differences in behaviour between steel and FRP-RC columns become more pronounced. Under seismic loading conditions, the steel reinforcement helps dissipate energy and provides ductile behaviour due to its yielding plateau. In contrast, FRP behaves linearly and is not as effective in energy dissipation. However, as shown by (Tavassoli 2013; Ali and El-Salakawy 2016; Abdallah and El-Salakawy 2021), when the GFRP-RC columns were well confined, the deformability of the column was able to replace the ductility provided by steel. Additionally, strength degradation of the column was found to be insignificant before failure as the GFRP was able to effectively confine the concrete core.

As columns are laterally loaded, columns develop both tension and compression zones. After the concrete cover spalls, the confinement is activated, and another peak load is observed after the initial peak. In steel RC columns, as the load approaches the second peak, the steel begins to yield, and the column begins to lose its capacity. However, due to the non-yielding nature of FRP and its superior tensile strength, they are able to provide better confinement and post-peak behaviour in the column after spalling of the outer concrete cover (Fig 2.4).

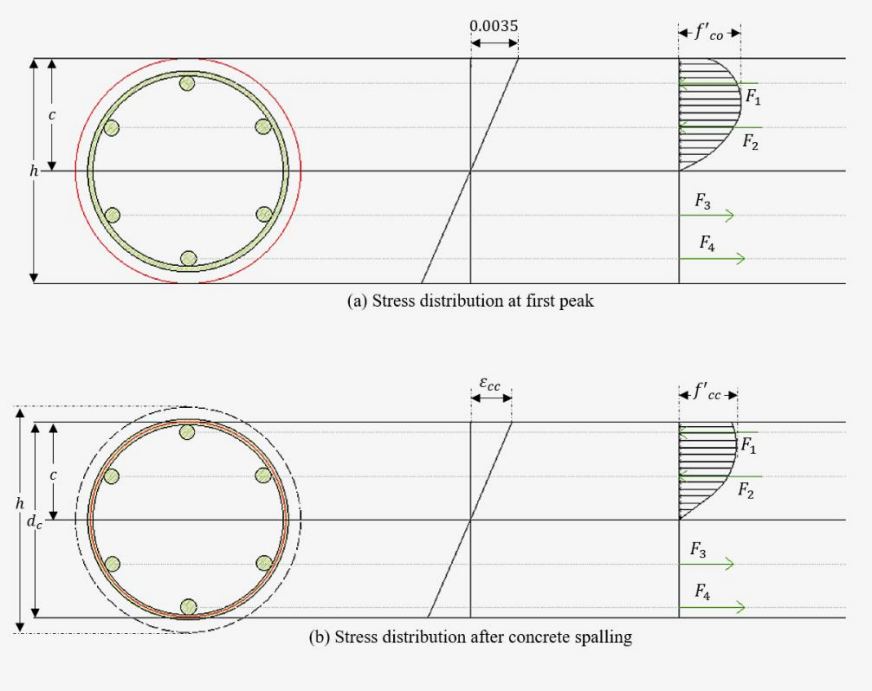

Figure 2.4: Stress distribution in the column peak and post-peak stages (adapted from Karim et al. 2016)

Many recent studies have investigated the behaviour of GFRP columns under eccentric loading. Studies such as Hales et al. (2016); Khorramian et al. (2017); Hadhood (2017); Abdelazim (2020); Barua and El-Salakawy(2020) and Barua et al. (2021) have provided evidence of the viability of GFRP reinforcement in such loading conditions and their ability to sustain large strains and effectively carry tension and compression. Moreover, GFRP lateral reinforcement was shown to develop sufficient strains and provide adequate confinement to the columns.

2.5 High Strength Concrete

Since the adoption of steel-reinforced concrete, the basic components of this composite underwent extensive research and development. Enhancements included increase in strength, which lead to continuous re-evaluation of existing definitions in available codes and guidelines. In the 1950,

concrete with compressive strength of 34 MPa was considered ‘high-strength’ concrete. In the 1960s, HSC was changed to 52 MPa as it became commercially available, followed by 62 MPa in the 1970s. Currently, many cast-in-place buildings are constructed with compressive strengths of up to 138 MPa. However, within controlled settings researchers were able to produce concrete strengths greater than 800 MPa (Schmidt and Fehling 2004).

High-Strength concrete demand began in the U.S.A. during the 70s; namely for the Water Tower Place in Chicago, IL. The structure required 62 MPa concrete and was 260 m in height. In the late 80s concrete strengths being used in buildings reached 83 and 131 MPa; for the 311 South Wacker building in Chicago and Two union square in Seattle, WA, respectively. The latter had set a record for the highest concrete compressive strength used in a building.

The current definition of HSC is any concrete with a specified compressive strength of 55 MPa or higher. This definition indicates the strength at which the production and testing require special levels of care and design requirements. It is also expected that as the development of concrete strength continues with the availability of advanced technology, continued research and a higher demand for more superior materials, many revisions of current definitions will be made and new definitions of HSC will be set in place.

The defining value of 55 MPa represents the lower limit of high-strength compressive strengths. However, this is not to suggest that such compressive strength requires radical changes in either the production methods or properties of the materials. In fact, the production of different concrete strengths is a continuous process, starting with the lower strengths and working up to higher compressive strengths. When designing structures, concrete strength is an important factor. Based on research data, empirical equations were developed to model the behaviour of concrete.

Although some equations have been developed for higher compressive strengths, the availability of data on HSC, or lack thereof, necessitates reassessing current equations to determine their applicability with such types of concrete. Consequently, more tests must be done to develop models with higher accuracy and better compatibly for higher-strength concretes, as opposed to extrapolating from current provisions (ACI Committee 363 2010).

A study addressing concrete strength (Xue et al. 2018), evaluated the behaviour of columns cast with concrete strengths of 29.1 MPa, 40 MPa and 55.2 MPa. It was observed that there was an expected increase in capacity of the column. Moreover, a decrease in ultimate displacement was observed as the compressive strength of concrete was increased. These behaviours can be directly linked to the properties of the concrete, since HSC is known to have more brittle behaviour. Additionally, (Hadhood et al. 2016) studied the behaviour of HSC columns reinforced with GFRP. Although many studies conducted on regular strength concrete suggest high conservativeness of code provisions for normal strength concrete (NSC) columns, this study suggested inadequacy of those design provisions for HSC columns.

Both works of Xue et al. (2018) and Hadhood et al. (2016) make it clear that there are differences in the behaviour of concrete with higher strengths that need to be addressed. Previous research has provided a basis on which current provisions have been established. Nonetheless, much research is required to develop an understanding of GFRP-RC columns. This would help incorporate FRP into more areas of structural design. As is evident, the compressive strength of concrete is a major factor that needs to be accounted for in future works. Recently, Abdelazim et al. (2020) and Hadhood et al. (2016) studied the behaviour of GFRP-HSC columns. The reinforcement was shown to contribute to the capacity of the columns and were able to improve columns stiffness as

tensile cracks appeared. Moreover, HSC columns showed higher capacities than their NSC counterparts. However, the NSC showed higher deformability.

2.6 Confinement

Lateral reinforcement in columns, particularly in the form of continuous spirals, has two beneficial effects on column behaviour. It confines the concrete core against expansion, hence, increasing the column's capacity. It also increases the axial strain capacity of concrete, permitting a more gradual and ductile failure, creating a tougher column (Ahmad et al. 1982; Martinez et al. 1984; Yong et al. 1988).

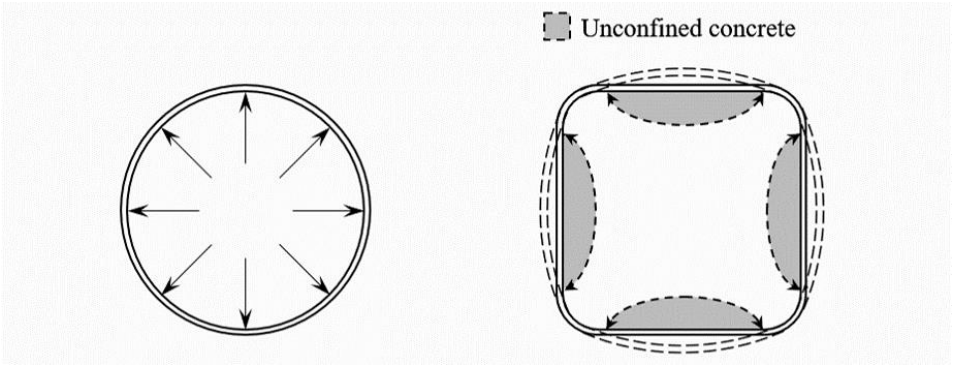

Figure 2.5: Confinement in circular and square/rectangular columns

The basis for design of spiral steel is that the strengthening effect of the spiral should be at least equal to the column strength lost when the concrete shell outside of the spiral spalls off under load (ACI Committee 363 2010). The equation used for the volumetric ratio in the (CSA S806 2017) is given by:

$$\rho_{Fs} = \frac{f'_c}{f_{Fh}}\left(\frac{A_g}{A_c} - 1\right)\left(\frac{P}{P_0}\right) \qquad \text{Equation 2.2}$$

The code provides two sets of provisions for the pitch of transverse reinforcement in compression members. These limits are different based on the load condition to which the column is subjected. For the specific purpose of resisting seismic loads, the CSA S806-12 (CSA 2017) dictates that the pitch must comply to the smallest of the following, 1) One quarter of the least dimension of the member, 2) 150 mm, 3) 6 time the diameter of the smallest longitudinal bars. This is to ensure that the column can provide adequate strength and lateral drift.

In the case of Ali and El-Salakawy (2016), eight concrete columns were fabricated and tested under seismic loads combined with different axial load levels. The columns tested in this study were cast with a 28-day strength of 35 MPa. Three of the tested columns, fully reinforced with GFRP, had a longitudinal reinforcement ratio of 1.3% and a spiral pitch varying between 75, 100 and 150 mm. The efficiency of the code provisions for spiral spacing was investigated. The performance of a column with a spiral pitch complying with code provisions was compared to larger pitches, 100 and 150 mm.

The study found that the code provisions for the spacing of the spirals relating to seismic load resisting columns was more effective at confinement than the larger values. It provided more deformability and hence better performance under seismic lateral loading. Similarly, (Naqvi et al. 2016) also found that a 75-mm spacing had better performance against larger spacing since it provided the required deformability and prevented early crushing of concrete under the applied cyclic loading. Therefore, both concluded that the code provisions for FRP confinement in columns resisting lateral seismic loading was adequate and necessary.

Volumetric ratio can be increased by increasing the spiral size or by decreasing the spiral pitch. This was investigated by (Tavassoli 2013) where nine full scale columns were fabricated and

tested. The columns had a diameter of 356 mm and a length of 1,473 mm and were cast using concrete with 35 MPa compressive strength. The columns were longitudinally reinforced with 6-25M bars. The study varied the transverse reinforcement by changing the diameter of the spirals while keeping the pitch similar. In the second case, the diameter of the spiral reinforcement was kept the same while the pitch was changed.

In the first scenario, the column laterally reinforced with 16-mm diameter spirals performed better than those reinforced with 12-mm diameter spirals. This was shown by the higher ductility parameters of the first over the latter. Moreover, the column with 16-mm diameter spirals showed increased moment capacity. Similarly, the decrease of the pitch of the spirals for the second group from 160 to 50 mm showed increase in moment capacity and showed more hysteresis loops. Thus, proving that the smaller pitch is more effective at dissipating energy. The increase in moment capacity observed when reducing the pitch from 160 to 50 mm was 47% and even when comparing the decrease from 275 to 160 mm the increase in moment capacity was 21%.

Although it was observed that both methods of increasing transverse reinforcement produced increase in the capacity of the columns, the increase of the spiral bar size was shown to be less effective than decreasing the spiral pitch. Nevertheless, these results show that transverse reinforcement is one of the major factors that dictate the behaviour of the columns and should therefore be investigated when other variables are studied to effectively map the behaviour of GFRP-RC columns.

For compression members in general, the code provisions require the pitch to be: 1) One sixth of the core diameter; 2) 25 mm $\leq$ pitch $\leq$ 75 mm. Tests carried out by (Guérin et al. 2018) studied rectangular full-sized columns of 405 mm x 405 mm dimensions, with volumetric ratios of

approximately 0.75%. They concluded that the use of 152 mm pitch showed better confinement of the core than a pitch of 203 mm. The columns were able to maintain confinement for up to 12,000 με. Another full–scale test was carried out by Hadhood et al. (2016) using circular columns of 305-mm diameter and 1,500-mm length. Carbon FRP (CFRP) was used as internal reinforcement and a spiral pitch of 80 mm. The results showed that the spirals were able to confine the core post-peak. The aforementioned studies used concrete compressive strengths of 42, 24, 38, and 35 MPa, respectively.

Moreover, Hadhood et al. (2016) carried out testing on HSC circular columns cast with 70 MPa concrete using No. 3 GFRP spirals at a pitch of 80 mm. The study found that at higher eccentricities, the spirals were able to maintain adequate confinement. However, for lower eccentricities the spirals were found to be insufficient at providing the required elastic behaviour and hence was not able to provide enough warning before failure. The provided reinforcement, which equates to a volumetric ratio of 0.95%, was inadequate on the compression side.

As evidenced in the aforementioned studies, the lateral reinforcement provisions in the Canadian design code (CSA S806 2017) proved to be conservative as larger spiral pitches were able to maintain integrity of the concrete core until later stages of loading. However, the findings of Hadhood et al. (2016) suggest that the provisions are not as adequate for HSC as they are for NSC for eccentrically loaded columns.

2.7 Longitudinal Reinforcement

Longitudinal reinforcement is essential for resisting axial loads and applied moment in columns. In concentrically loaded columns, longitudinal reinforcement can add to the axial capacity of the concrete and hence reduce the overall size of the column. However, when loading a column

laterally the reinforcement's primary role would be to resist tension that may arise from eccentric loading or seismic activity. Additionally, in seismic load cases, the longitudinal reinforcement provides much needed ductility in order to dissipate energy, this helps to delay or prevent sudden brittle collapse.

Guidelines provided by the Canadian code CSA S806-12 (CSA 2017) dictates a minimum reinforcement ratio of 0.01 of the gross area of the column to be used and a ratio of no greater than 0.08. This is to prevent overcrowding of reinforcement at lap splice areas. However, the compressive strength and stiffness of FRP bars must be ignored in design, as per Clause 7.1.6.4. Moreover, according to Clause 8.4.3.3, slender compression members satisfying the following conditions shall not be permitted to be reinforced with FRP longitudinal reinforcement:

$$\frac{kl_u}{r} \geq 34 - 12\left(\frac{M_1}{M_2}\right) \geq 4 \qquad \text{Equation 2.3}$$

$$\frac{kl_u}{r} \geq 22 \qquad \text{Equation 2.4}$$

with Equation 2.3 applying to columns braced against side-sway and Equation 2.4 for unbraced columns. These provisions are in place to prevent tension failures in FRP reinforcement and buckling of slender columns. However, these measures have an added level of conservativeness.

Afifi (2013) tested 27 large-size circular columns, 12 of which were reinforced with GFRP longitudinal and transverse reinforcement. Specimens had a diameter of 300 mm and a length of 1,800 mm. The columns were cast with concrete of compressive strength of 42.9 MPa, reinforced with a No. 3 spiral at an 80 mm pitch. The longitudinal reinforcement ratio was varied to study its effect on the performance of the concentrically loaded columns. The configurations used were 4-No.5, 8-No.5 and 12-No.5 GFRP sand-coated bars. The effectiveness of GFRP bars in resisting

compression was verified as the compressive strains developed in the bars were 75% of the ultimate strain. Furthermore, significant improvements were observed to the ductility of the columns as the amount of reinforcement was increased. However, the strength gain of the columns was found to be slight.

The effectiveness of GFRP is more pronounced under lateral loading. As shown in Ali and El-Salakawy (2016), three of eight columns cast with 40 MPa concrete were loaded with a similar load level and were tested under cyclic loading. The columns were 350 mm in diameter and 1,650 mm in height. The transverse reinforcement was kept constant while the longitudinal reinforcement ratio was varied; ratios of 1.3, 1.9 and 2.6% were used. It was apparent that as the longitudinal reinforcement ratio was increased, the lateral resistance saw slight improvements, with values of 167, 170 and 190 kN for reinforcement ratios 1.3, 1.9 and 2.6% respectively. Furthermore, a reduction in the drift ratio of the columns was observed and hysteretic loops produced were narrower, therefore indicating a reduction in cumulative energy dissipation.

Similarly, Elshamandy et al. (2018) tested 11 square columns with dimensions of 400 mm and a height of 1,850 mm. The researcher increased the reinforcement ratio in addition to the volumetric ratio of the transverse reinforcement. This increase in reinforcement resulted in an increase in ultimate strength and energy dissipation. The differences in both findings could be attributed to the difference in the behaviour of the two different cross-sections. Moreover, the improvement in the latter was due to the increase of both lateral and longitudinal reinforcement, which improved the overall core confinement.

Eccentrically loaded columns have also been tested by Hadhood et al. (2017) and Guérin et al. (2018). The first study was done on circular columns of diameter 305 mm and length of 1,500 mm,

and the second with 405 × 405 mm square columns with a length of 2,000 mm. Both studies show that increasing the longitudinal reinforcement ratio showed strength increase in the columns. However, the increase was slight. In the 2018 study, the increase was greater at higher eccentricities. They also concluded that the code provision requiring a minimum reinforcement ratio of 1% seemed to be adequate to prevent failure of the reinforcement bars on the tension side.

3. EXPERIMENTAL PROGRAM

3.1 General

As recommended in literature, more research is required to better understand the behaviour of GFRP-RC columns where there seems to be a lack of research in the area of HSC internally reinforced with GFRP material. In light of that, this study was designed to investigate the behaviour of HSC circular columns reinforced with GFRP bars and spirals. The results of this study would help produce a new confinement model and provide data for analytical models in future research.

3.2 Experimental Work

This study consisted of the construction and testing of fifteen HSC circular columns: fourteen reinforced with GFRP bars and spirals in addition to one (control) steel-RC column ($\lambda = 20$). The columns had a diameter, D = 350 mm and lengths of 1,250, 1,750 and 2,450 mm representing slenderness ratios of 14, 20 and 28, respectively. The columns were longitudinally reinforced with a ratio of 1.21 % and transversely reinforced with spirals of either 85 or 50 mm pitch corresponding to a reinforcement ratio of 1.11 or 1.43%, respectively. Each of the columns was fully reinforced with the respective reinforcement type. The columns were tested under monotonic eccentric-axial or flexural loading.

The following sections present in detail the properties of materials, reinforcement arrangement, instrumentation and loading procedures.

3.3 Concrete

Normal weight, ready mix concrete with a target 28-day compressive strength of 60 MPa was used. The actual strength of the concrete was determined on the day of column testing. This was determined by testing 100×200 mm standard cylinders that were taken from each batch of concrete according to CSA A23.1/2-19 standards (CSA 2019a).

3.4 Column Reinforcement

A control specimen was constructed with steel reinforcement; both longitudinal bars and confining spirals. Grade 400 steel was used and tested to determine its properties. The properties of the GFRP, however, were provided by the manufacturer. Table 3.1 summarises the properties of reinforcement.

Table 3.1 Mechanical properties of reinforcement

Bar No.	Bar diameter (mm)	Area of Bar (mm^2)	Modulus of Elasticity (GPa)	Tensile strength (MPa)	Ultimate strain (%)
Steel					
No. 10M	11.3	100	200	470 (yield)	$\varepsilon_y = 0.235$
No. 15M	15.9	200	200	480 (yield)	$\varepsilon_y = 0.240$
GFRP					
No. 10 (spirals)	9.5	71	50	1,022 (ultimate)	2.00
No. 16	15.9	199	62	1,184 (ultimate)	1.89

3.5 Test Matrix and Specimen Preparation

The test matrix was designed to measure multiple variables including:

- Reinforcement type (steel and GFRP).

- Spiral pitch (50 and 85 mm).
- Slenderness ratio, $\lambda = k\ell/r$ (14, 20 and 28).
- Eccentricity, e (60, 90, 120 and 150 mm; resulting in e/D ratios of 0.17, 0.26, 0.34 and 0.43, respectively).

In addition to the axially-loaded columns listed above, two columns were tested under pure flexure (FL).

The name of the specimens consisted of four parts. The first one is a letter (G; denoting GFRP or S; denoting Steel reinforcement). The second part is a numerical value expressing the pitch of the transverse reinforcement in mm (50 or 85). The third term denotes the slenderness ratio (14, 20 or 28). The fourth represents the eccentricity in mm at which the load is applied or if the column is under pure flexure (E60, E90, E120, E150 or FL). For example, Specimen G50-20-E60 represents a GFRP-RC column with a spiral pitch of 50 mm, λ= 20 and subject to an axial load at 60 mm eccentricity.

The specimens were divided into four series as shown in figure 3.2. The first series consisted of two columns: a control steel-RC column (85-mm spiral pitch) and a GFRP-RC column (50 mm spiral pitch). These columns were compared with specimen G85-20-E60. The second series had three GFRP-RC short columns ($\lambda = 14$) with a spiral pitch of 85-mm and different load eccentricity (60, 90 and 120 mm). The third series had 5 GFRP-RC columns ($\lambda = 20$) with a spiral pitch of 85 mm and different eccentricities (60, 90, 120 or 150 mm) and a pure flexural load case. The fourth and final series had 5 slender GFRP-RC columns ($\lambda = 28$) with a spiral pitch of 85-mm having eccentricities (60, 90, 120, 150 mm) and a column under pure flexure. To avoid premature failure,

the columns ends were covered with a specially fabricated steel collar to increase confinement in the end regions.

In total, there are three columns with λ = 14, seven with λ = 20 (six GFRP-RC columns and one steel-RC) and five slender columns with λ = 28.

Table 3.2: Test matrix and specimen details

Series	**Specimen ID**	**λ**	**Longitudinal Reinforcement**	**Transverse Reinforcement**	***e* (mm) [*e/D* ratio]**	f'_c **(MPa)**	**Variables**
			ρ_l **(%) [configuration]**	ρ_s **(%) [pitch (mm)]**			
I	S85-20-E60	20	1.21 [6-15M]	1.43 [85]	60 [0.17]	58.2	Reinforcement type and spiral pitch (control)
	G50-20-E60		1.21 [6-No.15]	1.89 [50]	60 [0.17]	59.4	
II	G85-14-E60	14		1.11 [85]	60 [0.17]	57.1	Short column behavior
	G85-14-E90				90 [0.26]	64.3	
	G85-14-E120				120 [0.34]	56.0	
III	G85-20-E60	20			60 [0.17]	60.3	Slenderness ratio limits (compared with Series II) and *e/D* ratio
	G85-20-E90				90 [0.26]	57.0	
	G85-20-E120				120 [0.34]	65.0	
	G85-20-E150				150 [0.43]	58.0	
	G85-20-FL				∞ [∞]	65.0	
IV	G85-28-E60	28			60 [0.17]	64.0	Slender Column behaviour (Compared to Series II) and *e/D* ratio
	G85-28-E90				90 [0.26]	64.3	
	G85-28-E120				120 [0.34]	65.4	
	G85-28-E150				150 [0.43]	66.4	
	G85-28-FL				∞ [∞]	72.0	

All columns were used to construct a “knee-shaped” interaction diagram for each respective slenderness ratio. Columns in Series I were compared with specimen G85-20-E60 to examine the effect of changing the spiral pitch and the type of reinforcement on the behaviour of the column. The results of Series II were used to test the effect of the level of eccentricity on short columns. A similar comparison with series III and IV for their respective slenderness ratios. The last parameter, that is slenderness ratio, was studied from the combination of results of Series II and III (λ = 14 and 20) and the combination of series III and IV (λ = 14 and 28). The test matrix is summarised in Table 3.2 and the detailing of the columns is shown in Figures 3.1-3.3.

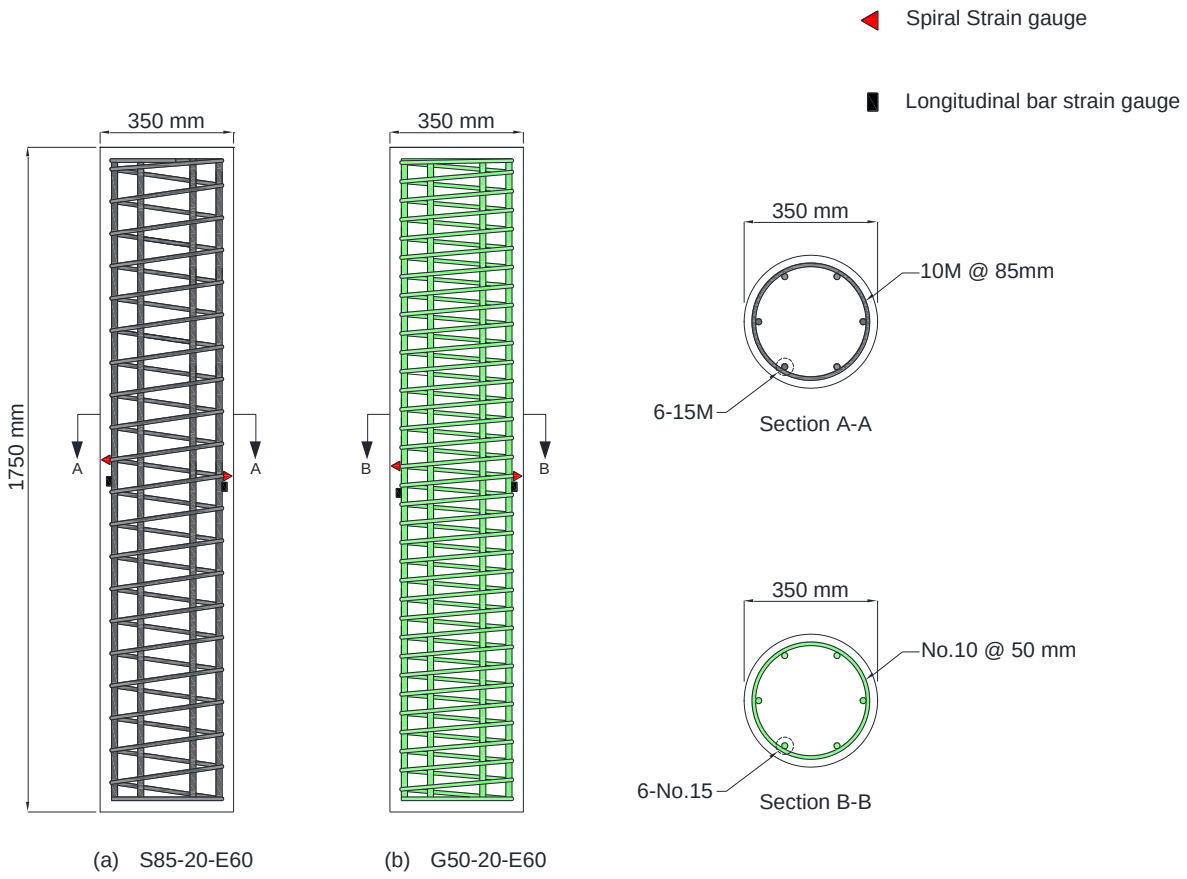

Figure 3.1: Reinforcement detailing for specimens of series I

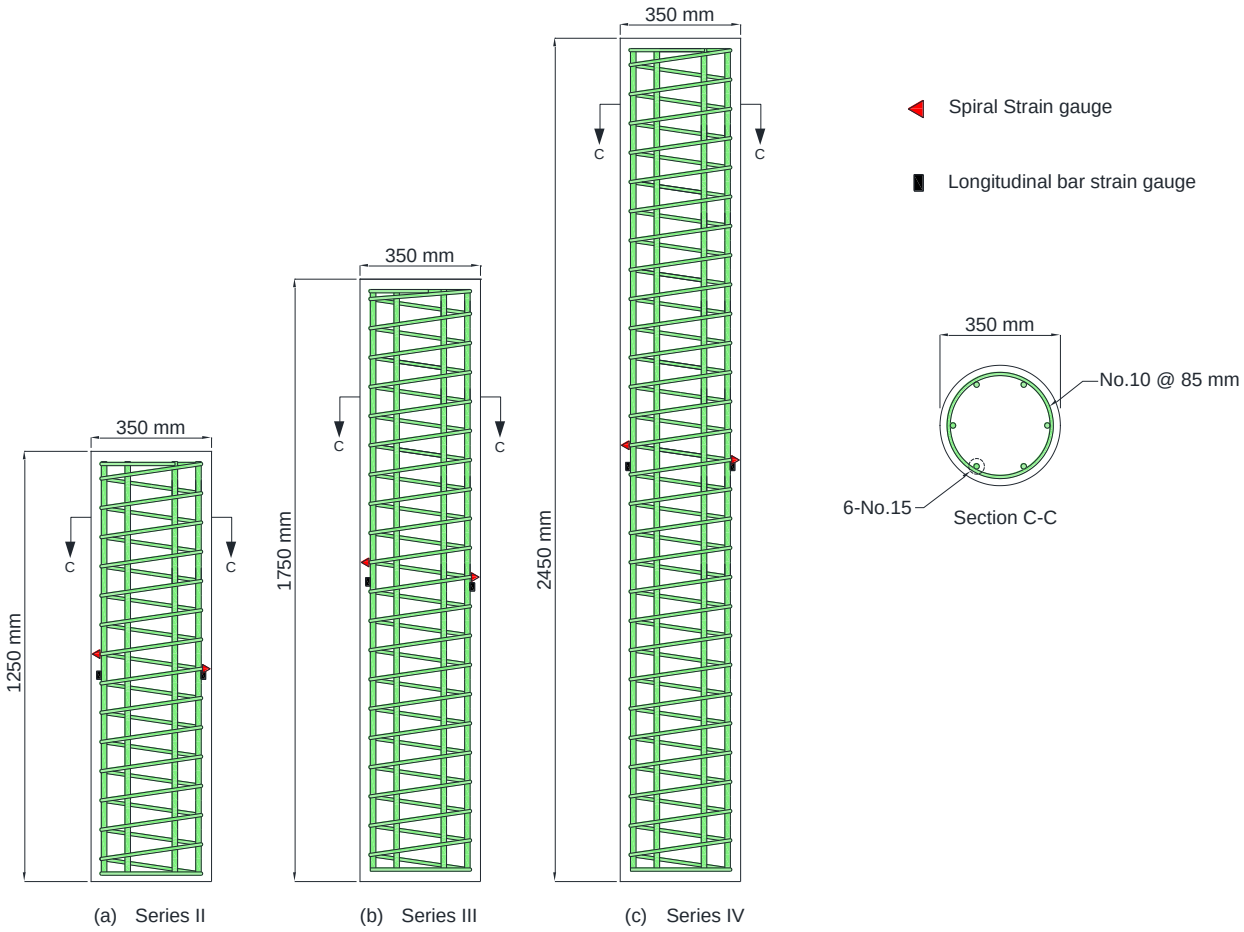

Figure 3.2: Reinforcement detailing for specimens of series II, III and IV

3.6 Construction of Specimens

Each column was constructed using stiff one-piece sonotubes and were cast vertically. The reinforcement cages were prepared and then inserted into the sonotubes, while ensuring a clear concrete cover of 25 mm from the face of the spiral reinforcement is maintained. The formwork was braced in a vertical position by a set of additional wooden forms that were also anchored to the casting platform. Concrete used to cast these columns was provided by a local ready-mix supplier; cylinder strength tests were carried out to measure the compressive strength on the day

of testing. The columns were cured for 7 days after casting. Prior to the test, the column ends were grouted to ensure uniform distribution of stress applied by the MTS machine.

3.7 Instrumentation

Each specimen was fitted with 8 internal strain gauges (Figure 3.3); measuring the strain in the longitudinal and transverse reinforcements. On the column outer surface, 2 Linear Variable Displacement Transducers (LVDTs) and 2 concrete strain gauges were installed. Additionally, 2 PI-gauges were installed at the locations of the concrete strain gauges (Figure 3.4). Along the length of the column, 5 LVDTs were placed at a spacing of $L/4$; this measured horizontal displacement as shown in Figures 3.4, 3.5 and 3.6. The strain gauges attached to the transverse reinforcement were attached at the extreme tension and compression locations of the centre-most loop. The longitudinal reinforcement strain gauges were attached to all reinforcement levels with a backup gauge on the compression-most as well as the tension-most bars. The external gauges (LVDTS, concrete strain gauges and PI-gauges) were also placed at the most critical location that is the column mid-height. Figure 3.4 illustrates the middle 1,000 mm of the columns, where the instrumentation mentioned above was located.

3.8 Test Setup and Loading Procedure

Thirteen specimens were tested under eccentric loading and two under pure flexure. The load was applied using a 5,000-kN capacity MTS machine. Heavy steel collars were used at the top and bottom of the axially-loaded specimen to help prevent premature failure as shown in Figure 3.5. In the case of the flexural test, the load was applied at two points with the column simply supported as shown in Figure 3.6.

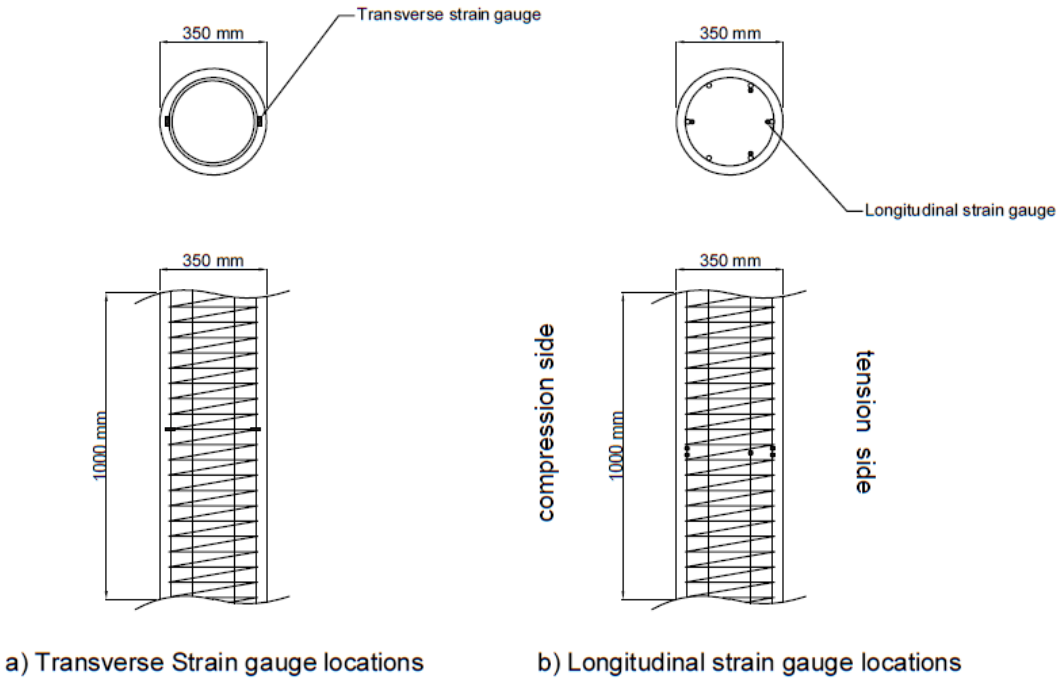

Figure 3.3: Location of internal instrumentation (reinforcement strain gauges)

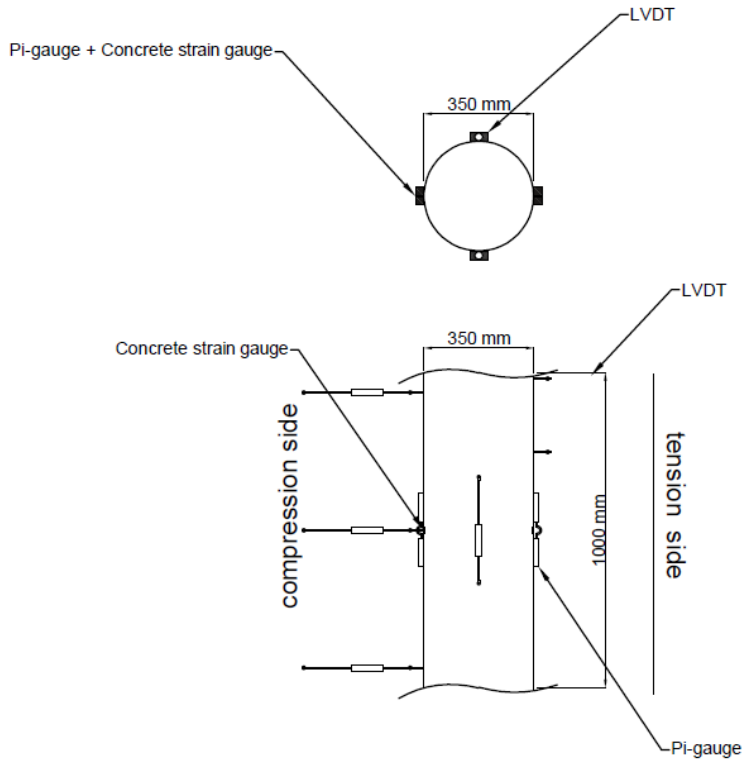

Figure 3.4: Location of external instrumentation

The load was displacement-controlled at a rate of 1.5 mm/min. The MTS machine is equipped with a built-in load cell; this was used to obtain the axial load applied to the column. All strains, displacements, and loads were automatically logged into a Data Acquisition System (DAQ) and were recorded and stored on a personal computer.

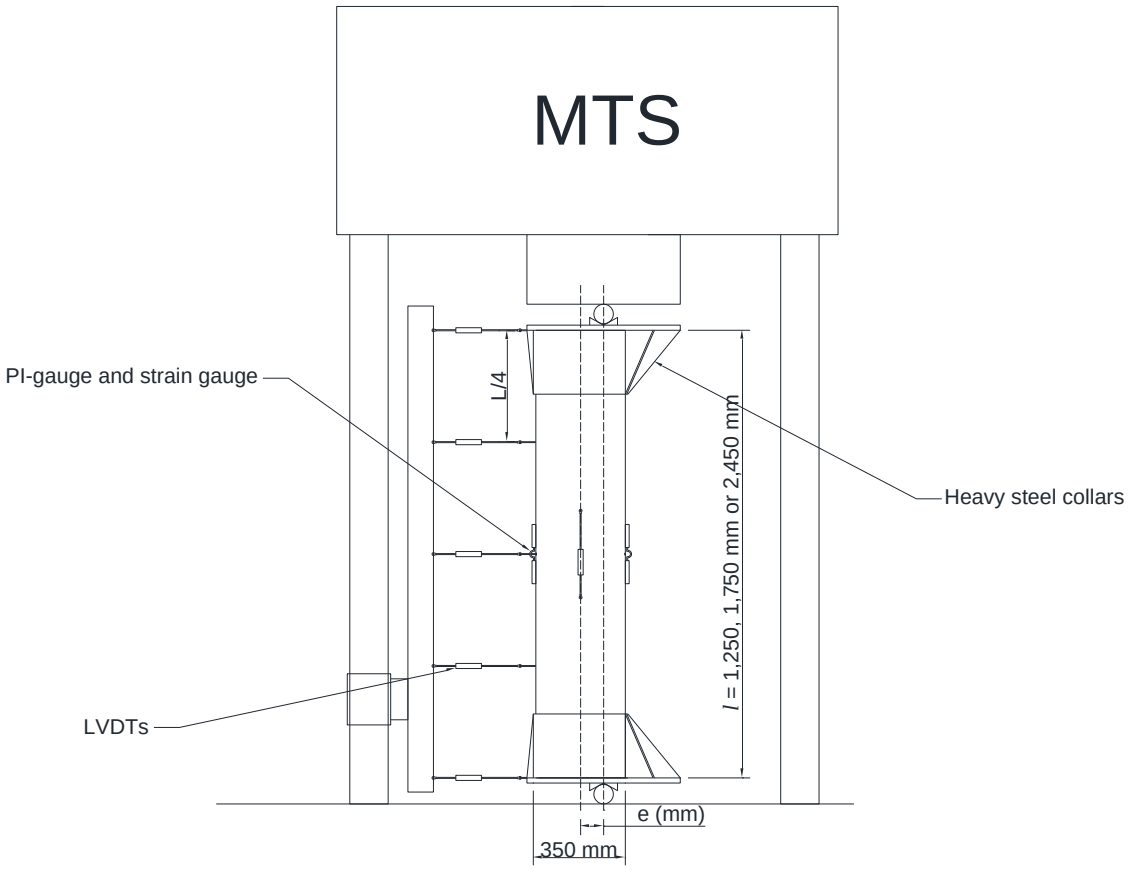

Figure 3.5: Axial loading test setup schematic

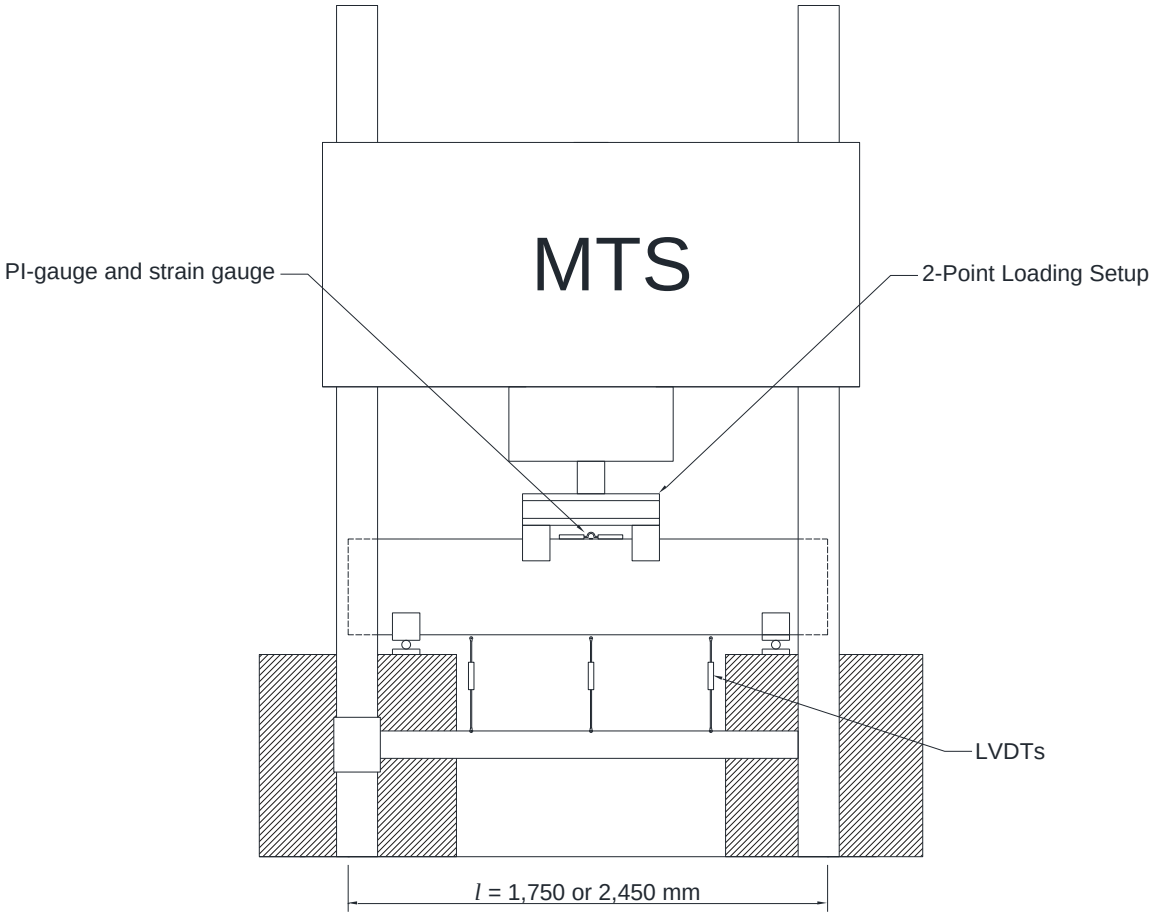

Figure 3.6: Flexure test setup schematic

4. EFFECT OF SLENDERNESS RATIO ON GFRP-REINFORCED HIGH STRENGTH CONCRETE COLUMNS

Authors and Affiliation:

- Mu'taz Almomani, M.Sc. Student, Department of Civil Engineering, University of Manitoba.
- Karam Mahmoud, Post-Doctoral Fellow, Winnipeg, MB, Canada.
- Ehab F. El-Salakawy, Professor, Department of Civil Engineering, University of Manitoba.

Journal and Status: ACI Structural Journal, under review.

Reference:

Almomani, M., Mahmoud, K., and El-Salakawy, E. "Effect of Slenderness Ratio on GFRP-Reinforced High Strength Concrete Columns." ACI Structural Journal, Submitted in April 2021.

Note:

The manuscript had been slightly edited from the original paper by renumbering the tables and figures to include the chapter number. The specimen names in this chapter differ from the matrix in Chapter 3. The specimen names are explained in the list of abbreviations. In addition, the reference list and list of notations have been moved to the appropriate sections in the thesis as indicated in the table of contents.

4.1 Abstract

This paper presents the results of eight large-scale high strength concrete (HSC) columns reinforced internally with glass fiber-reinforced polymers (GFRP) bars and spirals. The effects of slenderness ratio and the eccentricity-to-diameter ratio (*e/D*) on the behavior of HSC columns that meet the minimum code requirements are evaluated. Test results indicated that increasing the *e/D* ratio or the slenderness ratio resulted in a decrease in the axial and lateral stiffness and the axial capacity of the HSC columns. All tested columns exhibited a material type failure, which is characterised by crushing of concrete. Furthermore, compressive strains measured in the GFRP bars indicated their contribution to column axial capacity. In addition, an interaction diagram was developed and compared to the predictions of the available codes and guidelines.

Keywords: High-strength concrete, GFRP bars and spirals, eccentric loading, bending, slender columns, short columns.

4.2 Introduction

The effectiveness of glass fiber-reinforced polymers (GFRP) reinforcement has gained increasing recognition over the past few decades. Researchers were able to verify their viability as internal reinforcement for concrete structures in comparison to their traditional steel counterpart (Ali and El-Salakawy 2016; Ghomi and El-Salakawy 2016; El-Gendy and El-Salakawy 2016; Mahmoud and El-Salakawy 2016; Hadhood 2017; Rahman et al. 2017; Abdelazim 2020). In addition, the corrosion-resistant nature of GFRP bars makes their use more favourable in structures exposed to harsh conditions (El-Salakawy et al. 2003; ACI Committee 440 2015). The inevitability of corrosion in steel-reinforced concrete (RC) means more costs are incurred in mitigating or repairing affected members (ACI Committee 222 2019). Thus, eliminating the corrodible

component of the structural element increases its service life and consequently reduces lifecycle costs.

Circular columns, compared to rectangular columns, provide uniform confinement and a more aesthetic appearance. This makes their use in structures, such as bridges and parking garages, more common. More critical to the performance of a compression member is slenderness ratio (λ), which is defined as the ratio of the member's effective length to its radius of gyration ($k\ell/r$), where k, ℓ and r are the effective length coefficient, unbraced length and radius of gyration, respectively. As the slenderness ratio increases, the column is subjected to larger lateral deflections. This creates secondary moments, which directly affects the column axial capacity (ACI Committee 318 2019). Early studies, such as Mirmiran et al. (2001), suggest that fiber-reinforced polymer (FRP)-RC columns are more susceptible to the slenderness effect due to the lower modulus of elasticity of FRP reinforcement. Therefore, it was suggested that the slenderness ratio limit for FRP-RC short columns be reduced to 17 compared to 22 for steel-RC columns. Numerous codes and guidelines are currently available providing a reference for designers to incorporate FRP into structural elements. Many of these guidelines have maintained a high level of conservativeness regarding compression members. Among other codes, the Canadian Highway Bridge Design code - CSA S6-19 (CSA 2019a) - allows the use of FRP in members subject to combined flexural and axial loads while limiting the strains in the FRP bars in compression to 0.002. On the other hand, the ACI 440.1R-15 guideline (ACI Committee 440 2015) provided recommendations not to consider FRP bars in compression members or compression zones in flexural members. Further limitations regarding slender compression members were introduced by the CSA S806-12 (CSA 2017) prohibiting the use of FRP entirely in such members.

In efforts to alleviate code restrictions, significant research has been carried out to map and define the behavior of FRP columns. The behavior of FRP-RC short columns have been studied in recent literature (De Luca et al. 2010; Afifi et al. 2013; Hadhood 2017; Barua and El-Salakawy 2020; Elchalakani et al. 2020). All the aforementioned studies showed similarity in the behavior of the FRP-RC columns and their steel-RC counterparts. Additionally, the studies presented consistent data showing a small increase in axial capacity and a more pronounced increase in ductility with increasing of FRP longitudinal and transverse reinforcement under different eccentricities. However, recent studies have focused on slender FRP-RC members due to the increasing need of FRP materials in a wider range of structural applications. Abdelazim (2020), Khorramian et al. (2020) and Barua et al. (2021) investigated normal strength concrete (NSC) slender columns reinforced with GFRP bars. They found that the mode of failure of columns with lower eccentricities showed a material type failure characterised by the crushing of the concrete. However, larger eccentricities caused the columns to fail due to the development of excessive cracks on the tension side. As expected, the studies showed that for the same *e/D* ratio, the lateral displacements in the slender columns are consistently higher than those observed in the short columns. These conclusions were similar for rectangular and circular columns. Barua et al. (2021) compared slender columns ($\lambda = 28$) and short columns ($\lambda = 20$); as defined by current codes. The study found that changing the slenderness ratio from 20 to 28 showed a greater difference for results of steel-RC columns than GFRP-RC columns. Barua et al. (2021) suggested that this difference was due to that the steel-RC columns exhibited distinct short and slender behavior, respectively. However, the GFRP-RC columns were similar as both slenderness ratios exhibited slender behavior, suggesting the limit for GFRP-RC columns is lower than the 22 in codes, which is in agreement with the findings of Mirmiran et al. (2001).

Very limited research has been conducted to investigate the behavior of HSC slender columns reinforced with GFRP bars (Hales et al. 2016; Abdelazim 2020). Hales et al. (2016) studied HSC circular columns measuring 305 mm in diameter and 760 and 3,730 mm in height (λ = 10 and 49, respectively) and with reinforcement ratios of 1.65 and 2.71%. Abdelazim (2020) tested specimens with the same diameter, however, with a column length of 2,500 mm (λ = 33) and reinforcement ratios of 3.28 and 4.66%. Hales et al. (2016) stated that for low *e/D* ratios (up to 8.3%), both short and slender columns exhibited a failure that was initiated by crushing of the concrete, followed by the rupture and buckling of the spirals and the compression bars, respectively. In contrast, higher *e/D* ratio (33%) in slender columns showed much higher deflection at mid-height and exhibited a buckling (stability-type) failure. Conversely, Abdelazim (2020) found that slender columns showed no signs of stability-type failure. All columns failed due to concrete crushing, which is a material-type failure.

Available literature has provided a solid foundation for the use of FRP in RC columns. However, due to the brittle nature of HSC, many aspects such as ductility, effect of slenderness and eccentricity of the applied axial load and the reinforcement ratio still need to be further investigated. In addition, columns designed for the minimum reinforcement requirements are common in buildings. Broms and Viest (1961) stated that the minimum reinforcement ratio is more critical for slender columns where a decrease in the proportion of the load carried by the reinforcement leads to a less stable column. Therefore, further research is required to fully understand the behavior of such columns and to ease the level of conservativeness of related provisions in the codes and guidelines.

4.3 Research Significance

Despite the studies conducted on NSC columns reinforced with GFRP bars, gaps are still present in areas pertaining to HSC columns due to the different nature of the material. Additionally, previous literature has pointed to key differences between short and slender columns with recommendations of reducing the slenderness ratio limit to 17. Furthermore, FRP design codes and guidelines remain cautious when approaching compression members, especially slender ones. This study aims to experimentally investigate HSC short and slender columns reinforced with GFRP bars and spirals that meet the minimum code requirements under axial load with different eccentricities.

4.4 Experimental Program

4.4.1 Specimen configuration and details

In this study, a total of eight large-scale concrete columns were constructed and tested to failure. The columns were reinforced with sand-coated GFRP bars and spirals. The columns were designed in accordance with the Canadian standards CSA S806-12 (CSA 2017). The columns were cast with HSC concrete and had a diameter of 355-mm. The height of the columns was either 1,250-mm or 2,450-mm corresponding to λ of 14 and 28, respectively. According to the CSA S806-12 (CSA 2017), short columns are defined as those with a $\lambda \leq 22$. However, as mentioned earlier, recent literature recommended reducing the limit of the short column from 22 to 18 (Abdelazim 2020). Consequently, the columns presented in this study are designed to investigate slenderness ratios that are defined as short and slender in accordance with both, the current definition of slender and short compression members and the recommendations in the literature. Throughout this paper, the columns with $\lambda = 14$ will be referred to as “short” and those with $\lambda = 28$ will be referred to as “slender”. Furthermore, the CSA S6-19 (CSA 2019a) specifies that the smallest permissible

length-to-diameter ratio of a column is 2.5, which is satisfied by the specimen dimensions selected. The cross-sectional diameter of the columns is greater than 300 mm and the longitudinal and transverse reinforcement ratios meet the minimum requirements for reinforcement ratio, number of bars and spiral pitch specified by the CSA S806-12 (CSA 2017).

The specimens were longitudinally reinforced with 6-No.16 GFRP bars and transversely with No.10 GFRP spirals spaced at 85-mm as shown in Fig. 4.1.

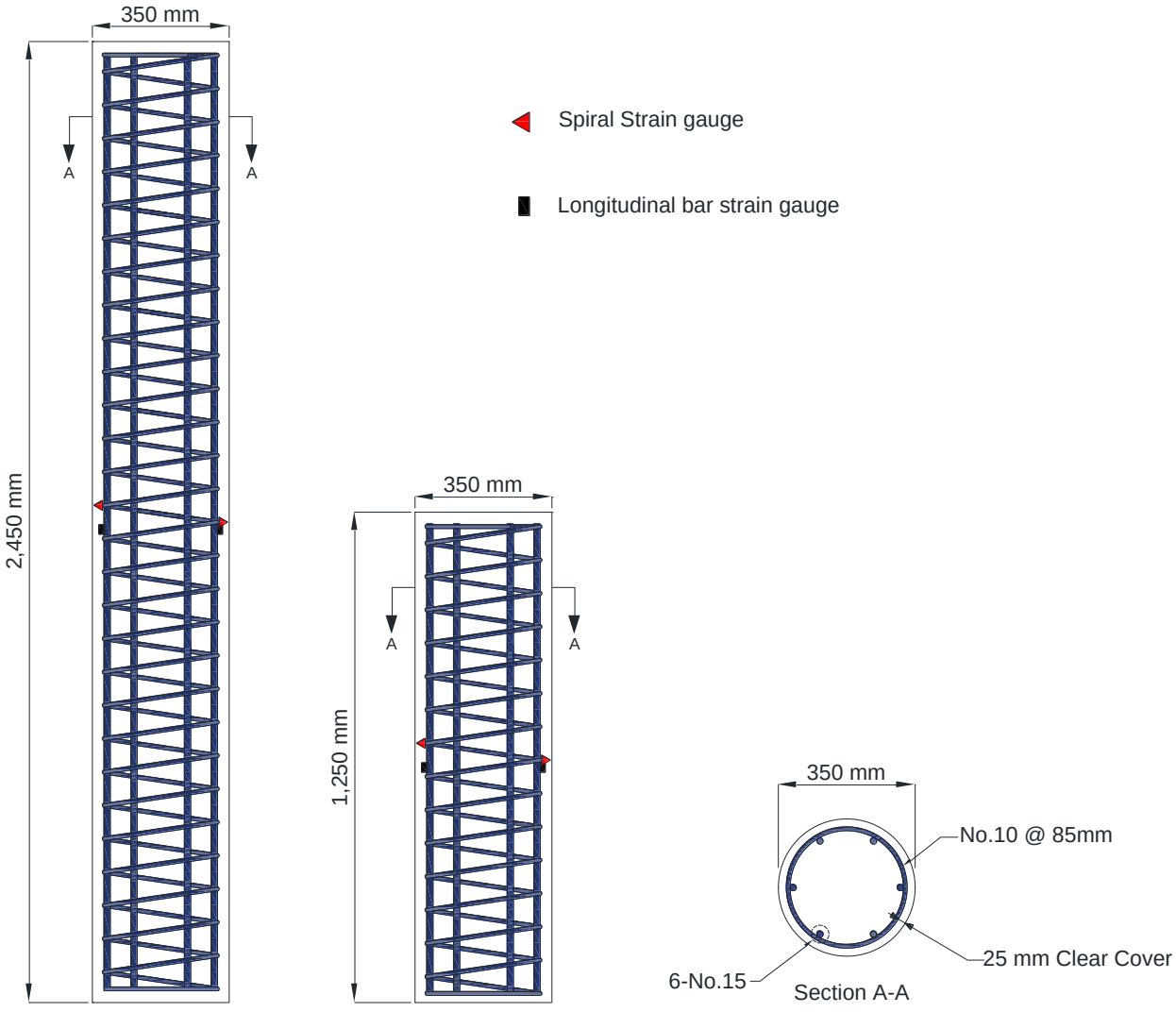

Figure 4.1 – Details of columns and GFRP reinforcement *(Note:* 1 *mm* = 0.0394 *in.)*

The axial load eccentricities were 60, 90, 120 and 150 mm corresponding to *e/D* ratio of 0.17, 0.26, 0.34 and 0.43, respectively. In addition to the axial loading, a column tested under pure flexural loading was investigated in the study. The name of the specimen consists of two parts. The first part denoted by S28 or S14 for slender (λ = 28) and short (λ = 14) columns, respectively. The second part represents the type of loading, where "FL" corresponds to flexural loading and "60", "90", "120" and "150" represent the eccentricity at which the load was applied. The details of specimens are summarised in Table 4.1.

Table 4.1: Test matrix

Specimen ID	f'_c (MPa)	Long. reinforcement		Transverse Reinforcement		λ	e (mm)	e/D
		No. of bars	ρ_f, (%)	Pitch (mm)	ρ_{fs}, (%)			
S14-60	57.1	6-No. 16	1.21	85	1.43	14	60	0.17
S14-90	64.3						90	0.26
S14-120	56.0						120	0.34
S28-60	64.0					28	60	0.17
S28-90	64.3						90	0.26
S28-120	65.4						120	0.34
S28-150	66.4						150	0.43
S28-FL	72.0						∞	∞

Note: 1 *mm* = 0.0394 *in.*; 1 *MPa* = 0.14504 *ksi*

4.4.2 Material properties

The columns were cast with ready-mix concrete with a target 28-day strength of 60 MPa. The nominal aggregate size used was 20 mm. Standard cylinders, 100×200 mm, were cast and tested

in accordance with CSA A23.1/2-19 (CSA 2019c) to determine the strength of the concrete on the same day the columns were tested. The concrete strength obtained for each specimen is listed in Table 1. The average of concrete strength obtained for all columns was 63.7 MPa. The columns were reinforced with pultruded, sand-coated GFRP bars and spirals. The properties of the GFRP reinforcement were provided by the manufacturer (Pultrall Inc. 2019), as shown in Table 4.2. The manufacturer obtained the properties through certified tests that were carried out according to the CSA S807-19 standards (CSA 2019e).

Table 4.2: Mechanical properties of GFRP reinforcement

Bar Size	Nominal Diameter (mm)	Area (mm^2)		Elastic tensile modulus (GPa)	Tensile strength (MPa)	Ultimate strain (%)
		Nominal	Annex A*			
No. 16 (Straight bar)	15.9	199	235	64±1.49	1,558±46.8	2.40
No. 10 (Spiral)	9.5	71	83	58±1.50	667±41.3	1.14

* Area according to test method in CSA/S806 Annex A.
Note: 1 *mm* = 0.0394 *in.*; 1 *GPa* = 145.04 *ksi*; 1 *MPa* = 0.14504 *ksi*; 1 mm^2 = 0.00155 in^2.

4.4.3 Test setup and procedure

The columns were tested using a 5000-kN capacity hydraulic machine. The load was applied at a displacement-controlled rate of 1.5 mm/min. The columns tested under axial loading were fitted with two heavy steel collars and were grouted to ensure confinement of the column ends. A pin-pin boundary condition was simulated by welding a pin and socket to collar and the loading machine, respectively, to ensure no transfer of moment. The location of the pin on the collars varied to achieve the required load eccentricity. A 25% drop in the column axial load marked the end of the test. The flexural setup consisted of two supports and two points of loading. The four loading points were fitted with semi-circular saddles ensuring full contact to the column. The load

was applied through a spreader beam to which the loading saddles were connected. The testing setup is depicted in Fig. 4.42.

4.4.4 Instrumentation

The behavior of columns was monitored using various internal and external instrumentation. The GFRP bars and spirals were fitted with several strain gauges to measure the strains on the tension and compression sides. In addition, a strain gauge and a PI-gauge were mounted on the concrete surface on the compression side to measure the compressive strains. The deflected shape of the column was measured using five linear variable displacement transducers (LVDTs). One LVDT was placed at mid-height and the remaining were evenly distributed along the length of the column. Furthermore, two LVDTs were also placed to measure the axial displacement of the columns. Similar instrumentation was used for the column under pure flexure. However, only three LVDTs were used to measure the deflection. The instrumentation for the two test setups is shown in Fig. 4.2.

4.5 Experimental Results and Conclusion

4.5.1 General behavior and modes of failure

The observed modes of failure for all specimens were material-type failure. As the specimens reached their peak loads, the concrete cover began to spall, and load immediately dropped. Figure 4.3 shows the tested specimens at failure. For specimens S28-60 and S14-60, no cracks were observed until failure. Tension cracks formed simultaneously with the crushing of the concrete on the compression side. Following the crushing of the concrete, S14-60 was the only specimen, which showed buckling of the GFRP bar and rupture of the confining spiral at the same location on the compression side. This was due to the additional compression stresses on the confined core as the cover spalled. As the eccentricity increased, the columns began to show earlier signs of

cracking attributed to the increased lateral deflections. The remaining short specimens showed cracks at 550 and 290 kN for specimens S14-90 and S14-120, respectively. The slender columns showed the first crack at much lower loads (390, 170 and 150 kN for specimens S28-90, S28-120 and S28-150, respectively). Those observations also show that for the same *e/D* ratio, the slender columns experienced tension cracks earlier than the short column counterparts. This was due tension cracks being influenced predominantly by the *e/D* ratio for short columns, however, for the "S28" series, this was influenced by the *e/D* ratio and the additional moment due to the slenderness effect.

4.5.2 Effect of eccentricity

The eccentricity, at which the load was applied, varied from 60 to 150 mm, which corresponds to an *e/D* ratio of 0.17 to 0.43. As expected, when the eccentricity increased, the axial capacity decreased, which is a direct consequence of the substantial increase in the moment on the column. Since the concrete strength varied between columns, the experimental axial loads were normalised using a factor of $63.7/f'_c$, where 63.7 MPa represents the average of the concrete strength of all columns. The normalised axial capacities for the "S28" series were 3,247, 2,383, 1,470 and 1,023 kN for the columns with an *e/D* ratio of 0.17, 0.26, 0.34 and 0.43, respectively. This represents a decrease of 26.6, 54.7 and 68.5% in the axial capacity compared to that of column S28-60. Similarly, the "S14" series capacities were 4,079, 3,047 and 1,890 kN for columns S14-60, S14-90 and S14-120, respectively. The effect of changing the *e/D* ratio, for both values of λ, showed very similar decrease in the overall capacity of the column; however, at greater loads for the short columns in general. This is due to the increased applied moment as the *e/D* ratio increased for both column slenderness ratios.

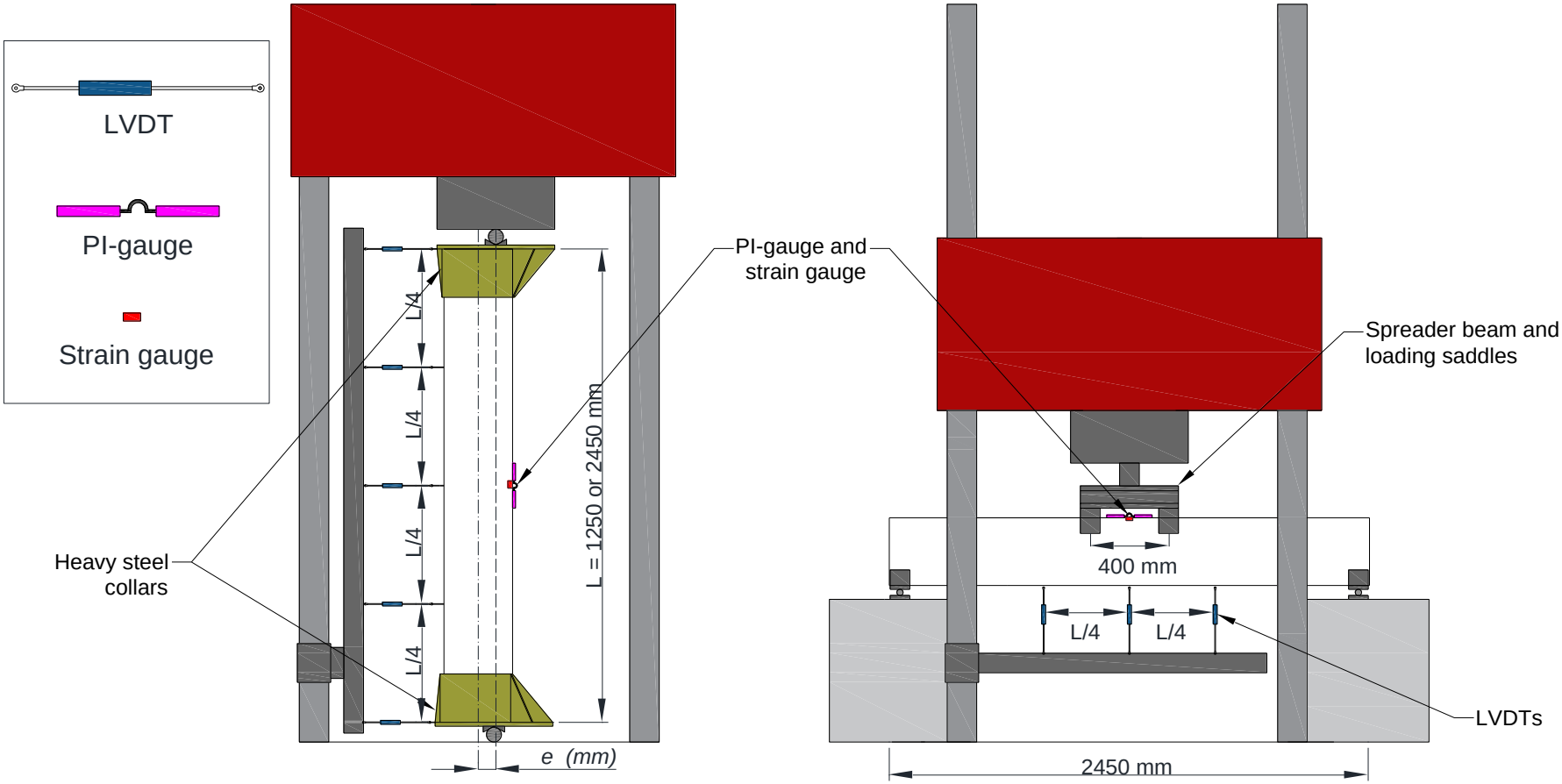

(a) Axially-loaded column test setup (b) Flexural test setup

Figure 4.2 – Test setup and external instrumentation *(Note:* 1 *mm* = 0.0394 *in.)*

Figure 4.3 – Mode of failure for all test specimens

The effect on the capacity was similar for both series, however, the disparity in the overall capacity was due to the slenderness effect, which reduced the axial capacity of the slender columns greatly. As the axial capacity decreased, the moment increased indicating the change of *e/D* from 0.17 to 0.26 was still above the theoretical balance point found on a typical axial load-bending moment interaction diagram. Further decrease in the axial capacity (or increase in *e/D*) resulted in a consistent decrease in the moment at failure. Results of all specimens are presented in Table 4.3.

Barua et al. (2021) tested NSC columns with identical dimensions and $\lambda = 28$. It was observed that increasing the *e/D* ratio from 0.0 to 0.085 and further to 0.17 and 0.34 caused a decrease in the specimen axial load capacity by 29, 37 and 69%. In addition, increasing the *e/D* ratio from 0.17 to 0.34 resulted in a 46% reduction in the axial capacity, which is less than the 54.7% observed for HSC columns in the current study. On the other hand, for slender columns ($\lambda = 33$) with 80 MPa concrete strength, Abdelazim (2020) reported similar decrease in the axial capacity of 52% when the *e/D* ratio increased from 0.16 to 0.33 and 0.66, respectively. This means that the axial capacity of GFRP-RC columns is significantly affected by the concrete strength.

Figure 4.4 shows the measured strains in the GFRP bars. Strains in the outermost bars on the tension side increased linearly up to the peak load as the *e/D* ratio increased. As can be seen in Fig. 4.4, the tensile strains in the bars for the "S28" series at peak load were 480, 2,020, 3,820 and 7,490 με for *e/D* ratio of 0.17, 0.26, 0.34 and 0.43, respectively. This was due to the reduced depth of the compression zone in the concrete with increasing the eccentricity. The increase in the moment because of increasing the eccentricity means the neutral axis shifted further towards the compression side, thus increasing the tensile force in the tension side. However, the compressive strains in the compression side bars were very close in value and approaching the maximum design compressive strains of the outer compression fiber of the concrete.

Table 4.3: Test results

Specimen ID	f'_c (MPa)	e (mm)	δ (mm)	P_u (kN)	P_u* (kN)	M_{u1}*(kN.m) [$P_u \times e$]	M_{u2}* (kN.m) [$P_u^* \times (e+\delta)$]
S14-60	57.1	60	2.36	3,657	4,079	244.7	255.3
S14-90	64.3	90	3.75	3,076	3,047	274.2	285.7
S14-120	56.0	120	5.30	1,662	1,890	226.8	236.1
S28-60	64.0	60	8.90	3,264	3,247	194.8	223.6
S28-90	64.3	90	9.80	2,406	2,383	214.5	237.8
S28-120	65.4	120	15.60	1,510	1,470	176.4	199.3
S28-150	66.4	150	24.50	1,056	1,023	152.0	176.7
S28-FL	72.0	∞	71.30	-	-	-	133.1

*Normalized Ultimate load and moments using the average concrete strength.
Note: 1 kN = 0.2248 kip; 1 mm = 0.0394 in.

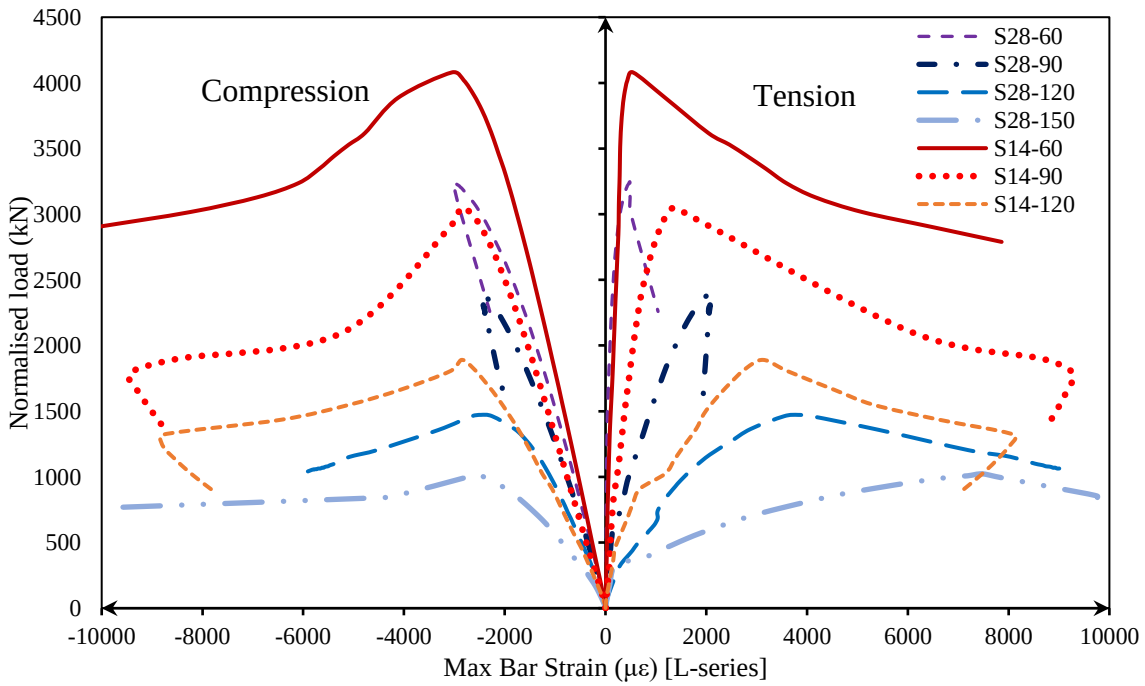

Figure 4.4 – Strains in longitudinal bars in axially-loaded columns *(Note:* 1 *kN* = 0.225 *kip)*

The measured strain on the bar on the compression side was -3,020, -2,400, -2,480, -2,640 με for columns with *e/D* ratio of 0.17, 0.26, 0.34 and 0.43, respectively. Similarly, for the "S14" series, an increase can be seen in the strain measured in the bar on the tension side when increasing the *e/D* ratio. These tensile strains were 550, 1,390 and 3,130 με in columns with *e/D* ratio of 0.17, 0.26 and 0.34, respectively. Correspondingly, the compressive strains in the GFRP bars were -3,050, -2,880 and -2,860 με in columns S14-60, S14-90 and S14-120, respectively.

Concrete compressive strains (Fig. 4.5) were close to or exceeded the design strains of -3,000 με specified in the ACI 440.1R-15 (ACI 2015) and -3,500 με specified in the CSA S806-12 (CSA 2017). The concrete strains on the compression side measured -2,890, -3,120, and -3,430 με for specimens S14-60, S14-90 and S14-120, respectively, while it was -3,430, -2,530, -3,150 and -3,300 με for specimens S28-60, S28-90, S28-120 and S28-150, respectively. However, it is worth noting that some of the readings correspond to loads less than the peak load as those strain gauges malfunctioned prior to failure.

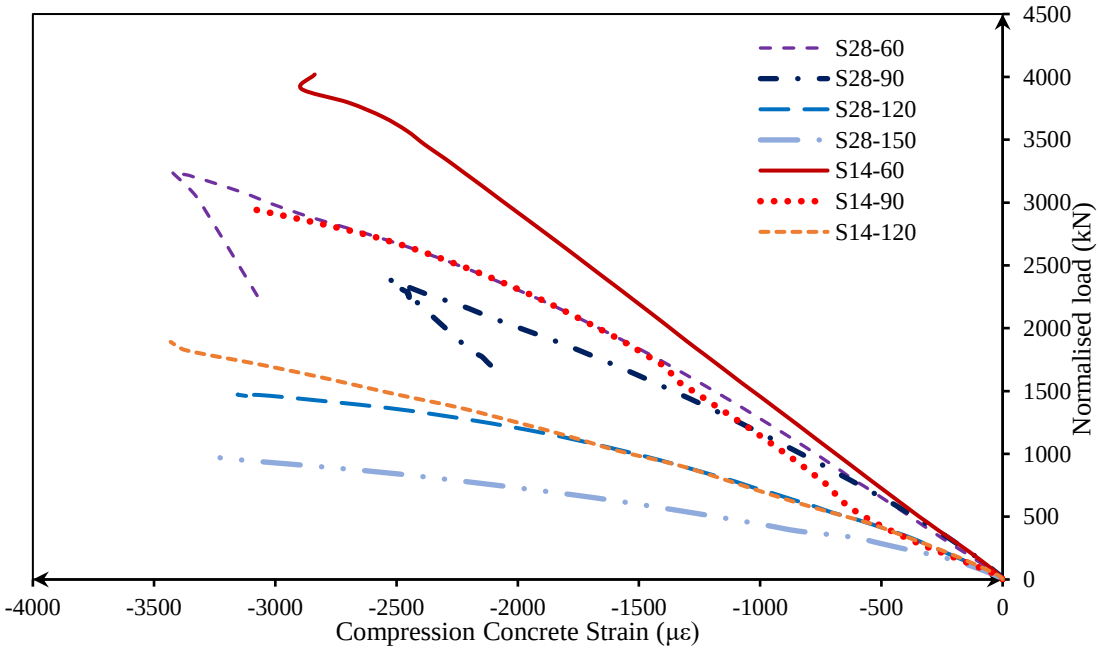

Figure 4.5 – Concrete compressive strains in axially-loaded columns *(Note:* 1 *kN* = 0.225 *kip)*

The NSC columns tested by Barua et al. (2021) with *e/D* ratios of 0.17 and 0.34 showed compression bar strains of -1,530 and -2,030 με and tension bars strains of 100 and 3,200 με, respectively. On the other hand, their HSC counterparts (S28-60 and S28-120) had strains of -3,020 and -2,480 με in compression and to 480 and 3,820 με in tension, respectively. This corresponds to an increase of 97 and 22% in compressive strain, while the increase in tensile strains were 380 and 19.5% for *e/D* ratios 0.17 and 0.34, respectively. The increased strains in the HSC columns are due to the larger column capacity. Moreover, the increase in strains associated with increasing concrete strength was greater for columns with *e/D* ratio of 0.17. This was due to the larger increase in axial capacity for specimens with lower *e/D* ratio.

As the load increased, the spiral strains increased almost linearly until approximately 80-95% of the peak load; however, the increase in strain became nonlinear prior to the peak load. The strains increased rapidly when the concrete cover spalled after the peak load was reached (Fig. 4.6). This shows that the spirals continued to confine the concrete core even after the peak load is reached.

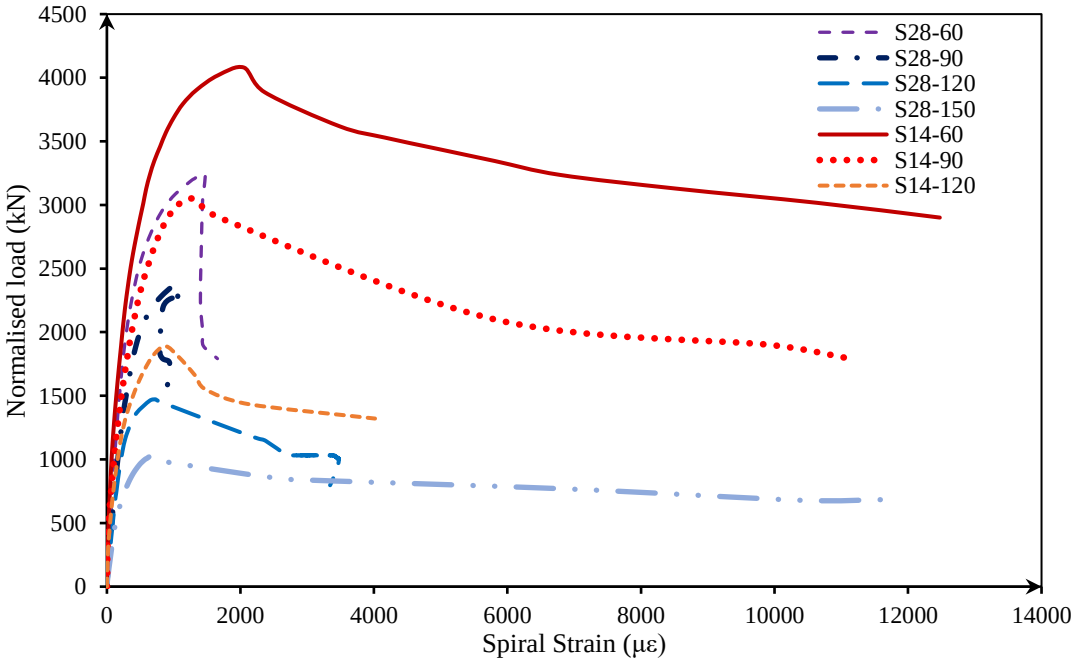

Figure 4.6 – Spiral strains in axially-loaded specimens (*Note:* 1 *kN* = 0.225 *kip)*

In general, columns having high *e/D* ratio (0.34 and 0.43) have lower load-strain slope and so the rate of increase of spiral strain is greater for those specimens. Increasing the *e/D* ratio from 0.17 to 0.26 and further to 0.34 in columns with $\lambda = 14$, decreased the spiral strains at peak load by 36.3 and 57.4%, respectively, compared to that with *e/D* of 0.17. Similarly, for slender columns ($\lambda = 28$), increasing the *e/D* ratio from 0.17 to 0.26 and further to 0.34 and 0.43, decreased the spiral strains by 29.0, 50.0 and 55.2%, respectively, compared to the specimen with *e/D* = 0.17.

Moreover, as the *e/D* increased, the lateral displacement of the columns increased. As shown in Fig. 4.7, the maximum displacement for column S28-60 (*e/D* = 0.17) was 8.87 mm. Increasing the *e/D* ratio to 0.26, 0.34 and 0.43 resulted in an increase in lateral displacement by 10.0, 74.0 and 175.0%, respectively, with reference to column S28-60. The shorter specimens, S14-60, S14-90 and S14-120, showed a lateral displacement of 2.36, 3.75 and 5.30 mm, respectively. Accordingly, the measured lateral stiffness decreased with increasing the *e/D* ratio. For short columns, the lateral stiffness decreased by 8.3 and 17.0% as the *e/D* ratio increased from 0.17 to 0.26 and further to 0.34, respectively.

The decrease in the lateral stiffness for slender columns was 15.0, 57.0 and 81.0% when the *e/D* ratio increased from 0.17 to 0.26, 0.34 and further to 0.43, respectively. This behavior was expected, as increasing the eccentricity was shifting the response of the column to a more flexural behavior. Since there was more applied bending moment, the column showed much larger deformations.

Similarly, the load-axial displacement relationship was linear up to failure as shown in Fig. 4.8. The axial displacement at the peak load decreased as the *e/D* ratio increased. The axial stiffness of the short columns decreased by 13.0 and 32.0% when the *e/D* ratio increased from 0.17 to 0.26

and 0.34, respectively. For slender columns, increasing the *e/D* ratio from 0.17 to 0.26, 0.34 and further to 0.43 resulted in a reduction in the axial stiffness by 10.0, 43.0 and 60.0%, respectively.

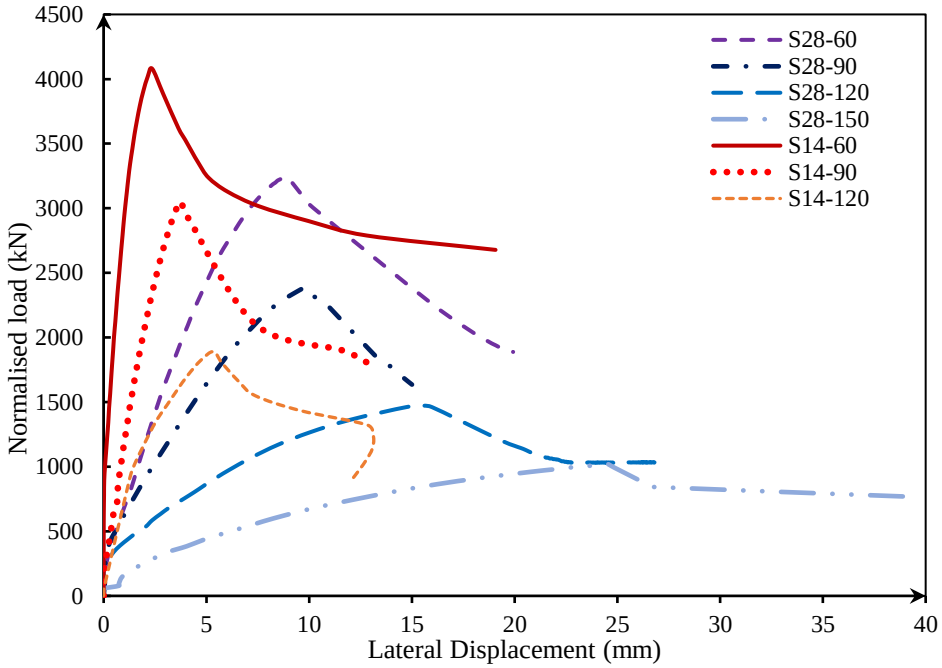

Figure 4.7 – Lateral displacement of axially-loaded columns (*Note:* 1 *kN* = 0.225 *kip;* 1 *mm* = 0.0394 *in.)*

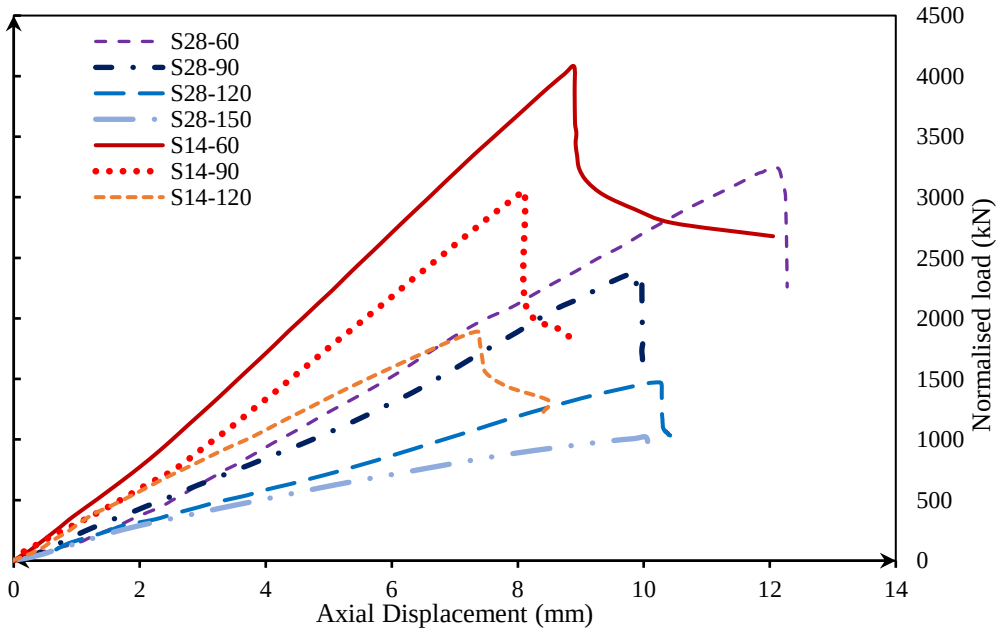

Figure 4.8 – Axial displacement of axially-loaded columns (*Note:* 1 *kN* = 0.225 *kip;* 1 *mm* = 0.0394 *in.)*

4.5.3 Effect of slenderness ratio

The increase of λ from 14 to 28 had a very significant effect on the behavior of the columns. Such increase in the slenderness ratio caused a decrease in the peak axial capacity of the columns by 20.4, 21.0 and 22.2% for columns with *e/D* ratio of 0.17, 0.26 and 0.34, respectively. This is due to the slender columns exhibiting higher lateral displacements throughout the loading, which translate to a higher secondary moment and thus reducing the axial capacity of the specimens. The decrease in axial capacity was accompanied by a decrease in the total moment capacity of 12.4, 16.8 and 15.6% for *e/D* ratios of 0.17, 0.26 and 0.34, respectively. Since the primary moment capacity is a direct product of the axial capacity and load eccentricity, the primary moment would, therefore, decrease with increasing slenderness due to the low axial load achieved by the slender columns. However, slender columns with *e/D* ratios of 0.17, 0.26 and 0.34 showed an increase in secondary moment by 172.0, 102.6 and 146.0% compared to that of their short counterparts. This shows that the increased lateral displacement of the column caused additional moments on the column and thus reduces the axial capacity.

Despite the change in the slenderness ratio, the strain developed in the bar on the compression side at peak loads for different *e/D* ratios was very similar (Fig. 4.4). These strains were in good agreement with the concrete compressive strain measured during the test. The values ranged between -2,400 and -3,050 με, which are slightly lower for the slender columns as compared to their short counterparts. The developed compressive strains suggest they have an active contribution to the axial capacity in both short and slender columns. On the other hand, short columns with higher eccentricities experienced lower tensile strains in the bar on the tension side of the column compared to slender counterparts. However, columns with *e/D* ratio of 0.17 experienced relatively low lateral displacements compared to those in columns with higher *e/D*

ratio, the measured tensile strain in the bars was very small. The strain in the tension side bar in specimen S28-60 and S14-60 was 480 and 550 με, respectively. However, for higher *e/D* ratios, the difference became larger, which was consistent with the increased lateral displacement and consequently the secondary moments in the slender columns. As more moment is exerted on the columns with *e/D* ratio 0.26 and 0.34, the deflected shape became more exaggerated.

In addition, the spiral strain was reduced as the slenderness ratio increased. Increasing the slenderness ratio from 14 to 28, reduced the spiral strain by 28.7, 20.5 and 16.4% in columns with *e/D* ratio of 0.17, 0.26 and 0.34, respectively. Again, this is due to the higher axial loads achieved by the short columns that in turn increased the confining pressure on the spiral.

The axial stiffness across the three *e/D* ratios was significantly impacted when λ increased from 14 to 28. For the same *e/D* ratios, columns with *e/D* ratio of 0.17, 0.26 and 0.34 experienced a reduction in axial stiffness by 38.0, 37.0 and 45.0%, respectively. Similarly, the lateral displacement of the columns was affected by the increased slenderness ratio. The lateral stiffness decreased by 20.0, 29.0 and 58.0% for columns with *e/D* ratio of 0.17, 0.26 and 0.34, respectively. Column S14-60 (*e/D* = 0.17) experienced a lateral displacement of 2.36 mm at peak load, whereas the counterpart slender column (S28-60) achieved 2.86 mm at only 50% of the peak capacity. Thereafter, column S28-60 reached a lateral displacement of 8.87 mm at peak load, which represents a 275.0% increase. Similarly, for *e/D* ratios of 0.26 and 0.34, the increase in lateral displacements due to doubling the slenderness ratio were 161.0 and 194.0%, respectively, at the peak load.

4.5.4 Flexural test

In this study, a specimen was tested under pure flexural loading in a four-point bending setup as shown in Fig. 4.2. The specimen showed initial cracks at a load of 32 kN. With the increasing load,

more cracks formed. When the load reached 80 kN, the cracks began to slightly widen. The load increased steadily until the concrete cover in the compression zone of the column spalled. The lateral stiffness of the column reduced because of the formed cracks. Nevertheless, the column continued to carry load until reaching a maximum load of 318 kN, at which the deflection was 71.3 mm. The peak load represented a moment carrying capacity of 150 kN.m. After the peak load, the specimen lost its capacity gradually with increasing deflection until the test was halted.

As shown in Fig. 4.9, the strain in the compression concrete before the initial spalling of the concrete cover was -3,750 με.

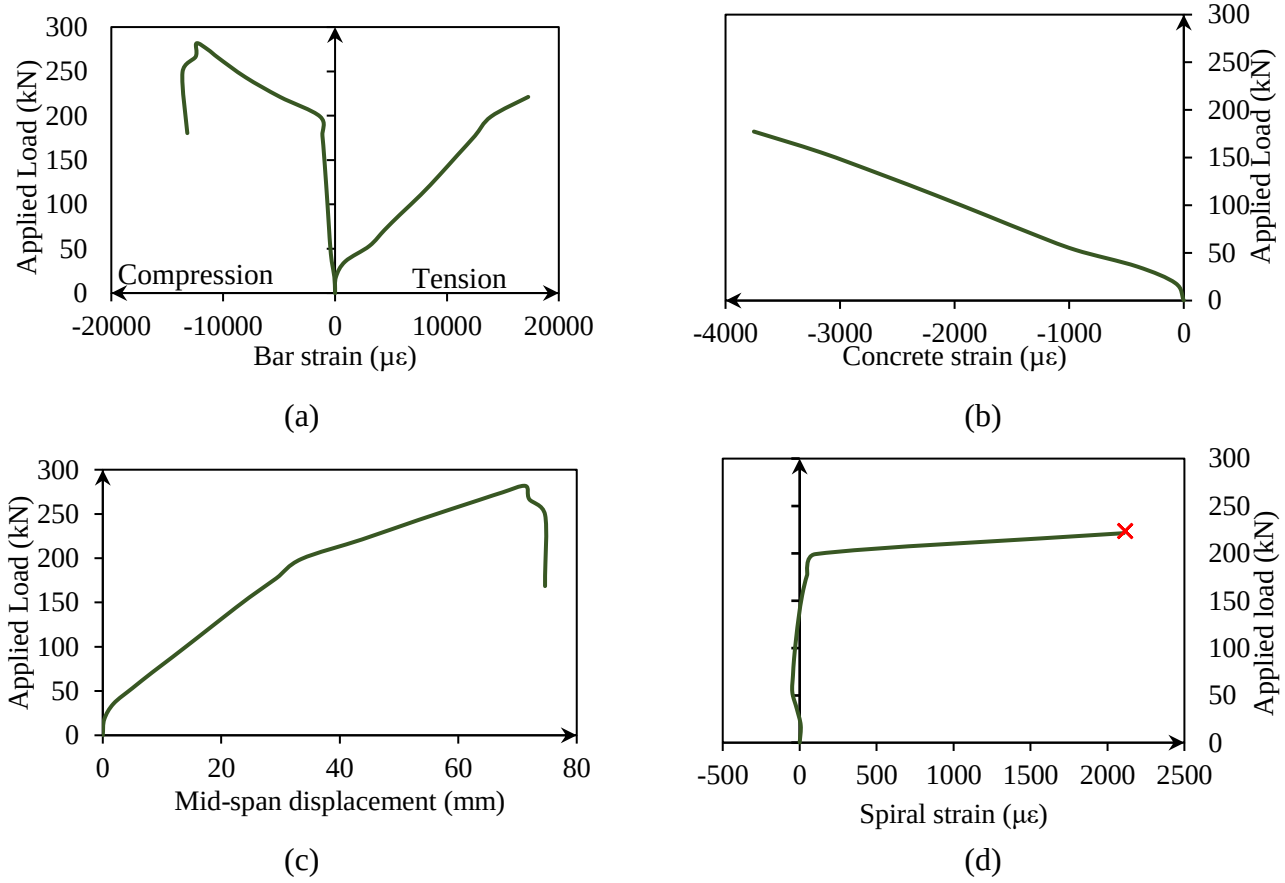

Figure 4.9 – Flexural specimen, (a) Extreme tension and compression bar strains, (b) Concrete strain, (c) Mid-span displacement, and (d) Spiral strain. (*Note:* 1 *kN* = 0.225 *kip;* 1 *mm* = 0.0394 *in.)*

After the concrete spalled, the concrete strain gauge malfunctioned. However, the strain in the GFRP bar in the compression side kept increasing to a strain of -12,390 με, while a tensile strain in excess of 15,000 με was measured on the tension side. The bars and spirals showed no sign of failure or rupture.

4.6 Experimental and Code Predicted Interaction Diagrams

The specimens in this study were designed to satisfy the provisions of the Canadian standards CSA S806-12 (CSA 2017). The columns were subjected to different loading eccentricities in addition to a specimen tested under pure flexural loading. Using the different loading conditions, an axial load-moment interaction diagram was developed. The capacities of the columns according to the Canadian CSA/S806-12 (CSA 2017) and American codes ACI 440.1R-15 (ACI 2015) were calculated using a strip analysis of the column section. This method consisted of dividing the column cross-section into small rectangular strips in order to integrate using a finite number of strips (Fig. 4.10a).

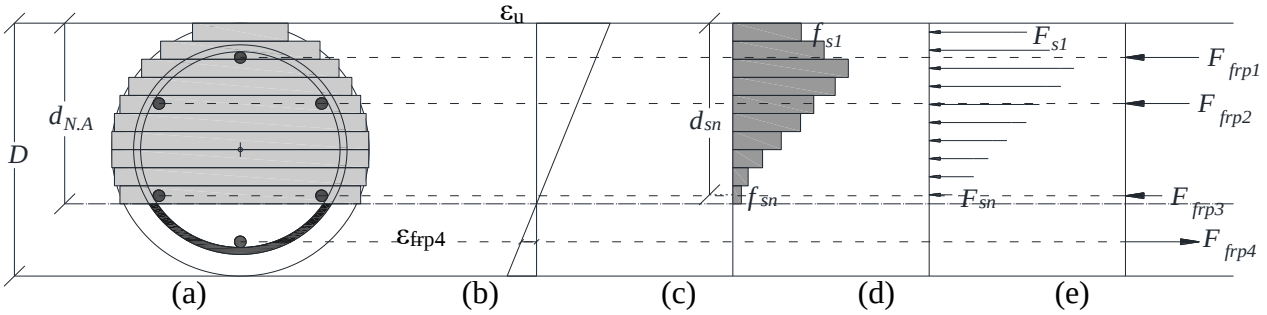

Figure 4.10 – Strip section analysis (a) Section strips, (b) Linear strain profile (c) Stress in concrete strips (d) Force in concrete strips (e) Forces in reinforcement layers

Thereafter, assuming a linear strain distribution the stress in each concrete strip was calculated. After calculating the width of the individual strips and using a predetermined thickness for the strips, the force in each strip and the corresponding force in the reinforcement can be determined then used to calculate the axial and moment capacity of the section. Due to the difference between NSC and HSC, the stress-strain relationship differs. Therefore, a model developed by Thorenfeldt et al. (1987) for unconfined HSC was used. This model was also employed in previous literature such as Hadi et al. (2017) to accurately determine the stresses in the HSC section. The analysis of the column section assumes that there is perfect bond between the concrete and reinforcement, the concrete in tension is neglected and the plane sections remain plane after bending. Therefore, the strain along the cross section and the strain in the reinforcement layers are proportional to the depth of the natural axis. To increase the accuracy of the integration, a 1-mm thickness of the strips was used. The stress in each concrete strip, f_{s_n} in Fig 4.10(c), is defined as:

$$f_{s_n} = \frac{f_c^{'} c^{xr}}{r - 1 + x^{kr}} \tag{4.1}$$

$$x = \frac{\varepsilon_c}{\varepsilon_o} \tag{4.2}$$

where ε_c is the corresponding strain to a concrete stress f_c and ε_0 is that corresponding to the maximum concrete stress f'_c. The remaining factors r and k are curve-fitting and slope control factors for the stress-strain curve, respectively, and can be defined as follows.

$$\varepsilon_o = \frac{f_c^{'}}{E_c}\left(\frac{r}{r-1}\right) \tag{4.3}$$

$$r = 0.8 + \left(\frac{f_c^{'}}{17}\right) \tag{4.4}$$

$$\text{for } \frac{\varepsilon_c}{\varepsilon_o} \leq 1.0 \text{ , } k = 1.0 \quad \text{and for } \frac{\varepsilon_c}{\varepsilon_o} > 1.0 \text{ , } k = 0.67 + \left(\frac{f_c'}{62}\right) \geq 1.0 \tag{4.5}$$

The modulus of elasticity, E_c, was calculated according to the respective code or guideline. This method was used to calculate the interaction diagrams predicted by both the ACI 440.1R-15 (ACI 2015), the CSA S6-19 (CSA 2019a) and the CSA S806-12 (CSA 2017). Differences in each code were considered such as the maximum concrete compressive strain (0.003 for the ACI guideline and 0.0035 for the CSA standards Additionally, since the CSA S806-12 (2017) and the ACI 440.1R-15 (2015) do not allow for the compressive capacity of the GFRP bars to be considered, their contribution has been excluded for the corresponding interaction diagram. On the other hand, the CSA/S6-19 (CSA 2019a) considers the contribution of the GFRP bars with a limited compressive strain in the bars of 0.002. Figure 4.11 shows the predicted interaction diagrams in addition to the experimental interaction diagrams plotted for each slenderness ratio. The interaction diagrams were normalised, where the y-axis represents the normalised axial load (K_n) and the x-axis represents the normalised bending moment (R_n):

$$K_n = \frac{P_n}{A_g f_c'} \tag{4.6}$$

$$R_n = \frac{M_n}{A_g f_c' D} \tag{4.7}$$

$$M_n = P_n(e + \delta) \tag{4.8}$$

where P_n is the peak load achieved by the column and δ is the maximum lateral displacement corresponding to the peak load. The nominal moment M_n is defined as the peak load multiplied by the applied eccentricity in addition to the maximum lateral displacement, A_g, f_c' and D are the gross area of the section, the concrete compressive strength, and the diameter of the column cross-section, respectively.

Both the slender and short column exhibited a “knee” shaped interaction diagram, which is similar to that of the code predictions in the range of the *e/D* ratios used in this study. In addition, the experimental K_n and R_n were higher than the code predictions for all *e/D* ratios despite neglecting any reductions in terms of slenderness effect in the predicted diagrams. The slenderness effect is represented by the disparity between the interaction diagrams for slender and short columns. On both accounts the predictions of different codes are conservative with the CSA S6-19 (CSA 2019a) giving the closest predictions.

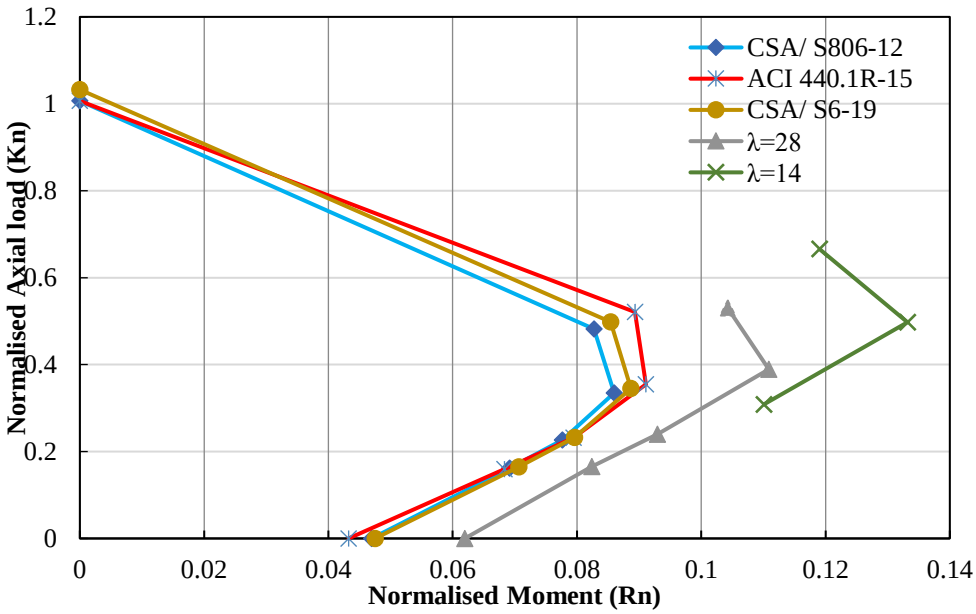

Figure 4.11 – Normalized load-moment interaction diagram

4.7 Conclusions

The following conclusions can be drawn based on the test results of the eight full-size HSC columns reinforced with GFRP discussed above:

1) The mode of failure in all specimens can be categorised as material type failures. The columns failed by spalling and crushing of the concrete on the compression side. With lower eccentricities, cracks on the tension side were observed near failure. However, as the

eccentricity increased, tension cracks formed at earlier stages due to the increased bending moment and excessive lateral deflections.

2) As the *e/D* ratio increased, the axial load capacity was greatly reduced. The axial capacity of the slender column decreased by 26.6, 54.7 and 68.5% when the *e/D* ratio increased to 0.26, 0.34 and 0.43, respectively, compared to the column with *e/D* = 0.17. Similarly, the capacity of the short column decreased by 29.8 and 53.7% when the *e/D* ratio increased from 0.17 to 0.26 and further to 0.34, respectively.

3) Based on the measured strains, the longitudinal bars have actively contributed to the axial capacity of the column. The strains in the GFRP bar on the compression side reached approximately the same values observed in the concrete. Furthermore, only the short column under *e/D* = 0.17 showed failure of the GFRP bar and spiral on the compression side.

4) As the slenderness ratio increased from 14 to 28, the axial capacity of the column decreased. For columns loaded at *e/D* ratio of 0.17, 0.26 and 0.34, the reduction in axial capacity was 20.4, 16.8 and 22.2% respectively. Although the primary moment capacity decreased in the slender columns, however, the secondary moment increased by 172, 118 and 146%.

5) The column under pure flexural loading reached a maximum load of 318 kN, which represents a moment of 150 kN.m. No signs of failure were observed in the GFRP bars or spirals. The GFRP bars were able to develop substantial compressive and tensile strains indicating active contribution to the specimen capacity.

6) The experimental data obtained from the tests were used to develop a normalised axial load-bending moment diagram. The diagram shows that the capacity of both the short and

slender columns exceeded the predictions of the Canadian standards (CSA 2017 and 2019a) and the American guidelines (ACI 2015) with the CSA S6-19 (CSA 2019a) giving the closest predictions.

5. EFFECT OF SLENDERNESS RATIO ON THE BEHAVIOR OF GFRP REINFORCED HIGH STRENGTH CONCRETE COLUMNS UNDER ECCENTRIC LOADING

Authors and Affiliation:

- Mu'taz Almomani, M.Sc. Student, Department of Civil Engineering, University of Manitoba.
- Karam Mahmoud, Post-Doctoral Fellow, Winnipeg, MB, Canada.
- Ehab F. El-Salakawy, Professor, Department of Civil Engineering, University of Manitoba.

Journal and Status: ASCE, Journal of Composites for Construction, under review.

Reference:

Almomani, M., Mahmoud, K., and El-Salakawy, E. "Effect of Slenderness Ratio on Large –Scale Eccentrically-Loaded GFRP-Reinforced HSC Columns." ASCE, Journal of Composites for Construction, Submitted in May 2021.

Note:

The manuscript had been slightly edited from the original paper by renumbering the tables and figures to include the chapter number. The abbreviations of the specimen names are explained in the list of abbreviations. In addition, the reference list and list of notations have been moved to the appropriate sections in the thesis as indicated in the table of contents.

5.1 Abstract

Ten large-scale high-strength concrete (HSC) circular columns were constructed and tested to failure. Nine columns were internally-reinforced with glass fiber-reinforced polymer (GFRP) bars and spirals, while one was reinforced with steel bars and spirals to serve as a reference. All columns had a diameter of 350 mm. The variables tested were reinforcement type, spiral pitch, slenderness ratio and eccentricity-to-diameter ratio (*e/D*). Experimental results showed that both reinforcement types (steel or GFRP) and the spiral pitch did not have a significant effect on the behavior of GFRP-reinforced HSC columns up to the peak load. In addition, a decrease in the axial capacity of the columns as the *e/D* ratio increased was observed. This was consistent for specimens of both slenderness ratios. Columns with a higher slenderness ratio showed a lower axial capacity for all specimens tested under the same *e/D* ratio. Furthermore, slender columns with higher *e/D* ratio underwent much larger deformations; both axially and laterally. For columns of both slenderness ratios, axial load-bending moment interaction diagrams were produced using the experimental results and were compared to the predictions of available codes and guidelines.

Keywords: Circular columns; slenderness ratio; eccentricity; GFRP bars and spirals; interaction diagram; pure bending.

5.2 Introduction

Design guidelines and codes in North America such as ACI 440.1R-15 (ACI 2015) CSA/ S806-12 (CSA 2017); CSA/ S6-19 (CSA 2019a), although allowing the use of FRPs, provided very conservative guidelines for the use of FRP in compression members such as columns due to lack of experimental data. The ACI 440.1R-15 (ACI 2015) and the CSA S806-12 (CSA 2017) neglected the contribution of FRP bars in compression, with the latter prohibiting the use of FRP entirely in slender compression members. Recently, the Canadian highway bridge design code, CSA/S6-19 (CSA 2019a), allowed the use of FRP reinforcing bars in compression up to a strain of 0.002.

The increased level of conservativeness regarding compression in FRP bars is due to the critical location and function of compressive members in a structure. Therefore, several recent studies have been directed at studying GFRP-reinforced concrete (RC) columns. The majority of these studies have investigated the behavior of normal strength concrete (NSC) columns reinforced with GFRP bars under eccentric loading (Hadhood 2017; Khorramian et al. 2017; Abdelazim 2020; Barua and El-Salakawy 2020; Elchalakani et al. 2020; Barua et al. 2021). These studies have found that GFRP bars are able to contribute effectively to the axial carrying capacity of columns. In addition, the provided transverse GFRP reinforcement was able to provide adequate confinement to the columns up to failure. The brittle nature and the different stress-strain relationship of high strength concrete (HSC) along with the very little studies conducted on HSC columns reinforced with GFRP bars makes the investigation of such columns necessary to outline the difference of its interaction with GFRP reinforcement. Few studies on the behavior of FRP-reinforced HSC columns reported that failure mode of such columns was material type failure characterized by concrete crushing, while FRP bars did not experience compression failure (Hales et al. 2016; Hadi et al. 2017; Abdelazim 2020). Furthermore, bars and spirals used in the specimens were able to

develop sufficient strains, while providing effective confinement of the concrete and contributing to the axial capacity of the columns. The confinement provided in specimens at higher eccentricities was more effective than that observed in steel-RC counterparts.

On the other hand, the codes remain overly conservative regarding the use of FRP materials in slender columns. This reflects the lack of a sufficient amount of experimental data concerning the issue. The slenderness ratio of a column ($\lambda = k\ell/r$), where k is the effective length coefficient, ℓ is the unbraced column length and r is the radius of gyration of column section, has always been an important topic due to the significant secondary moment that results from the lateral displacement associated with the axial load in such columns. However, combining the loss of axial capacity due to the slenderness effect and eccentric loading create a very critical case of loading. Slender columns undergo large deformations that cause a decrease in axial load. Although the mode of failure remains a material type failure, the slender columns showed more cracks due to the increased deflections (Abdelazim 2020). Research studies on NSC columns showed that increasing the slenderness ratio from 14 to 33 under the same *e/D* ratio, caused a 300% increase in the lateral displacement at the peak load. Moreover, other studies conducted on HSC slender columns reinforced with GFRP bars and spirals reported that columns with very high slenderness ratios (λ = 39.7 and 59.5) exhibited global buckling failure unlike specimens with lower ratios. Slender columns with moderate slenderness ratios (λ = 33) showed no signs of stability type failures (Khorramian et al. 2020; Abdelazim 2020). It is to be noted that these studies used reinforcement ratios ranging from 2.19 to 4.8%. However, Broms and Viest (1961) stated that columns with the minimum longitudinal reinforcement ratios are at a high risk of instability failure. As such, it becomes important to study the behavior of HSC columns with GFRP reinforcement that contain the minimum code requirements.

Mirmiran et al. (2001) investigated analytically the slenderness effect in columns reinforced with different types of FRPs and compared them to steel-RC specimens where all the columns had the minimum reinforcement ratio of 1%. The study suggested that the properties of FRP materials affected the slenderness of the column. These properties include the linear stress-strain behavior, the low compressive capacity and stiffness. Based on a parametric study taking into account many parameters, it was suggested to reduce the slenderness ratio limit of FRP-RC columns to 17 compared to the 22 used for steel-RC columns. This suggests that columns with a slenderness ratio between 17 and 22 that are usually considered short, are designed with a reduced level of conservativeness than that intended by the code. The study only considered NSC columns. Further investigation is required to verify the validity of such recommendation and their applicability to HSC columns. Furthermore, Barua et al. (2021) tested GFRP-reinforced NSC columns of slenderness ratio of 20 and 28. Results have shown that although by code definition the specimen of slenderness ratio of 20 is considered short, the columns behaved in a similar manner to that of slenderness ratio of 28.

5.3 Objectives

The literature highlights the critical impact of the slenderness effect on the behavior of GFRP-RC columns. With the differences in material properties in mind, further investigation into slender GFRP-reinforced HSC columns is necessary. Therefore, through the experimental investigation of such compression members, the objectives of this study are as follows:

1. Investigate the difference in the behavior of columns of slenderness ratio 14 that fall well into the short column classification and those with slenderness ratio of 20 that lies in the questionable range of 17-22.

2. Experimentally verify the applicability of slenderness ratio limits presented by current design codes and literature on GFRP-HSC columns.
3. Produce normalised axial load-bending moment interaction diagrams for the tested specimens and compare them to the predictions of design codes and guidelines.

5.4 Experimental Program

5.4.1 Materials

The columns were cast vertically using ready-mix concrete with a maximum nominal aggregate size of 20 mm and a target 28-day compressive strength of 60 MPa. The strength of the concrete for each column was obtained through testing standard 100×200 mm cylinders in accordance with CSA A23.1/2-19 (CSA 2019c). The strength of the concrete obtained on the day of testing for each column is listed in Table 5.1. Sand-coated GFRP bars and spirals as well as G400 steel bars and spirals were used to reinforce the columns. The mechanical properties of the GFRP reinforcement, provided by the manufacturer through a product certificate (Pultrall Inc. 2019), and those of the steel reinforcement are summarised in Table 5.2. The mechanical properties of the steel bars were obtained through standard tensile tests carried out in the laboratory according to CSA G30.18-09 (CSA 2019b).

5.4.2 Specimen details and construction

Ten large-scale HSC columns reinforced with either GFRP or steel bars and spirals were constructed and tested to failure. The columns were designed as per the CSA S806-12 (CSA 2017) and CSA A23.3-19 (CSA 2019d) where appropriate. The columns had a diameter of 350 mm and a length of either 1,250 or 1,750 mm representing slenderness ratios of 14 or 20, respectively.

Table 5.1 – Test matrix

Specimen ID	λ	Longitudinal Reinforcement ρ_f, (%) [Config.]	Transverse Reinforcement ρ_{fs}, (%) [Pitch (mm)]	e (mm) [e/D]	f'_c (MPa)
S85-20-E60	20	1.21 [6-15M]	1.43 [85]	60 [0.17]	58.2
G50-20-E60	20	1.21 [6-No.15]	1.89 [50]	60 [0.17]	59.4
G85-20-E60	20	1.21 [6-No.15]	1.11 [85]	60 [0.17]	60.3
G85-20-E90	20	1.21 [6-No.15]	1.11 [85]	90 [0.26]	57.0
G85-20-E120	20	1.21 [6-No.15]	1.11 [85]	120 [0.34]	65.0
G85-20-E150	20	1.21 [6-No.15]	1.11 [85]	150 [0.43]	58.0
G85-20-FL	20	1.21 [6-No.15]	1.11 [85]	∞ [∞]	65.0
G85-14-E60	14	1.21 [6-No.15]	1.11 [85]	60 [0.17]	57.1
G85-14-E90	14	1.21 [6-No.15]	1.11 [85]	90 [0.26]	64.3
G85-14-E120	14	1.21 [6-No.15]	1.11 [85]	120 [0.34]	56.0

Table 5.2 –Properties of steel and GFRP reinforcement

Type	Bar Size	Nominal diameter (mm)	Area (mm^2)		Modulus of elasticity (GPa)	Tensile strength (MPa)	Ultimate strain (%)
			Nominal	Annex A*			
Steel	15M	16.0	200	N/A	200	460[1]	0.23[2]
Steel	10M (Spiral)	11.3	100	N/A	200	420[1]	0.21[2]
GFRP	No.15	15.9	199	235	64±1.5	1,558±47	2.40
GFRP	No.10 (Spiral)	9.5	71	83	58±1.5	667±41	1.14

*Annex A of the CSA S806-12 (CSA 2017)
[1]Yield strength of steel bars and spirals
[2]Yield strain of steel bars and spirals
Note: the nominal area was used in the calculation of the mechanical properties of GFRP.

The effective length factor *k* was set to unity as the columns were tested under pin-pin boundary conditions. The longitudinal reinforcement ratio of the specimens was selected to be as close as possible to the minimum allowed by the code (1.21%) considering other requirements such as the size (15M) and number of bars (6 bars). Size 10M spirals with the maximum allowed (clear) pitch of 75 mm were used in nine columns, while a pitch of 50 mm was used for one column for comparison purposes (Fig. 5.1). The test matrix is shown in Table 5.1.

The specimen nomenclature consists of four parts reflecting the tested parameters. The first part is a letter indicating the reinforcement type used (S for steel or G for GFRP). The second is a numerical value (50 or 85) indicating the spiral pitch. The third is also a numerical value representing the slenderness ratio of the column of either 14 or 20. The fourth and final part refers to the loading condition where E60, E90, E120 and E150 represents an axial load eccentricity of 60, 90, 120 and 150, respectively while FL refers to a specimen tested under four-point bending (pure flexure).

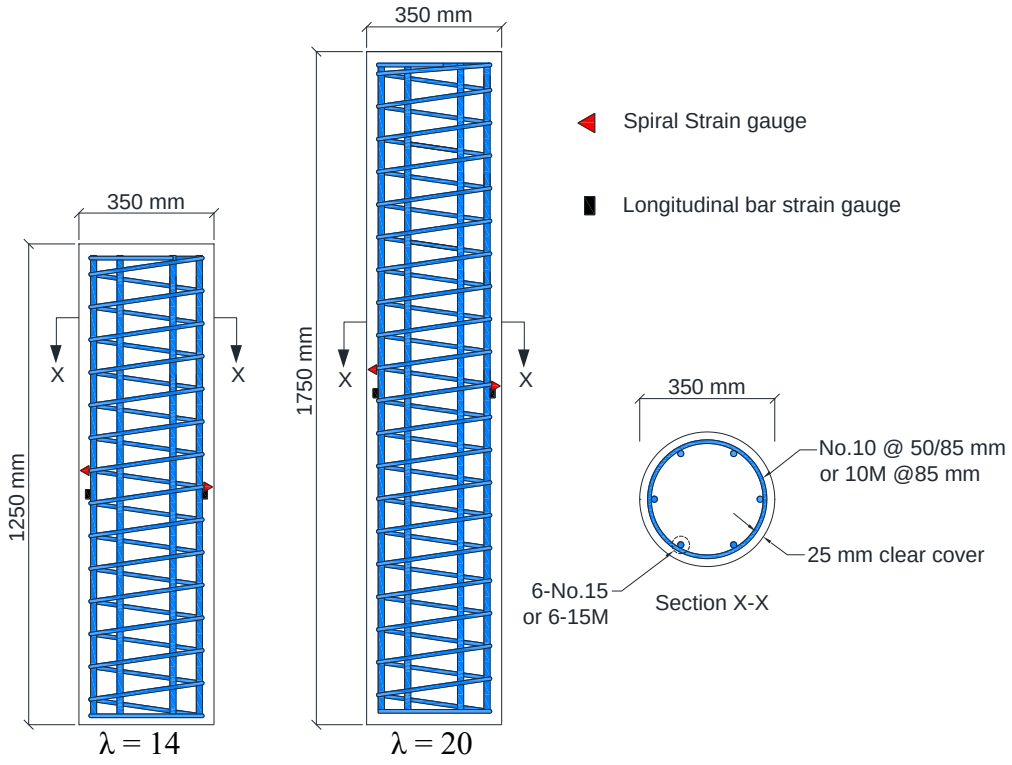

Figure 5.1 – Specimens details, reinforcement configuration and internal instrumentation

5.4.3 Test setup and procedure

The test was conducted using a 5000-kN hydraulic machine. The axially-loaded columns were placed in heavy steel collars and aligned in the machine to ensure loading at the specified eccentricity. The eccentric loading was facilitated by welding of the pin on each collar at the

required distance from the specimen centroid ensuring the intended load transfer and pin-pin boundary condition. The monotonic load was applied at a constant rate of 1.5 mm/min and the specimens were loaded until failure. After the column reached the peak load, the loading continued until the specimen lost 25% of its axial capacity. The four-point bending test was carried out using four semi-circle steel saddles with radius similar to that of the columns. The load was applied to the upper saddles using a spreader beam. The test setups are depicted in Fig. 5.2.

5.4.4 Instrumentation

The specimens were fitted with multiple strain gauges to measure strains in the longitudinal bars, spirals and concrete. Additionally, a PI-gauge was installed on the compression side of the column to measure strains in the concrete. All gauges were placed at the mid-height of the column, where the maximum strains were expected. Furthermore, the lateral and axial displacements of the columns were monitored using linear variable displacement transducers (LVDTs). The lateral displacement of the column was measured using five LVDTs distributed along the height of the column and the axial displacement by vertical LVDTs attached to the sides of the columns at mid-height. The internal and external instrumentation are shown in Figs. 5.1 and 5.2.

5.5 Experimental Results and Discussion

5.5.1 General behaviour and modes of failure

The failure of all specimens was a material-type failure characterised by the crushing of the concrete. Out of all tested columns, the short specimen G85-14-E60 was the only specimen to experience crushing of the compression GFRP bar and the rupture of the confining spiral at mid-height of the column (Fig. 5.3). The specimens tested under the lowest eccentricities showed no tension cracks prior to failure. The formation of the tension cracks and crushing of the concrete occurred simultaneously near the peak load.

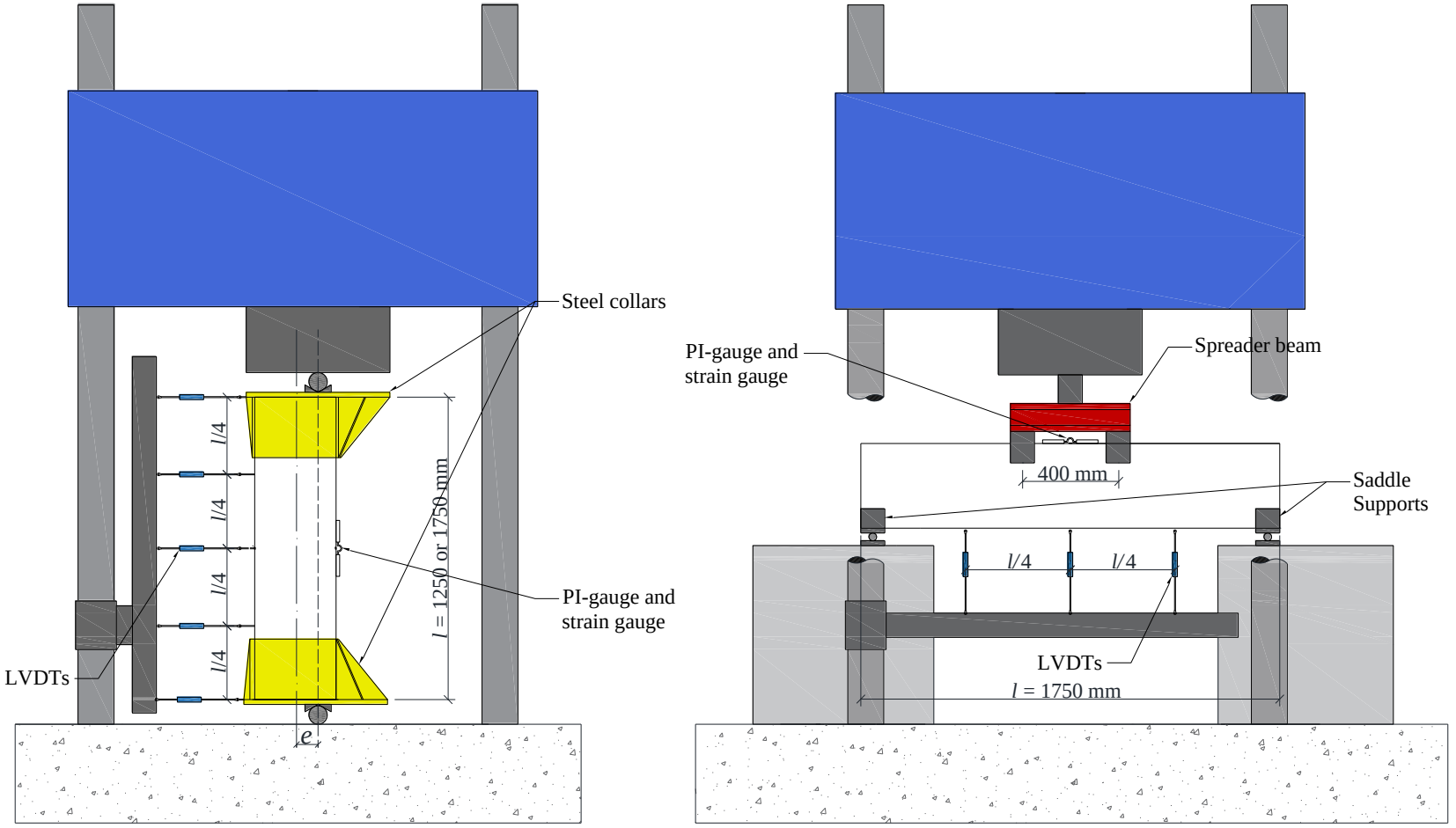

(a) (b)

Figure 5.2 – Test setup and external instrumentation, (a) Axial load, and (b) Flexural load.

For columns with higher eccentricity, the crushing of the concrete was preceded by a gradual increase in cracks on the tension side until failure. The first cracks were observed at 20.4 and 16.3% of the peak load in specimens G85-14-E90 and G85-14-E120 and at 18.1, 16.5 and 15.3% of the peak load in specimens G85-20-E90, G85-20-E120 and G85-20-E150, respectively. For specimen G85-20-FL the first flexural cracks were observed at 12.2% (55 kN) of the peak load. As the load increase, the cracks started to propagate diagonally between the support and the loading point. This was followed by widening and extending of the cracks until concrete crushing at the mid-span was observed. Due to variability in the concrete strengths of the columns on the day of testing (Table 5.1), the peak loads were normalised using a factor of $60/f_c'$, where 60 is the average concrete strength and f_c' is the concrete strength of each individual column. The experimental results are summarised in Tables 5.3 and 5.4.

Table 5.3: Experimental displacements, peak loads and bending moments.

Specimen ID	λ	e/D	δ (mm)	Δ (mm)	P_u (kN)	P_u^* (kN)	M_1^* (kN.m) [$P_u^* \times e$]	M_2^* (kN.m) [$P_u^* \times \delta$]	M_{total}^* (kN.m) [M_1+M_2]
S85-20-E60	20	0.17	6.2	10.6	3,708	3,825	229.5	23.7	253.2
G50-20-E60	20	0.17	6.0	10.2	3,560	3,598	212.9	21.3	234.2
G85-20-E60	20	0.17	5.8	9.7	3,541	3,525	211.5	20.4	231.9
G85-20-E90	20	0.26	6.4	9.0	2,383	2,510	225.9	16.0	241.9
G85-20-E120	20	0.34	8.7	9.4	1,771	1,636	196.3	14.2	210.5
G85-20-E150	20	0.43	10.1	7.2	1133	1,173	176.0	11.8	187.8
G85-20-FL	20	-	38.3	-	-	-	-	-	134.0
G85-14-E60	14	0.17	2.4	8.9	3,657	3,845	230.7	9.1	239.8
G85-14-E90	14	0.26	3.8	8.1	3,076	2,871	258.4	10.8	269.2
G85-14-E120	14	0.34	5.3	7.4	1,662	1,782	213.8	9.4	223.2

*Normalized with factor $60/f'_c$, where 60 MPa is the average concrete strength.
Note: Δ and δ is the axial and lateral displacement at peak load, respectively.

S85-20-E60

G50-20-E60

G85-20-E60

G85-20-E90

G85-20-E120

G85-20-E150

G85-14-E60

G85-14-E90

G85-14-E120

Figure 5.3 – Mode of failure for axially-loaded columns

Table 5.4: Measured strains in vertical bars, concrete, and spirals for all columns

Specimen ID	λ	Tensile strain in GFRP bars ($\mu\varepsilon$)		Compressive strain in GFRP bars ($\mu\varepsilon$)		Concrete strain ($\mu\varepsilon$)	Spiral Strain ($\mu\varepsilon$)	
		At peak load	Max.[1]	At peak load	Max.[1]		At peak load	Max.[1]
S85-20-E60	20	370	2,760	-2,430	-4,360	-3,530	1,230	-
G50-20-E60	20	700	7,980	-3,130	-11,270	-3,640	1,270	7,620
G85-20-E60	20	610	3,560	-2,930	-6,280	-3,640	1,320	2,670
G85-20-E90	20	1,560	5,080	-2,690	-5,930	-2,370	920	3,230
G85-20-E120	20	3,570	5,450	-1,790	-2,270	-2,590	840	1,610
G85-20-E150	20	5,510	11,730	-2,590	-10,080	-3,110	600	4,610
G85-20-FL	20	15,270[2]	24,290[3]	-1,360[2]	-13,790[3]	-3,910[2]	210[2]	3,750[3]
G85-14-E60	14	545	5,090	-3,050	-8,240	-2,890	2,050	8,530
G85-14-E90	14	1,380	6,100	-2,880	-5,220	-3,120	1,020	4,560
G85-14-E120	14	3,130	6,620	-2,860	-6,440	-3,430	880	2,120

[1]Maximum strains obtained at the end of the test after 25% load loss
[2]Values measured at crushing of concrete cover
[3]Values measured at final failure (crushing of concrete core) or malfunction of the strain gauge

5.5.2 Effect of reinforcement type

The steel-RC column (S85-20-E60) achieved a peak axial load of 3,825 kN, whereas it counterpart with GFRP reinforcement (G85-20-E60) achieved 3,525 kN representing a decrease of 7.8% in axial capacity. The axial displacement of both columns exhibited a linear increase until peak load. After peak load, column G85-20-E60 showed a sharp decrease in load with little change in the displacement. However, specimen S85-20-E60 continued to undergo vertical displacement as the load drops (Fig. 5.4).

The axial displacement at the peak load was 10.6 and 9.7 mm in columns S85-20-E60 and G85-20-E60, respectively. Similarly, a linear increase in the lateral displacement as the load increased was observed with a displacement of 6.2 and 5.8 mm at the peak load for specimens S85-20-E60 and G85-20-E60, respectively. After reaching the peak load, the columns exhibited increasing lateral displacement while losing their axial load carrying capacity (Fig. 5.5). The columns reached a maximum lateral displacement of 15.5 and 10.5 mm when the test was halted after a loss of 25%

of the respective peak loads for the steel- and GFRP-RC specimens. This shows that the behavior of the HSC columns reinforced with GFRP and steel behaved in a very similar manner.

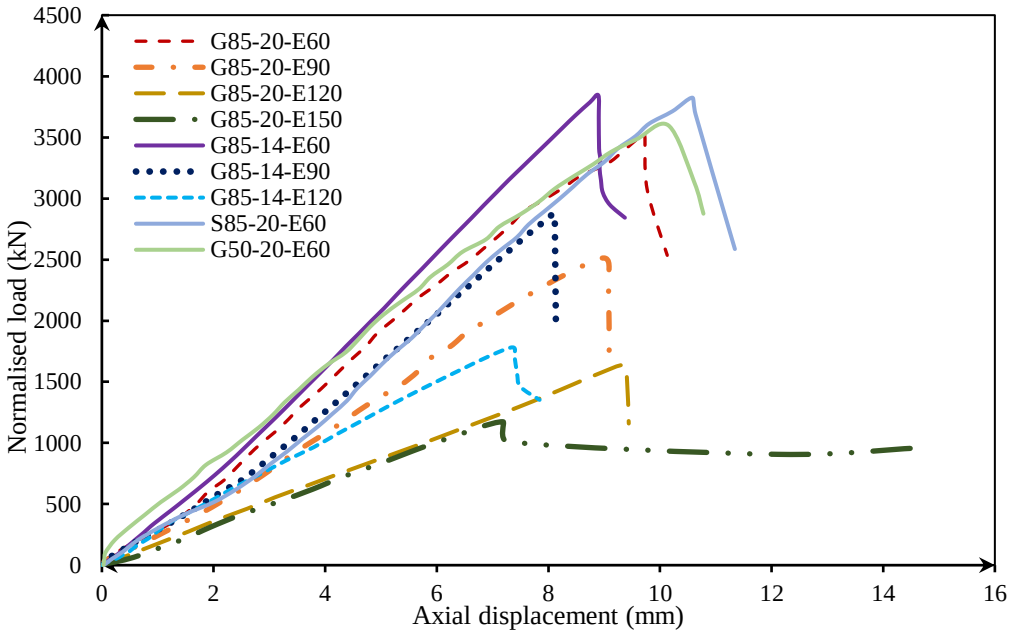

Figure 5.4 – Load versus axial displacement of axially loaded columns

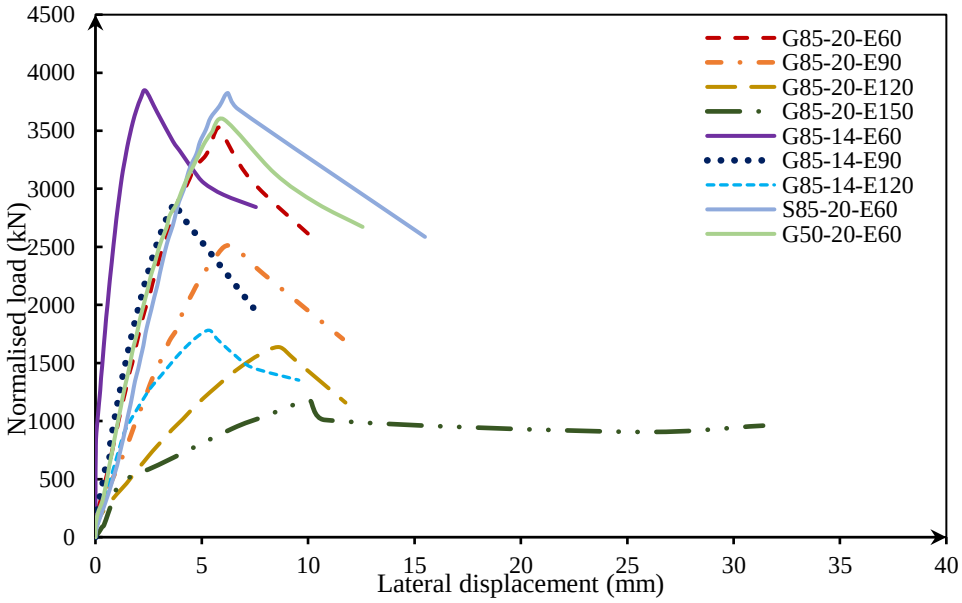

Figure 5.5 – Load versus lateral displacement of axially loaded columns

This is further evidenced by the recorded strains in the outermost bars and the concrete (Fig. 5.6). The strains in the bars for both columns increased linearly until the peak load and then began to

exponentially increase as the column capacity decreases. The bar strains on the compression side recorded at peak load were -2,430 and -2,930 με whereas the bar strains on the tension side were 370 and 610 με for specimens S85-20-E60 and G85-20-E60, respectively. This indicated that the steel bars in compression have started to yield slightly before the peak load. In the post-peak stage, bars on the tension and the compression sides experienced large strains in both steel- and GFRP-RC columns. The maximum recorded concrete strains were -3,530 and -3,640 με in column S85-20-E60 and G85-20-E60, respectively, which exceeded the design concrete strains of 3,000 and 3,500 in the ACI 440.1R guideline (ACI 2015) and the Canadian standards (CSA 2017; CSA 2019a and d), respectively.

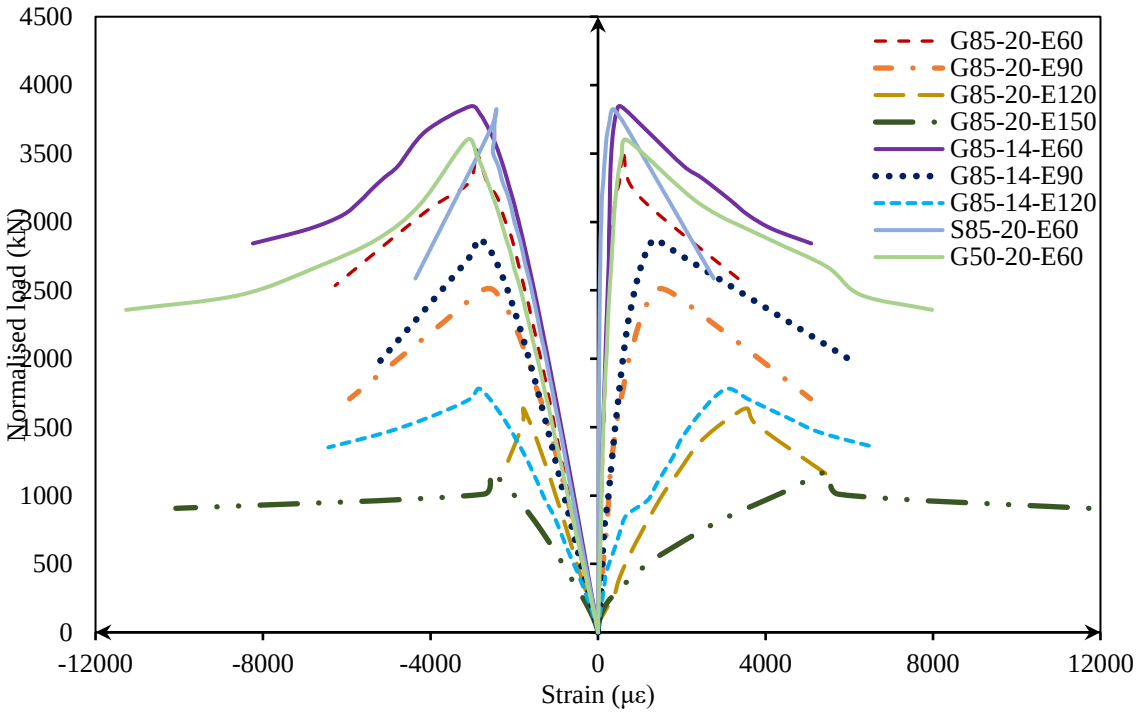

Figure 5.6 – Load-strain relationship for axially loaded columns

The spiral strains (Fig. 5.7) were almost identical up to 40-50% of the peak load; however, the GFRP-RC column exhibited more strains as it approached the peak load. The steel- and GFRP-

RC columns achieved spiral strains of 1,230 and 1,320 με at the peak load, respectively. The GFRP spiral reached a maximum strain of 2,670 με after a load loss of 25% while the strain gauge attached to the steel spiral malfunctioned before the test was halted with strain reading of 1,780 με. Throughout the tests of both specimens, the most significant difference was the 7.8% decrease in peak axial capacity of the GFRP-RC column compared to the steel-RC specimen, which can be attributed to the lower compressive capacity of the GFRP reinforcement. However, the measured displacements and strains showed the ability of HSC column reinforced with GFRP bars to exhibit similar behavior under eccentric loading compared to their steel-RC counterparts.

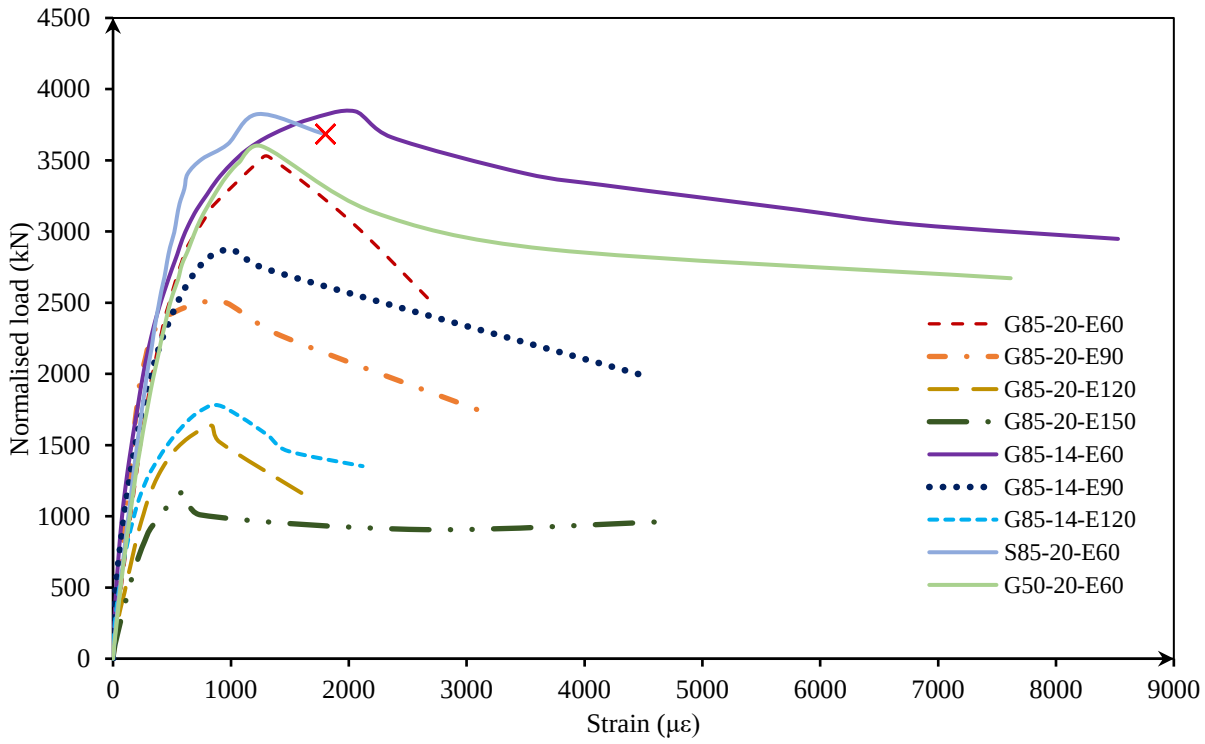

Figure 5.7 – Load-spiral strain relationship for axially loaded columns

A similar comparison was made by Barua and El-Salakawy (2020) for specimens of identical reinforcement and dimensions; however, with normal strength concrete (average concrete strength of 38 MPa). The specimens were tested under a 30 mm eccentricity (e/D = 0.085). GFRP-RC

column exhibited a decrease of 16.6% in the axial capacity compared to the steel-RC counterpart. Similarly, a study by Abdelazim (2020) compared steel- and GFRP-RC specimens with average concrete strength of 46.6 MPa. The specimens tested under concentric load showed a decrease in axial load by 11%, whereas those under *e/D* ratio of 0.66 showed a decrease of 23%.

5.5.3 Effect of spiral pitch

Decreasing the pitch from 85 to 50 mm caused no significant change in the axial capacity, increasing by only 2.1%. The normalized capacities achieved were 3,525 and 3,598 kN for specimens G85-20-E60 and G50-20-E60, respectively. The spiral strains were very similar up to approximately 85-88% of the axial capacity after which, the specimen with 85-mm pitch started to gain larger spiral strain. Both specimens showed adequate confinement and increasing the spiral reinforcement ratio had no significant effect on the peak axial capacity. The results of Hadi et al. (2017) also showed very little difference in column capacity since a 1.7% decrease was observed for 210-mm diameter HSC columns when the spiral pitch decreased from 60 to 30 mm tested at an $e/D = 0.12$. As shown in Fig. 5.4, both axial and lateral displacements as well as strains in the GFRP bars, concrete and spirals for both specimens are identical before the peak load. This shows that prior to the crushing of the concrete, the spirals in both columns did not provide significantly different confinement to the concrete core. At peak load, specimens G50-20-E60 and G85-20-E60 exhibited an axial displacement of 10.2 and 9.7 mm, respectively. After the peak load, both specimens showed a sharp drop in axial capacity with little increase in the axial displacement. The lateral displacements at peak load of columns G50-20-E60 and G85-20-E60 were 6.0 and 5.8 mm, respectively. Likewise, the maximum strain in the outermost bars measured at peak load was 700 and 610 με on the tension side and -3,130 and -2,930 με on compression side in columns G50-20-E60 and G85-20-E60, respectively. Moreover, in the post-peak stage, reducing the spiral pitch

from 85 to 50 mm reduced the rate of loss of axial load capacity of the columns. This is a direct consequence of the activation of the spiral confinement only following the crushing of the concrete cover. Once the concrete cover spalled, the spirals were able to develop sufficient strains allowing them to confine the concrete core. As shown in Fig. 5.7, confinement provided by a spiral pitch of 50 mm was superior to that of 85 mm as evidenced by the measured spiral strains in the post-peak stage. The specimen with 50 mm spiral pitch began effectively confining the concrete core after the specimen lost 12.9% of its axial capacity. The spirals were then able to slow down the degradation of the columns capacity and gained a maximum spiral strain of 7,620 με at 25% load loss of peak axial capacity. However, specimen G85-20-E60 only achieved a maximum spiral strain of 2,670 με.

The same spiral pitches were tested by Barua and El-Salakawy (2020) for NSC columns and showed a 9% decrease in axial capacity when increasing the pitch from 50 to 85 mm. The results also showed that the axial stiffness of the column with 50 mm pitch was higher than that of the 85 mm pitch. This indicated that, in normal strength concrete columns, the spiral confinement contributed to the pre- and post-peak behavior. This was further verified by the spiral strain profiles for those columns, where the column with 50-mm pitch started to develop larger spiral strains in earlier loading stages and thus provide additional confinement. In contrast, the HSC columns in this study showed identical spiral strain profiles in the pre-peak stage and thus indicating that the concrete did not undergo sufficient dilation to allow for activation of the spirals.

5.5.4 Effect of slenderness ratio

As per the CSA S806-12 (CSA 2017) definition, both slenderness ratios 14 and 20 are considered short columns. However, recommendations from the literature classify columns with $\lambda = 20$ as slender for GFRP-RC columns caused by several factors such as lower stiffness, linear-elastic

response of FRP, higher tensile strength and lower compressive strength (Mirmiran et al. 2001; Abdelazim 2020). Increasing λ from 14 to 20 resulted in a decrease in the axial load capacity by 8.3, 12.6 and 8.2% for columns with *e/D* ratio of 0.17, 0.26 and 0.34, respectively. On the other hand, for the same *e/D* ratios, the secondary moment, caused by the lateral displacement of the column, increased by 124.2, 48.1 and 51.1%. The increase in the secondary moment offsets much of the decrease in primary moment, resulting in a 3.3, 10.1 and 5.7% decrease in the total moment for the mentioned *e/D* ratios, respectively. The loads, moments and displacements at peak load for all columns are summarized in Table 5.3. Furthermore, as the load increased, the axial displacement increased linearly until failure for all specimens (Fig. 5.4). The change in λ caused an increase in axial displacement at peak load by 9.0, 11.1 and 27.0% for columns with *e/D* ratios of 0.17, 0.26 and 0.34, respectively. Following the peak load, a sharp drop in the axial load was observed for most specimens with little to no change in axial displacement. Moreover, the effect of λ on the lateral displacement is much greater than the axial displacement. The lateral displacement increased linearly until the peak load; however, showing larger displacements in the post-peak stage (Fig. 5.5). This behavior is consistent for all columns. For columns with λ = 14, the lateral displacements at the peak load were 2.4, 3.8 and 5.3 mm for *e/D* ratio of 0.17, 0.26 and 0.34, respectively. In comparison, columns with a slenderness ratio of 20 achieved displacements of 5.8, 6.4 and 8.7 mm for the same *e/D* ratios. This represents an increase in the lateral displacement at peak load of 141.7, 68.4 and 62.9% in columns with *e/D* ratio of 0.17, 0.26 and 0.34, respectively. With the increase in λ, the lateral and axial stiffness (the gradient of the ascending portion of the load-lateral displacement and load-axial displacement graphs, respectively) decreased. For the same *e/D* ratio (0.17, 0.26 and 0.34), increasing λ from 14 to 20 resulted in the decrease of the axial stiffness by 12.3, 19.7 and 26.6%, whereas the reduction in the

lateral stiffness was 55.9, 43.4 and 25.1%, respectively. After reaching the peak, the load declined and columns G85-14-E60, G85-14-E90 and G85-14-E120 reached a maximum lateral displacement of 7.5, 7.4 and 9.6 mm, respectively, whereas columns G85-20-E60, G85-20-E90 and G85-20-E120 reached 10.5, 11.6 and 11.8 mm, respectively, at an axial load loss of 25% of the peak load capacity.

Figure 6 presents the relationship between the axial load and the strains in vertical reinforcement on the compression and tension sides. In general, the strains increased linearly until failure. After the peak load, the bars started to develop strain more rapidly with declining axial load. At the peak load, in columns with $\lambda = 14$, the bar strains on the compression side were -3,050, -2,880 and -2,860 με, whereas in columns with $\lambda = 20$, these strains were -2,830, -2,690 and -1,790 με for *e/D* ratios of 0.17, 0.26 and 0.34, respectively. The decrease in compressive bar strain with increasing λ represents 7.4, 6.6 and 37.3%, respectively. For the same *e/D* ratios, the tensile strains at the peak load were 550, 1,380 and 3,130 με for columns with $\lambda = 14$ and were 610, 1,560 and 3,570 με for columns with $\lambda = 14$. The spiral strains (Fig. 5.7) showed very similar behavior across slenderness ratios. The spiral strains increased at a slower rate in the pre-peak than the post-peak stage. After reaching the peak load and the spalling of concrete cover started, the spirals began to gain strain at a much greater rate, reaching strains up to a maximum of 8,530 με. This was due to that the crushing of the concrete cover drastically increased the compression on the concrete core and thus activating the spiral reinforcement. As the λ increased from 14 to 20, the spiral strains at peak load decreased by 35.6, 9.8 and 4.5% while this decrease at 25% loss of the axial load was 68.7, 29.2 and 24.0% (Fig. 5.7). Barua et al. (2021) provided evidence supporting the recommendations regarding the slenderness limit reduction proposed by Mirmiran et al. (2001). The study found that changing the slenderness ratio of steel-RC columns and GFRP-RC columns

across the limit of 22 set by the code yielded different results. The steel specimens showed a shift from short to slender behavior, whereas the GFRP specimens did not seem to undergo any behavioral change. Rather both slenderness ratios of 20 and 28 were in the slender behavior category. For HSC columns with slenderness ratios of 14 and 20, the results showed that there is a transition of behavior due to the changed slenderness ratios and thus supports further the recommendations of reducing the slenderness limit of GFRP-RC columns put forth.

5.5.5 Effect of eccentricity

As expected, when the eccentricity was increased the axial load capacity decreased. Increasing the *e/D* ratio from 0.17 to 0.26 and further to 0.34 resulted in a decrease in axial load by 25.3 and 53.7%, respectively for columns with $\lambda = 14$. Similarly, increasing the *e/D* ratio from 0.17 to 0.26 and further to 0.34 and 0.43 caused a decrease in the axial capacity by 28.8, 53.6 and 66.7%, respectively, in columns with $\lambda = 20$. However, the columns showed an increase in the total moment capacity when increasing *e/D* from 0.17 to 0.26 by 12.3 and 4.3% for specimens with $\lambda =$ 14 and 20, respectively. Further increase in the *e/D* ratio to 0.34 for the column with $\lambda = 14$, caused a decrease in moment capacity by 6.9% with respect to specimen G85-14-E60. Increasing the *e/D* ratio from 0.17 to 0.34 and further to 0.43 for specimens with $\lambda = 20$ led to a decrease in moment capacity by 9.2 and 19.0%, respectively. This decreasing pattern, preceded by an initial rise in moment capacity, is due to the scatter of the specimens around the theoretical balance point of the axial load-bending moment interaction diagram.

The peak axial displacement of the specimens for both slenderness ratios were very similar in value. The axial displacements in columns G85-14-E60, G85-14-E90 and G85-14-E120 were 8.9, 8.1 and 7.4 mm, respectively. For columns with $\lambda = 20$, the axial displacement in columns with *e/D* ratio of 0.17, 0.26, 0.34 and 0.43 were 9.7, 9.0, 9.4 and 7.2 mm, respectively. However, the

lateral displacement of the specimens showed a distinct increase with increasing *e/D* ratio. The lateral displacement at peak load was 2.4, 3.8 and 5.5 mm for columns G85-14-E60, G85-14-E90 and G85-14-E120, respectively, representing an increase of 58.9 and 126.3%, compared to that of G85-14-E60. Columns with $\lambda = 20$ showed a similar increasing pattern, however, at larger displacements that measured 5.8, 6.4, 8.7 and 10.1 mm for *e/D* ratios of 0.17, 0.26, 0.34 and 0.43, respectively. This represents an increase of 10.3, 50.0 and 74.1%, respectively. Additionally, increasing the *e/D* ratio resulted in a reduction in the axial and lateral stiffness for columns of both slenderness ratios. For the short columns, the lateral stiffness decreased by 47.0 and 82.2% when increasing the *e/D* ratio from 0.17 to 0.26 and further to 0.34. Likewise, increasing the *e/D* ratio for columns with $\lambda = 20$ from 0.17 to 0.26 and further to 0.34 and 0.43, resulted in a decrease of 32.0, 69.8 and 86.9%, respectively. The axial stiffness for columns with $\lambda = 14$ decreased by 16.4 and 47.0%, while that for specimens with $\lambda = 20$ decreased by 23.5, 55.6 and 59.0% for the aforementioned *e/D* ratios, respectively.

The strains developed in the specimens indicated a material-type failure. The maximum concrete strains developed in the compression side of the columns were close to or exceeded the design strain of 3,500 με in the Canadian codes (CSA 2017 and 2019a) and the 3,000 με in the American guideline (ACI 2015). The strains in the bar on the compression side for all specimens were approaching the concrete strains in the extreme concrete fibers, which provides evidence of the compressive load carrying capacity of GFRP reinforcement (Table 5.4). The tension strains developed in the extreme tension layer of reinforcement in the columns showed an increase in the strains as the *e/D* ratio increased. This can be attributed to the increased moment and lateral displacements developed as the *e/D* ratio increased. The tensile strains developed in the short specimens were 550, 1,380 and 3,130 με for *e/D* ratios 0.17, 0.26 and 0.34, respectively, which

represents an increase of 154 and 474% when compared to the strain in column G85-14-E60. Similarly, in columns with λ = 20, the strains for the same *e/D* ratios were 610, 1,560 and 3,570 με, respectively, representing an increase of 156.0, 485.0%, respectively. Increasing the *e/D* ratio further from 0.17 to 0.43 resulted in an additional 803.0% increase in tensile strain. The spiral strains were generally higher for lower *e/D* ratios. For the columns with λ = 14, the spiral strain was 2,050 με when the *e/D* ratio was 0.17. As the *e/D* ratio increased to 0.26 and 0.34, the spiral strain reduced to 1,020 and 880 με, respectively. This is a reduction of 50.0 and 57.4% compared to the specimen with low *e/D* ratio (0.17). Increasing the *e/D* ratio for columns with λ = 20 yielded similar results. Specimens with *e/D* ratio of 0.26, 0.34 and 0.43 experienced spiral strains of 1,320, 920, 840 and 600 με, respectively. When compared to *e/D* ratio 0.17, this represents a reduction in spiral strains by 30.4, 36.5 and 54.9%, respectively. The higher the eccentricity, the smaller the overall compression zone and therefore, there is less of the concrete core experiencing compression as the *e/D* increased, which in turn reduced the tension strains in the spirals.

5.5.6 Effect of concrete strength

Specimens with λ = 20 and NSC were tested by Barua and El-Salakawy (2020) with identical dimensions and reinforcement as those in this study. Increasing the concrete strength from 38 to 60 MPa resulted in an increase in axial capacity of 36.0 and 28.0% for specimens with an *e/D* ratio of 0.17 and 0.26, respectively. However, for the same *e/D* ratios, increasing the concrete strength caused a moment capacity decrease of 36.0 and 25.0%. At peak load, the measured lateral displacements for the NSC columns were 5.3 and 9.2 mm, whereas at the same load level, the HSC columns achieved displacements of 3.4 and 5.7 mm for *e/D* ratios 0.17 and 0.26, respectively. This indicates a much higher lateral stiffness of the HSC specimens. The axial displacement measured at the peak load for the NSC columns were 8.4 and 7.8 mm compared to 6.8 and 7.5 mm for the

HSC specimens at the same load level for the same *e/D* ratio. However, the HSC columns had an axial stiffness that is approximately 17% higher. The increase in the concrete strength caused a decrease in tensile and compressive strains in the GFRP bars at the same load level. At peak load, the NSC columns achieved tensile bar strains of 650 and 4,760 με for *e/D* ratios 0.17 and 0.26, respectively, while for the same load level, the HSC experienced a 64 and 54% reduction in tensile strains. Furthermore, the compressive strains at the aforementioned load level decreased by 51 and 58%, respectively.

5.5.7 Flexural loading

Figure 5.8 shows the mode of failure for specimen G85-20-FL tested under pure flexure, which is characterized by crushing of the concrete cover followed by crushing of the concrete core. In addition, Fig. 5.9 shows the experimental results for specimen G85-20-FL. Before cracking, the specimen gained load with very little deflection.

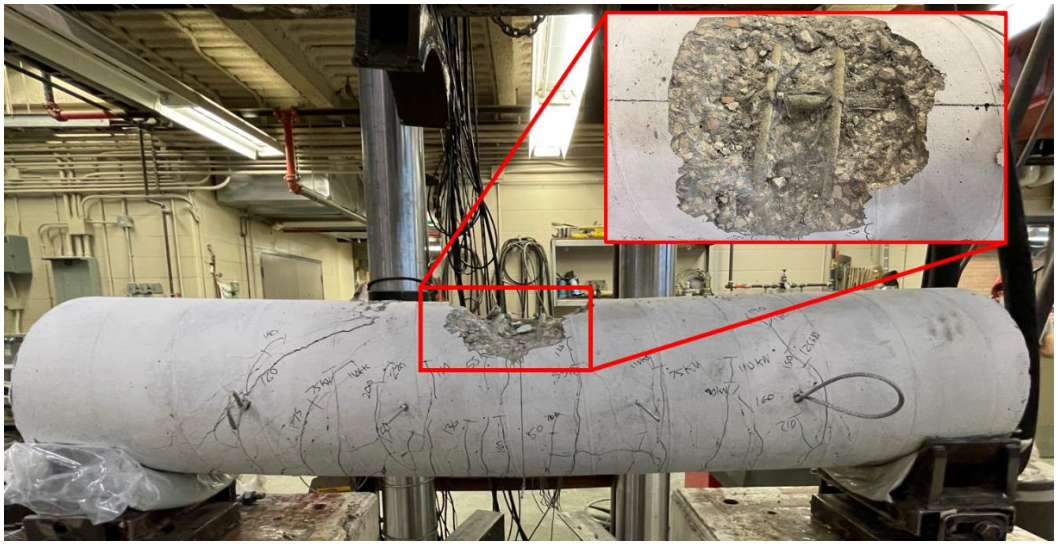

Figure 5.8 – Mode of failure for specimen G85-20-FL

The first crack appeared at 55 kN, which reduced the moment of inertia significantly. As the load increased, the deflection began to increase rapidly with the development of additional crack and widening of existing ones. This behavior continued until crushing of the concrete cover at a load of 323 kN was observed. The maximum concrete compression strain measured was -3,910 με. At the crushing of concrete cover, the spirals began to exhibit large strains providing substantial confinement to the concrete core that reached a maximum of 3,750 με at failure. This allowed the specimen to carry more load, with the maximum concrete strain developed at the edge of the column core.

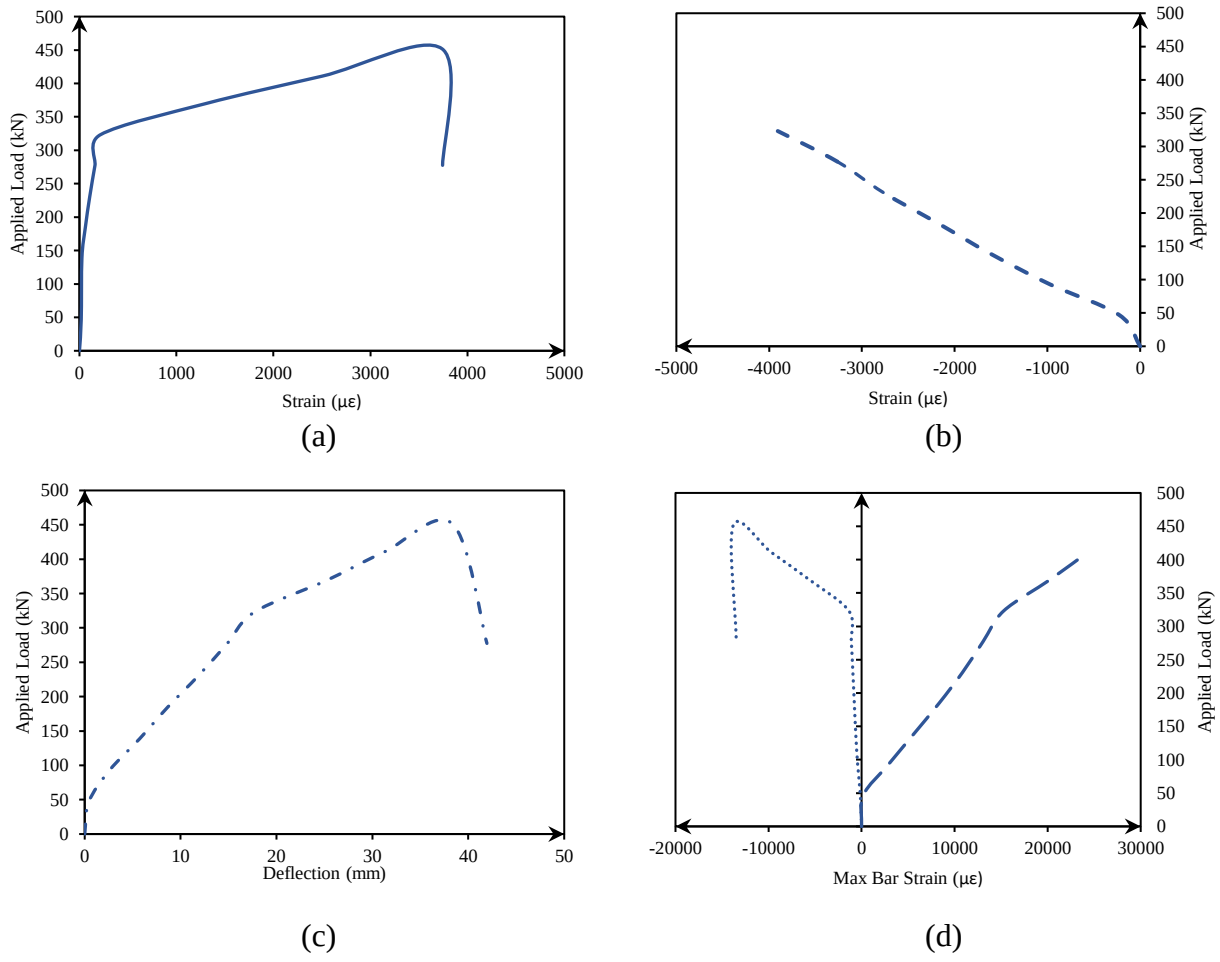

Figure 5.9 – Experimental results for specimen G85-20-FL, (a) Mid-span deflection, (b) Concrete strain, (c) Spiral strain, (d) Reinforcement strain

The compression strains in the reinforcement also started to increase significantly. The outermost tension bars linearly gained strain from the start of the loading, however, after the crushing of concrete cover (323 kN), the rate increased. The compressive and tensile strains in these bars measured prior to the crushing of the concrete cover were -1,360 and 15,270 με, respectively. After the concrete cover crushed, the strains achieved at failure were -13,790 and 24,290 με, respectively. Finally, when the concrete core reached concrete crushing, the specimen failed completely. No rupture or bucking of any of the bars was observed. The maximum load reached was 451 kN corresponding to a moment capacity of 134.0 kN.m.

5.6 Interaction diagram

The specimens tested in this study were used to develop a normalized "knee-shaped" axial load-bending moment interaction diagram (Fig. 5.10). The normalized axial load (K_n) and moment (R_n) , were calculated according to the following equations:

$$K_n = \frac{P_n}{A_g f_c'} \tag{5.1}$$

$$R_n = \frac{M_n}{A_g f_c' D} \tag{5.2}$$

where P_n is the nominal experimental axial load and M_n is the nominal moment, which is the product of the nominal axial load with the eccentricity and maximum lateral displacement (Table 5.3). Moreover, A_g, f'_c, and D are the gross area of the section, the concrete compressive strength, and the diameter of the column cross-section, respectively. Initially, for both specimens with λ = 14 and 20, as the axial capacity increased the moment resistance increased. However, as the *e/D* ratio increased the interaction diagram approached the theoretical balance point, after which, the moment begins to decrease with decreasing axial capacity. The last point represents a specimen

under pure flexure. Similar interaction diagrams were reported in Barua and El-Salakawy (2020), Barua et al. (2021) and Abdelazim (2020). In addition to the experimental interaction diagrams, the prediction of the ACI 440.1R-15 (ACI 2015); CSA S6-19 (CSA 2019a) and CSA S806-12 (2017) are also presented. To determine the stress distribution in HSC, the predictions were calculated using the method of integration over a finite number of strips, developed by Thorenfeldt et al. (1987). The method was then applied to each design code taking into account the differences such as the crushing strain of the concrete to be used (3,000 or 3,500 με) and whether the code allows for consideration of the compressive capacity of the GFRP bars. The stress in each concrete strip f_c is calculated using the following equations:

$$f_c = \frac{f_c^{'} x r}{r - 1 + x^{kr}} \tag{5.3}$$

$$x = \frac{\varepsilon_c}{\varepsilon_o} \tag{5.4}$$

$$\varepsilon_o = \frac{f_c^{'}}{E_c}\left(\frac{r}{r-1}\right) \tag{5.5}$$

$$r = 0.8 + \left(\frac{f_c^{'}}{17}\right) \tag{5.6}$$

$$\text{for } \frac{\varepsilon_c}{\varepsilon_o} \le 1.0 \text{ , } k = 1.0 \quad \text{and for } \frac{\varepsilon_c}{\varepsilon_o} > 1.0 \text{ , } k = 0.67 + \left(\frac{f_c^{'}}{62}\right) \ge 1.0 \tag{5.7}$$

where f'_c is the concrete compressive strength, ε_o is the strain corresponding to f'_c, ε_c is the strain corresponding to any concrete strip stress f_c , r is the curve-fitting factor and k is the slope control. Although the code predictions were similar, there are differences due to small disparities in the provisions. The CSA S6-19 allows for consideration of the compressive capacity of GFRP bars up to a strain of 0.002 and this is apparent when compared to the corresponding interaction diagram

envelopes for both the CSA S806-12 and the ACI 440.1R-15 counterparts. Additionally, while the top portion of the CSA S806-12 and the ACI 440.1R-15 diagrams are almost identical, the lower portion (beyond the balance point) of the CSA S806-12 has slightly larger moment capacities. This is due to the CSA S860-12 allowing for a higher concrete crushing strain, on which the moment capacity is more dependant than the reinforcement. These predictions do not take into account the slenderness effect and are used to predict the capacity of short columns. As can be seen in Fig. 5.10, the short and slender column capacities exceeded the predictions of all code predictions. However, as shown by the experimental diagrams, the specimens with $\lambda = 20$ have a reduced capacity due to the slenderness effect.

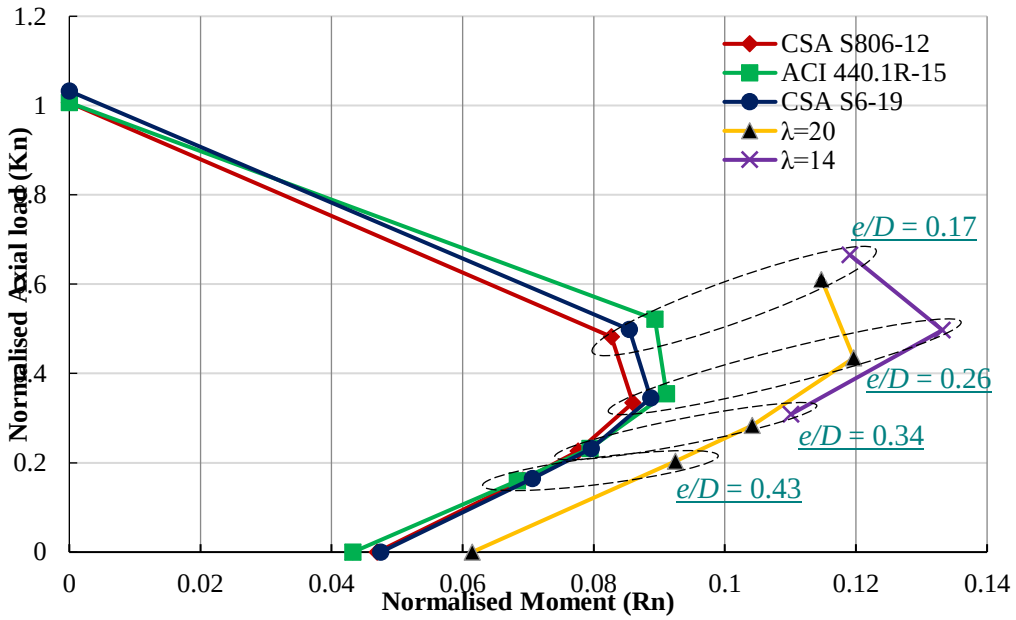

Figure 5.10 – Axial load-bending moment interaction diagram

5.7 Conclusion

In this study, ten large-scale HSC columns were tested until failure. The main conclusions are summarized as follows:

1. GFRP-reinforced HSC columns showed very similar behavior to their steel-RC counterparts in terms of vertical and lateral displacements as well as concrete and reinforcement strains up to the peak load. The GFRP-HSC columns were able to achieve approximately 92% of the axial capacity of their steel-RC counterpart.
2. Reducing the spiral pitch from 85 to 50 mm had very little effect on the axial capacity of the columns. However, the column with 50-mm spiral pitch exhibited improved post-peak behavior, allowing it to impede the capacity degradation.
3. All columns showed material-type failures characterized by crushing of concrete. Furthermore, the short column under the lowest *e/D* ratio (0.17) showed large dilation of the cross-section in the post-peak stage. This, in turn, caused the outermost compression bar to buckle and the spiral to rupture at the same location.
4. Increasing the slenderness ratio from 14 to 20 caused an increase in the lateral displacement of 141.7, 68.4 and 62.9% and in secondary moment by 124.2, 48.1 and 51.1% in addition to a decrease in axial load by 8.3, 12.6 and 8.2% for *e/D* ratios 0.17, 0.26 and 0.34, respectively. This indicates that columns with $\lambda = 20$ behaved in a slender manner.
5. Increasing the eccentricity of the load caused a more significant reduction in the axial capacity of the column than increasing the slenderness ratio. Increasing the eccentricity in increments of 30 mm caused a reduction in axial capacity of 25.3 and 53.7% for the columns with $\lambda = 14$ and 28.8, 53.6 and 66.7% for the counterpart columns with $\lambda = 20$.
6. Increasing the concrete strength from 38 to 60 MPa significantly increased the axial capacity of the column. The increase in the concrete strength caused an increase in the axial and lateral stiffness attributed to the properties of the HSC. Compared to NSC columns at

their peak load, using HSC decreased the compressive bar strains by 51 and 58% and the tensile bar strains by 64 and 54% for specimens with *e/D* ratios 0.17 and 0.34, respectively.

7. The specimen tested in flexure was able to reach a maximum moment capacity of 134.5 kN.m. The strains developed in the compression bars reached -1,360 με as the concrete cover crushed and increased to -13,790 με at failure. Similarly, tension strains reached 15,270 με and further increased to 24,290 με at failure. Additionally, the maximum spiral strain observed at failure was 3,740 με.
8. The test data obtained was used to produce an axial load-bending moment interaction diagram. The moment increased with decreasing axial load up to the balance point and afterwards it decreased with decreasing load. The interaction diagram for the columns with $\lambda = 14$ enveloped that of columns with $\lambda = 20$, showing higher axial and moment capacity. When compared to interaction diagrams predicted by the ACI 440.1R-15, CSA S806-12 and the CSA S6-19, it was found that the code predictions were very conservative.

6. CONCLUSION

6.1 Summary

This study investigated the behaviour of fifteen large-scale HSC columns reinforced with GFRP and steel longitudinal and transverse reinforcement. The specimens were tested under a monotonic eccentric or flexural load. The parameters studied were the reinforcement type, transverse reinforcement pitch, type of loading, slenderness ratio and level of eccentricity. Predictions of the capacity of the columns were calculated using a finite strip integration method in accordance with the relevant American and Canadian codes. Experimental results were then compared against the code predictions.

6.2 Conclusions

The conclusions that can be drawn from this experimental program are as follows:

1) The mode of failure in all specimens can be categorised as material type failures. The columns failed by spalling and crushing of the concrete on the compression side. With lower eccentricities, cracks on the tension side were observed near failure. However, as the eccentricity increased, tension cracks formed at earlier stages due to the increased bending moment and excessive lateral deflections.

2) As the *e/D* ratio increased, the axial load capacity was greatly reduced. The axial capacity of the slender column decreased by 26.6, 54.7 and 68.5% when the *e/D* ratio increased to 0.26, 0.34 and 0.43, respectively, compared to the column with *e/D* = 0.17. Similarly, the capacity of the short column decreased by 29.8 and 53.7% when the *e/D* ratio increased from 0.17 to 0.26 and further to 0.34, respectively.

3) Based on the measured strains, the longitudinal bars have actively contributed to the axial capacity of the column. The strains in the GFRP bar on the compression side reached approximately the same values observed in the concrete. Furthermore, only the short column under e/D = 0.17 showed failure of the GFRP bar and spiral on the compression side.

4) As the slenderness ratio increased from 14 to 28, the axial capacity of the column decreased. For columns loaded at e/D ratio of 0.17, 0.26 and 0.34, the reduction in axial capacity was 20.4, 16.8 and 22.2% respectively. Although the primary moment capacity decreased in the slender columns, however, the secondary moment increased by 172, 118 and 146%.

5) The column under pure flexural loading reached a maximum load of 318 kN, which represents a moment of 150 kN.m. No signs of failure were observed in the GFRP bars or spirals. The GFRP bars were able to develop substantial compressive and tensile strains indicating active contribution to the specimen capacity.

6) The experimental data obtained from the tests were used to develop a normalised axial load-bending moment diagram. The diagram shows that the capacity of both the short and slender columns exceeded the predictions of the Canadian standards (CSA 2017 and 2019a) and the American guidelines (ACI 2015) with the CSA S6-19 (CSA 2019a) giving the closest predictions.

7) GFRP-reinforced HSC columns showed very similar behavior to their steel-RC counterparts in terms of vertical and lateral displacements as well as concrete and reinforcement strains up to the peak load. The GFRP-HSC columns were able to achieve approximately 92% of the axial capacity of their steel-RC counterpart.

8) Reducing the spiral pitch from 85 to 50 mm had very little effect on the axial capacity of the columns. However, the column with 50-mm spiral pitch exhibited improved post-peak behavior, allowing it to impede the capacity degradation.

9) All columns showed material-type failures characterized by crushing of concrete. Furthermore, the short column under the lowest *e/D* ratio (0.17) showed large dilation of the cross-section in the post-peak stage. This, in turn, caused the outermost compression bar to buckle and the spiral to rupture at the same location.

10) Increasing the slenderness ratio from 14 to 20 caused an increase in the lateral displacement of 141.7, 68.4 and 62.9% and in secondary moment by 124.2, 48.1 and 51.1% in addition to a decrease in axial load by 8.3, 12.6 and 8.2% for *e/D* ratios 0.17, 0.26 and 0.34, respectively. This indicates that columns with $\lambda = 20$ behaved in a slender manner.

11) Increasing the eccentricity of the load caused a more significant reduction in the axial capacity of the column than increasing the slenderness ratio. Increasing the eccentricity in increments of 30 mm caused a reduction in axial capacity of 25.3 and 53.7% for the columns with $\lambda = 14$ and 28.8, 53.6 and 66.7% for the counterpart columns with $\lambda = 20$.

12) Increasing the concrete strength from 38 to 60 MPa significantly increased the axial capacity of the column. The increase in the concrete strength caused an increase in the axial and lateral stiffness attributed to the properties of the HSC. Compared to NSC columns at their peak load, using HSC decreased the compressive bar strains by 51 and 58% and the tensile bar strains by 64 and 54% for specimens with *e/D* ratios 0.17 and 0.34, respectively.

13) The specimen tested in flexure was able to reach a maximum moment capacity of 134.5 kN.m. The strains developed in the compression bars reached -1,360 με as the concrete cover crushed and increased to -13,790 με at failure. Similarly, tension strains reached

15,270 με and further increased to 24,290 με at failure. Additionally, the maximum spiral strain observed at failure was 3,740 με.

14) The test data obtained was used to produce an axial load-bending moment interaction diagram. The moment increased with decreasing axial load up to the balance point and afterwards it decreased with decreasing load. The interaction diagram for the columns with $\lambda = 14$ enveloped that of columns with $\lambda = 20$, showing higher axial and moment capacity. When compared to interaction diagrams predicted by the ACI 440.1R-15, CSA S806-12 and the CSA S6-19, it was found that the code predictions were very conservative.

6.3 Future Work

The following are suggestions for future work on HSC columns reinforced with GFRP bars and spirals:

1. Investigate the behaviour of HSC rectangular columns under axial, eccentric and flexural loading conditions.
2. Study the effect of using fibre-reinforced concrete (FRC) on the behaviour of GFRP-RC columns.
3. Conduct a numerical finite element analysis to further investigate a wider range of the parameters used in this study.
4. Use data from this study and other literature to produce a confinement model for HSC columns reinforced with GFRP bars and spirals.
5. Investigate the behaviour of BFRP (Basalt) and AFRP (Aramid) reinforced HSC columns.

References

Abdallah, A. E. M., and Ehab El-Salakawy (2021) “Confinement Properties of GFRP-Reinforced Concrete Circular Columns under Simulated Seismic Loading”, ASCE *Journal of Composites for Construction* 25(2): 04020088.

Abdelazim, W. (2020). “Behavior of Slender Concrete Columns Reinforced with GFRP-Bars And Spirals Under Concentric and Eccentric Loads”. PhD Thesis, Dept. of Civil Engineering, University of Sherbrooke, Sherbrooke, QC, Canada.

ACI Committee 222. (2019). "Guide to Protection of Metals in Concrete Against Corrosion" ACI 222R-19. American Concrete Institute (ACI): Farmington Hills, Detroit, MI..

ACI Committee 318 (2019). “Building code requirements for structural concrete (ACI 318-19) and commentary (ACI 318R-19).” American Concrete Institute, Farmington Hills Detroit, MI.

ACI Committee 363. (2010). "Report on High-Strength Concrete". ACI 363R-10, American Concrete Institute (ACI), Farmington Hills, Detroit, MI.

ACI Committee 440.1R. (2015). "Guide for the Design and Construction of Structural Concrete Reinforced with Fiber-Reinforced Polymer (FRP) Bars" ACI 440.1R-15. American Concrete Institute (ACI): Farmington Hills, Detroit, MI.

Afifi, M.Z. (2013). "Behaviour of Circular Concrete Columns Reinforced with FRP Bars and Stirrups". PhD Thesis, Department of Civil Engineering, University of Sherbrooke: Sherbrooke, QC, Canada.

Afifi, M.Z., Mohamed, H.M. and Benmokrane, B. (2013). "Axial Capacity of Circular Concrete Columns Reinforced with GFRP Bars and Spirals". Journal of Composites for Construction, ASCE, V. 18, No 1: 04013017.

Ahmad, S.H. and Shah, S.P. (1982). "Stress-Strain Curves of Concrete Confined By Spiral Reinforcement". ACI Structural Journal, 79(6): p.484–490.

Ali, M. (2015). "Seismic Performance of Rectangular GFRP-Reinforced Concrete Columns". M.Sc. Thesis, Department of Civil Engineering, University of Manitoba: Winnipeg, MB, Canada.

Ali, M.A. and El-Salakawy, E. (2016). "Seismic Performance of GFRP-Reinforced Concrete Rectangular Columns". ASCE Journal of Composites for Construction 20(3): 04015074: DOI: 10.1061/(ASCE)CC.1943-5614.0000637.

Barua, S., and El-Salakawy, E. (2020). "Performance of GFRP-Reinforced Concrete Circular Short Columns under Concentric, Eccentric, and Flexural Loads". Journal of Composites for Construction, ASCE, V. 24, No. 5: 04020044.

Barua, S., Mahmoud, K. and El-Salakawy, E. (2021). " Slender GFRP-RC Circular Columns under Concentric, Eccentric, and Flexural Loads: Experimental Investigation". Journal of Bridge Engineering, ASCE, V. 26, No. 7: 04021033.

Broms, B. and Viest, I. M. (1961). “Long Reinforced Concrete Columns: A Symposium,” *Transactions, ASCE,* V. 126, No. 2, pp. 308-400.

CSA. (2019a). "Canadian Highway Bridge Design Code" CSA/ S6-19. Canadian Standard Association (CSA): Toronto, Ontario, Canada.

CSA. (2019b). “Carbon steel bars for concrete reinforcement.” G30.18-09 (R2019), Canadian Standard Association (CSA). Toronto, ON, Canada.

CSA. (2019c). "Concrete materials and methods of concrete construction/Test moethods and standard practices for concrete" CSA A23.1/2-19. Canadian Standard Association (CSA): Toronto, Ontario, Canada.

CSA. (2019d). "Design of Concrete Structures" CSA A23.3-19. Canadian Standard Association (CSA): Toronto, Ontario, Canada.

CSA. (2019e). “Specification for fibre-reinforced polymers.” CSA S807-19. Canadian Standard Association (CSA). Toronto, Ontario, Canada.

CSA. (2017). "Design and construction of building structures with fibre-reinforced polymers" CSA S806-12. Canadian Standard Association (CSA): Toronto, Ontario, Canada.

De Luca, A., Matta, F., and Nanni, A. (2010). "Behavior of full-scale glass fiber-reinforced polymer reinforced concrete columns under axial load". *ACI Structural Journal,* V. 107, No.5: p.589–596.

El-Gendy, M.G., and El-Salakawy, E. (2016). “Effect of shear studs and high moments on punching behavior of GFRP-RC slab–column edge connections”. *Journal of Composites for Construction*, ASCE, V.20, No.4:04016007.

El-Salakawy, E., Benmokrane, B. & Desgagné, G. (2003). "Discussion of ‘Fibre-reinforced polymer composite bars for the concrete deck slab of Wotton Bridge’". Canadian Journal of Civil Engineering, 31(3): 530–531.

Elchalakani, M., Dong, M., Karrech, A., Sadakkathulla, M., and Ali, M. (2020). "Circular Concrete Columns and Beams Reinforced with GFRP Bars and Spirals under Axial, Eccentric, and Flexural Loading". *Journal of Composites for Construction*, ASCE, V. 24, No. 3: 04020008.

Elshamandy, M.G., Farghaly, A.S. & Benmokrane, B. (2018). "Experimental behavior of glass fiber-reinforced polymer-reinforced concrete columns under lateral cyclic load". ACI Structural Journal, 115(2): 337–349.

Ghomi, S.K. and El-Salakawy, E. (2016). “Seismic performance of GFRP-RC exterior beam–column joints with lateral beams”. *Journal of Composites for Construction*, ASCE, V.20, No.1: 04015019.

Guérin, M., Mohamed, H.M., Benmokrane, B., Nanni, A. & Shield, C.K. (2018). "Eccentric behavior of full-scale reinforced concrete columns with glass fiber-reinforced polymer bars and ties". ACI Structural Journal, 115(2): 489–499.

Hadhood, A. (2017). "Behaviour, Strength and Flexural Stiffness of Circular Concrete Columns Reinforced with FRP Bars and Spirals/Hoops under Eccentric Loading". PhD Thesis, Department of Civil Engineering, University of Sherbrooke: Sherbrooke, QC, Canada.

Hadhood, A., Mohamed, H.M. & Benmokrane, B. (2016). "Behavior of circular frp-reinforced concrete columns under eccentric loading". CSCE Annual Conference: Resilient Infrastructure, London, ON, Canada, STR-828-(1-8).

Hadhood, Abdeldayem, Mohamed, H.M. & Benmokrane, B. (2016). "Experimental Study of Circular High-Strength Concrete Columns Reinforced with GFRP Bars and Spirals under Concentric and Eccentric Loading". ASCE Journal of Composites for Construction, 21(2): p.04016078.

Hadi, M.N.S., Hasan, H.A., and Sheikh, M.N. (2017). "Experimental Investigation of Circular High-Strength Concrete Columns Reinforced with Glass Fiber-Reinforced Polymer Bars and Helices under Different Loading Conditions". *Journal of Composites for Construction*, ACSE, V.21, No. 4: 04017005.

Hales, T.A., Pantelides, C.P., and Reaveley, L.D. (2016). "Experimental Evaluation of Slender High-Strength Concrete Columns with GFRP and Hybrid Reinforcement". *Journal of Composites for Construction*, ASCE, V.20, No.6: 04016050.

ISIS Canada. (2007). "Reinforcing Concrete Structures with Fibre Reinforced Polymers." Design Manual No.3. ISIS Canada corporation: University of Manitoba, Winnipeg, Canada, 103 p.

Karim, H., Neaz S. M., Hadi, M. N. S. (2016) “Load and Moment Interaction Diagram for Circular Concrete Columns Reinforced with GFRP Bars and GFRP Helices”. ASCE, *Journal of Composites for Construction*, 21(1): 04016076.

Khorramian, K. and Sadeghian, P. (2017). "Experimental and analytical behavior of short concrete columns reinforced with GFRP bars under eccentric loading". *Engineering Structures* 151: p.761–773.

Khorramian, K., and Sadeghian, P. (2020). "Experimental Investigation of Short and Slender Rectangular Concrete Columns Reinforced with GFRP Bars under Eccentric Axial Loads". *Journal of Composites for Construction*, ASCE, V.24, No.6: 04020072.

Mahmoud, K., and El-Salakawy, E. (2016). “Size Effect on Shear Strength of Glass Fiber-Reinforced Polymer- Reinforced Concrete Continuous Beams”. *ACI Structural Journal, V. 113, No.1: p.125-134.*

Martinez, S., Nilson, A.H. & Slate, F.O. (1984). "Spirally Reinforced High-Strength Concrete Columns". ACI Structural Journal , 81(5): 431–442.

Mirmiran, A., Yuan, W., and Chen, X. (2001). "Design for Slenderness in Concrete Columns Internally Reinforced with Fiber-Reinforced Polymer Bars ". *ACI Structural Journal*, V. 98, No.1: p.116-125.

Naqvi, S. & El-Salakawy, E. (2016). "Lap Splice in GFRP-RC Rectangular Columns Subjected to Cyclic-Reversed Loads". ASCE Journal of Composites for Construction, 21(4): 04016117.

Park, R. & Paulay, T. (1975). "Reinforced Concrete Structures". John Wiley & Sons, Inc.: Hoboken, NJ, USA. http://doi.wiley.com/10.1002/9780470172834.

Rahman, S.M.H., Mahmoud, K., and El-Salakawy, E. (2017). “Behavior of glass fiber–reinforced polymer reinforced concrete continuous T-beams”. *Journal of Composites for Construction*, ASCE, V.21, No.2: 04016085.

Schmidt, M. & Fehling, E. (2004). "Ultra High Performance Concrete (UHPC)". Proceedings of the 1st International Symposium on Ultra High Performance Concrete, Schriftenreihe Baustoffe und Massivbau, Universitat Kassel, Kassel, Germany.

Tavassoli, A. (2013). "Behaviour of GFRP-Reinforced Concrete Columns under Combined Axial Load and Flexure". M.Sc. Thesis, Department of Civil Engineering, University of Toronto, Toronto, ON, Canada.

Thorenfeldt, E., Tomaszewicz, A. and Jensen, J. J. (1987). “Mechanical properties of high strength concrete and Application to design,” *Proceedings of the Symposium: Utilization of High-Strength Concrete,* Stavanger, Norway, 149-159.

Xue, W., Peng, F. & Fang, Z. (2018). "Behavior and design of slender rectangular concrete columns longitudinally reinforced with fiber-reinforced polymer bars". ACI Structural Journal, 115(2): 311–322.

Yong, Y.-K., Nour, M.G. & Nawy, E.G. (1988). "Behavior of Laterally Confined High-Strength Concrete under Axial Loads". ASCE Journal of Structural Engineering, 114(2): 332–351

APPENDIX A – GFRP-RC COLUMN DESIGN

Column dimensions:

L = 1250, 1750, 2450 mm

D = 355 mm

A = 98,980 mm^2

FRP longitudinal reinforcement:

$\rho_{l,min} = 0.01$

$\therefore A_{frp,req} = 0.01 \times 96{,}211 = 962.11\ mm^2$

Use No. 15 bars ($A_b = 199\ mm^2$)

$\therefore n = \frac{962.11}{199} \approx 5\ bars$

However, minimum number of bars for a circular column is 6 bars.

$\therefore \rho_{frp} = \frac{199 \times 6}{98{,}980} = 1.21\%$

FRP transverse reinforcement:

CSA S806, Clause 8.4.3.13: FRP spirals for compression members shall conform to the following:

a) spiral reinforcement shall have a minimum diameter of 6 mm

   [Satisfied by **9.5 mm spirals**]

b) the pitch or distance between turns of the spirals shall not exceed 1/6 of the core diameter

   [=(355-25-25-9.5)×1/6 = 49.25 ≈**50 mm pitch**]

c) the clear spacing between successive turns of a spiral shall not exceed 75 mm nor be less than 25 mm

   [75 mm clear + 9.5 ≈ **85 mm pitch**]

d) the volumetric ratio of spiral reinforcement shall be not less than the value given by

$$\rho_{FS} = \frac{f'_c}{f_{Fh}}\left(\frac{A_g}{A_c} - 1\right)\left(\frac{P}{P_0}\right) = \frac{60}{0.006*58000}\left(\frac{98{,}980}{70{,}920} - 1\right)(0.2) = 1.36\%$$

For 50 mm pitch $\rho_{FS} = 1.89\%$

For 85 mm pitch $\rho_{FS} = 1.11\%$

According to these provisions, 50 mm pitch must be used, however, 50 and 85 mm were used to investigate the level of conservativeness of the code requirements.

Axial capacity:

f_{frp} is equal to $0.002E_{frp}$ according to the CSA S6-19 and is neglected in the other codes.

As per the CSA S6-19, $P_o = 0.85f'_c\left(A_g - A_{frp}\right) + f_{frp}A_{frp}$

$= 0.85(60)(98{,}980 - 1{,}194) + 0.002(64{,}000)(1{,}194) = 5{,}140\ kN$

APPENDIX B – STEEL-RC COLUMN DESIGN

Steel longitudinal reinforcement:

$\rho_{l,min} = 0.01$

$\therefore A_{s,req} = 0.01 \times 96{,}211 = 962.11\ mm^2$

Use 15M bars ($A_b = 200\ mm^2$)

$\therefore n = \frac{962.11}{200} \approx 5\ bars$

However, minimum number of bars for a circular column is 6 bars.

$\therefore \rho_{frp} = \frac{200 \times 6}{98{,}980} = 1.21\%$

Steel transverse reinforcement:

$$\rho_s = 0.5\left(\frac{A_g}{A_c} - 1\right)^{1.4} \frac{f'_c}{f_y} = 0.5\left(\frac{98{,}980}{70{,}920} - 1\right)\frac{60}{420} = 1.98\%$$

$$s_{req} = \frac{4A_{sp}}{D_c \rho_{s,req}} = \frac{4 \times 100}{300 \times 0.0198} = 67\ mm$$

85 mm was used to make the steel specimen reinforcement comparable to its GFRP counterpart.

Axial capacity:

$P_o = 0.85 f'_c\left(A_g - A_{st}\right) + f_y A_{st} = 0.85(60)(98{,}980 - 1200) + 460(1200) = 5{,}538\ kN$

APPENDIX C – LOAD PREDICTIONS

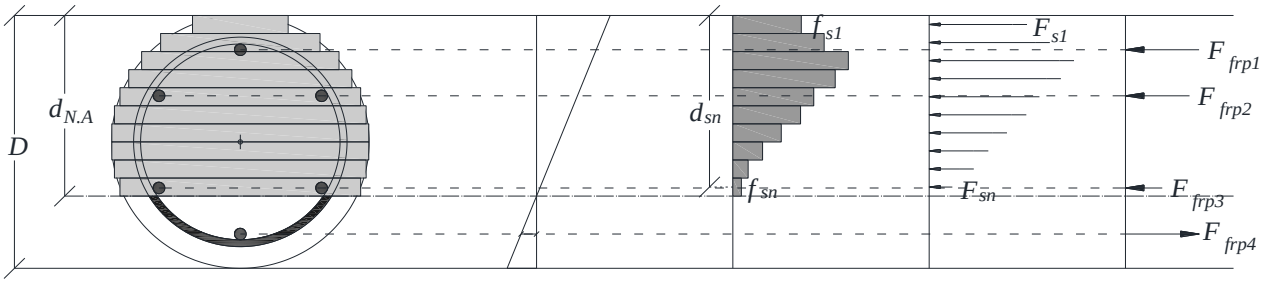

Equations 4.1 – 4.5 were programmed in an excel sheet to find the stress and force in each concrete strip of 1 mm thickness.

Axial load = $\sum_1^n F_{sn} + \left(F_{frp1} + F_{frp2} + F_{frp3} + F_{frp4}\right)$

Moment = $\sum_1^n (F_{sn})(\frac{D}{2} - d_{sn}) + \Big(F_{frp1}(\frac{D}{2} - d_{frp1}) + F_{frp2}(\frac{D}{2} - d_{frp2}) + F_{frp3}(\frac{D}{2} - d_{frp3}) + F_{frp4}(d_{frp4})\Big)$

The compressive forces (F_{frpn}) in the bars were neglected or included to reflect the provisions of the respective design code. The results from this analysis were used to generate an interaction diagram.